



HAL
open science

3D whole-brain quantitative histopathology : methodology and applications in mouse models of Alzheimer's disease

Michel Vandenberghe

► **To cite this version:**

Michel Vandenberghe. 3D whole-brain quantitative histopathology : methodology and applications in mouse models of Alzheimer's disease. Medical Imaging. Université Pierre et Marie Curie - Paris VI, 2015. English. NNT : 2015PA066411 . tel-01381094

HAL Id: tel-01381094

<https://theses.hal.science/tel-01381094>

Submitted on 14 Oct 2016

HAL is a multi-disciplinary open access archive for the deposit and dissemination of scientific research documents, whether they are published or not. The documents may come from teaching and research institutions in France or abroad, or from public or private research centers.

L'archive ouverte pluridisciplinaire **HAL**, est destinée au dépôt et à la diffusion de documents scientifiques de niveau recherche, publiés ou non, émanant des établissements d'enseignement et de recherche français ou étrangers, des laboratoires publics ou privés.



**THÈSE DE DOCTORAT DE
L'UNIVERSITÉ PIERRE ET MARIE CURIE**

École doctorale Informatique, Télécommunications et Électronique
(Paris)

Présentée par

Michel VANDENBERGHE

Pour obtenir le grade de
**DOCTEUR de l'UNIVERSITÉ PIERRE ET MARIE
CURIE**

Sujet de la thèse :

**3D whole-brain quantitative histopathology:
methodology and applications in mouse models of
Alzheimer's disease**

soutenue le 12 octobre 2015

devant le jury composé de :

M. Daniel RACOCEANU	Président du jury
M. Thierry DELZESCAUX	Directeur de thèse
Mme Frédérique FROUIN	Directeur de thèse
Mme Anne-Sophie HÉRARD	Encadrant de thèse
M. Grégoire MALANDAIN	Rapporteur
M. Stephen SAWIAK	Rapporteur
M. Régis GRAILHE	Examineur

Remerciements

List of abbreviations

APP Amyloid Precursor Protein

CCD Coupled-charge device

DAB Diaminobenzidine

EM Expectation-Minimization

FDR False Discovery Rate

FFD Free-Form Deformation

FOV Field-of-view

GMM Gaussian Mixture Models

IHC Immunohistochemistry

MRI Magnetic resonance imaging

PET Positron emission tomography

PS1 Presenilin 1

RF Random Forest

ROI Region of interest

SPM Statistical Parametric Mapping

WRF Weighted Random Forest

Abstract

Histology is the gold standard to study the spatial distribution of the molecular building blocks of organs and to inspect the architecture of cells within tissues. In humans and in animal models of disease, histology is widely used to highlight neuropathological markers on brain tissue sections. This makes it particularly useful to investigate the pathophysiology of neurodegenerative diseases such as Alzheimer's disease and to evaluate drug candidates. However, due to tedious manual interventions, quantification of histopathological markers is classically performed on a few tissue sections, thus restricting measurements to limited portions of the brain. Quantitative methods are lacking for whole-brain analysis of cellular and pathological markers. In this work, we propose an automated and scalable method to thoroughly quantify and analyze histopathological markers in 3D in rodent whole brains. Histology images are reconstructed in 3D using block-face photography as a spatial reference and the markers of interest are segmented via supervised machine learning. Two complimentary approaches are proposed to detect differences in histopathological marker load between groups of animals: an ontology-based approach is used to infer difference at the level of brain regions and a voxel-wise approach is used to detect local differences without spatial *a priori*. Several applications in mouse models of $A\beta$ deposition are described to illustrate 3D histopathology usability to characterize animal models of brain diseases, to evaluate the effect of experimental interventions, to anatomically correlate cellular and pathological markers throughout the entire brain and to validate *in vivo* imaging techniques.

Résumé

L'histologie est la méthode de choix pour l'étude *ex vivo* de la distribution spatiale des molécules qui composent les organes et pour l'étude de l'architecture cellulaire des tissus. En particulier, l'histologie permet de mettre en évidence les marqueurs neuropathologiques de la maladie d'Alzheimer chez les humains et les modèles animaux de la maladie ce qui en fait un outil incontournable pour étudier la physiopathologie de la maladie et pour évaluer l'efficacité de candidats médicaments. Classiquement, l'analyse de données histologiques implique de lourdes interventions manuelles, et de ce fait, est souvent limitée à l'analyse d'un nombre restreint de coupes histologiques et à quelques régions d'intérêts. Dans ce travail de thèse, nous proposons une méthode automatique pour l'analyse quantitative de marqueurs histopathologiques en trois dimensions dans le cerveau entier de rongeurs. Les images histologiques deux-dimensionnelles sont d'abord reconstruites en trois dimensions en utilisant l'imagerie photographique de bloc comme référence géométrique et les marqueurs d'intérêts sont segmentés par apprentissage automatique. Deux approches sont proposées pour détecter des différences entre groupes d'animaux: la première est basée sur l'utilisation d'une ontologie anatomique de cerveau qui permet détecter des différences à l'échelle de structures entières et la deuxième approche est basée sur la comparaison voxel-à-voxel afin de détecter des différences locales sans *a priori* spatial. Cette méthode a été appliquée dans plusieurs études chez des souris modèles de dépôt amyloïde afin d'en démontrer l'utilisabilité pour caractériser des modèles animaux pathologiques, évaluer des candidats médicaments, corréler les distributions spatiales de plusieurs marqueurs à travers le cerveau et pour valider des modalités d'imagerie *in vivo*.

Contents

Introduction	1
1 Context	5
1.1 Histology	5
1.1.1 Principles and evolution	5
1.1.2 Histology imaging	11
1.1.3 Histopathological biomarkers quantification	15
1.2 Alzheimer’s disease	20
1.2.1 Impact on public health	20
1.2.2 Pathological hypotheses	21
1.2.3 Preclinical research on Alzheimer’s disease	25
1.3 Motivation	26
2 High-throughput 3D histopathology	29
2.1 Large-scale tissue section processing	29
2.2 Whole-slide imaging strategies	32
2.3 Brain multi-modal 3D reconstruction	35
2.4 Supervised segmentation of neuropathological markers	38
3 Brain-wide quantitative analysis of neuropathological markers	51
3.1 Ontology-based analysis	51
3.1.1 3D mouse brain atlases	51
3.1.2 Atlas registration to histopathological data	53
3.1.3 Mouse brain ontology	54
3.2 Voxel-wise analysis	56
3.2.1 Principle and issues for histopathological data analysis	56
3.2.2 Heat map generation	62
3.2.3 Cluster detection with simulated data	65

CONTENTS

4 Applications in mouse models of Aβ deposition	73
4.1 Context of the studies	73
4.2 Study 1: animal model characterization	75
4.2.1 Experimental procedures	75
4.2.2 Ontology-based characterization of A β deposition	76
4.3 Study 2: preclinical immunotherapy evaluation	76
4.3.1 Experimental procedures	76
4.3.2 Whole-brain therapeutic intervention evaluation	78
4.3.3 3D versus 2D histopathology comparison	81
4.4 Study 3: gene effect evaluation	83
4.4.1 Experimental procedures	83
4.4.2 Image processing	85
4.4.3 ADAM30 effect on A β pathology	90
4.4.4 Discussion	94
5 Towards multimodal and multiscale analysis	97
5.1 Matching quantitative 3D histopathology to <i>in vivo</i> MRI	99
5.2 3D whole-brain histopathology at the cellular-scale	103
5.2.1 Spatial correlation between cellular markers at the whole- brain level	103
5.2.2 A hierarchical Gaussian Mixture Model (GMM) approach for touching cells segmentation	107
Conclusion	117
A 3D Histopathology Analysis Pipeline (3D-HAPi)	123
B Experimental procedures summary	127
C Publications	129

Introduction

Fueled by advances in technology and computer engineering, biomedical research has profoundly evolved over the last decades. The essential feature of this change has been the introduction of techniques generating massive amounts of data. Examples of this revolution abound. A successful example is the advent of genomic technologies. Since the human genome has been first sequenced in 2003, genomics have considerably evolved so that it is now possible to decode the entire sequence of the 3 billion elements that constitute our genome in only a few days. This led to discovery of genes involved in diseases such as cancer, autism and Alzheimer's disease and paved the way for earlier diagnosis and more personalized medical care. In the drug discovery area, the impact of large-scale technologies has been huge with the establishment of high-throughput screening as a leading technique to discover new active compounds. Other examples come from brain imaging with, for instance, functional magnetic resonance imaging which has enabled to map brain activation dynamics with high spatial and temporal resolutions.

The introduction of high-throughput digital technologies in biology has an essential consequence on how scientific hypotheses are formulated and investigated. Rather than testing one hypothesis at a time, researchers can now explore thousands to millions of hypotheses in single experiments. In functional brain imaging for example, voxel-wise statistical analysis allows to investigate the relationship between behavior and the activation of thousands of locations in the brain. An even more tantalizing aspect of high-throughput technologies is to find new hypotheses from data itself. In high-throughput screening for example, hundreds of thousands of compounds are tested in replicated experiments without *a priori* hypothesis on their pharmacological properties. Most promising compounds are then evaluated in secondary assays to confirm initial hypotheses. More data, however, does not necessarily translate into more knowledge. Indeed, as more data is generated, it becomes harder to control the quality of individual instances over whole datasets. Also, testing many hypotheses at a time raises statistical issues relating to multi-

ple comparisons. Therefore, drawing reproducible results from massive datasets is particularly challenging.

A more recent yet similar evolution towards **high-throughput technologies** is happening in the area of **histopathology**. Histopathology relies on tissue sectioning and subsequent staining with dyes that reveal the presence of the elementary constituents of organs (proteins, carbohydrates, lipids). To date, microscopic imaging of histopathology tissue section is the gold standard technique to study the spatial distribution of specific markers within the brain. While histopathology has been in use since the 19th century, recent developments in digital imaging are considerably extending its capabilities. The rising use of automated slide staining systems and the development of whole slide imaging technologies have dramatically increased the throughput of histopathological material production and image digitization.

While more and more brain histopathology data becomes available to the researcher, **quantitative analysis remains a bottleneck**. Adapted tools are lacking to mine brain histopathological data and to extract valuable biological information. Indeed, current standards for the analysis of neuropathological markers heavily rely on manual intervention. Hence, data analysis is usually restricted to a few tissue sections and a few regions of interest. While this can be sufficient for many studies, it drastically limits the scope of the analysis in studies with low prior knowledge about biomarkers of interest, if any and it increases the risk of sampling error.

Preclinical research is fundamental to the understanding of disease and to the development of new therapeutics. Due to evident ethical reasons, any drug candidate has to be thoroughly evaluated in animal models of disease before it enters clinical trials. A number of rodent models show neuropathological markers similar to human neurodegenerative diseases. Imaging and quantifying pathophysiological markers in these models is essential to evaluate the effect of new therapies. Because histopathological investigations take an important role in drug discovery, exhaustive histopathology data analysis could imply better understanding of drug mechanism of action and toxicity early on during drug development. Also it can be expected that system-level analysis of neuropathological markers could benefit to the understanding of complex diseases such as those affecting the brain.

The objective of this work was to develop an integrated approach to quantify and analyze neuropathological markers at the level of the whole brain in rodents. Three features were aimed for at each step of this approach: **exhaustiveness, automation** and **robustness**. The method described in the next chapters relies on **serial histology, block-face photography**, image processing

and analysis. All the computational developments required for this work were performed in the **BrainVISA** open-source environment. A new image processing pipeline, 3D Histology Analysis Pipeline (**3D-HAPi**), integrates most of the computational aspects described in this thesis and will be made publicly available soon (brainvisa.info).

This work took place in **MIRCen** (Molecular Imaging Research Center) in the neurodegenerative diseases laboratory **CNRS/CEA UMR9199**. Owing to unique facilities in MIRCen, internal collaborations in UMR9199 and external collaborations with Sanofi, IPSEN and Institut Pasteur de Lille, this approach was applied in several cohort studies involving mouse models of Alzheimer’s disease. **The goals of these studies were to better characterize neuropathological markers distribution in mouse models of cerebral amyloid deposition and to evaluate the effect-size and -localization of experimental interventions (drug treatment, gene over-expression).**

The thesis document has been subdivided into five main parts.

Chapter 1 reviews important aspects of histopathology. Main histopathology techniques are described and briefly put into historical perspective. Methods for image digitization and quantification are reviewed with a focus on current methods for the assessment of neuropathological markers in mouse models of Alzheimer’s disease. This chapter also covers general aspects of Alzheimer’s disease. Current main hypotheses on Alzheimer’s disease pathophysiology are discussed. Animal models of Alzheimer’s disease are described and their relevance to the human disease is analyzed.

Chapter 2 focuses on **high-throughput production of 3D histopathological data**. It consists in several steps: (1) production of series of histopathological tissue sections encompassing the whole-brain; (2) imaging large number of sections with time constraints; (3) recovery of the 3D shape of the brain from 2D tissue section images; (4) segmentation of neuropathological markers in whole-brain histopathology volumes in a robust and scalable fashion. Describing this last step will be the opportunity to present **a new method for neuropathology image segmentation** and to compare it with the current state-of-the art.

Chapter 3 presents two approaches to extract meaningful biological information from whole-brain histopathology volumes. Both approaches are commonly used in clinical brain imaging and to some extent in preclinical imaging and extended here for the analysis of histopathological data. The **ontology-based analysis** enables to perform global measures of neuropathological marker loads in hierarchically-

CONTENTS

organized regions of interest while **voxel-wise analysis** can be used to detect local differences between groups of animals without anatomical *a priori*. Due to the nature of histology staining and imaging, voxel-wise analysis cannot be directly applied to histopathological marker analysis. **A solution to extend voxel-wise analysis to histopathological data analysis will be proposed and validated through simulation experiments.**

Chapter 4 shows various applications of the methodology. Three studies will be described:

- The **first study** aims to thoroughly characterize a mouse model of Alzheimer's disease.
- The **second study** evaluates the preclinical efficacy of a new immunotherapy for Alzheimer's disease.
- The **third study** dissects the effect of a newly described protective gene in a mouse model of Alzheimer's disease.

Finally, **chapter 5** opens the door on several extensions for 3D histopathology. An application for whole-brain histopathological data to **validate *in vivo* imaging modalities** is presented. In addition, preliminary results are shown for **whole-brain analysis of cellular markers** and spatial correlation of pathological and cellular markers throughout the brain. Remaining challenges for cellular markers analysis are discussed and a **new method will be proposed to address the problem of individual cells segmentation.**

Chapter 1

Context

1.1 Histology

1.1.1 Principles and evolution

Histology is the study of the microscopic structure of biological tissues and the ensemble of techniques that enable this study. It is broadly used to study the spatial distribution of the molecular building blocks of human and animal organs (proteins, nucleic acids, carbohydrates, lipids) and to inspect the architecture of both cells within tissues and organelles within cells. Not only histological techniques profoundly impacted the current understanding of life but it also deeply changed medical practices. While histological techniques have continuously evolved and became more diverse, a few general principles for tissue histological processing can be drawn:

1. **Tissue collection:** a tissue sample is collected from a donor either *in vivo* via a biopsy or a surgical intervention or *post mortem* via dissection,
2. **Tissue processing:** the sample tissue is prepared in order to preserve its microstructural integrity and is then cut into sections,
3. **Staining:** tissue sections are stained to provide a contrast between structures or molecules of interest and the remaining tissue; tissue sections are then mounted on glass slides,
4. **Imaging:** slides are digitized with high spatial resolution (typically with a microscope).

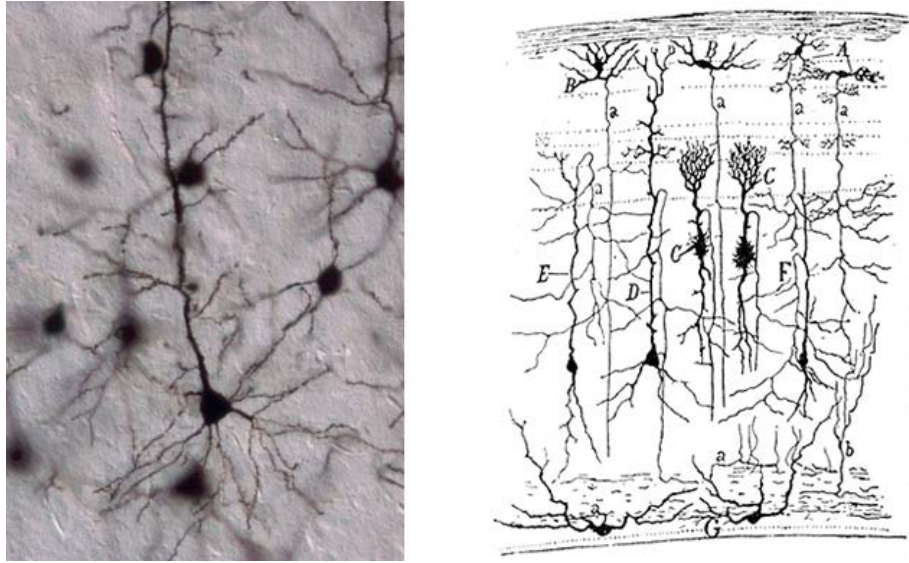


Figure 1.1: Early brain histology. Left: A cortical pyramidal neuron stained with Golgi's method. Right: Different neuronal types in the cerebral cortex as drawn by Ramon y Cajal.

These principles can be traced back to the 19th century when the first histochemical dyes were discovered. With respect to neuroscience, the first successful attempt to stain nerve cells with a chemical dye is due to Camillo Golgi. It consists in impregnating brain tissue with silver nitrate which stains nerve cell bodies and their processes in black (Figure 1.1). This staining allowed to study for the first time the cellular organization of the brain and led Santiago Ramon y Cajal to postulate that neurons were communicating through signals that would be transmitted via axons and synapses. Using another silver staining, Alois Alzheimer discovered the two neuropathological signatures of Alzheimer's disease: **A β plaques** and **neurofibrillary tangles**. Another chemical staining is the Nissl staining, which can be achieved using dyes such as Cresyl violet or toluidine blue. It specifically highlights Nissl bodies which are small intra-cellular granules predominantly found in neurons and it is easy to perform. Therefore, Nissl staining became very popular to reveal structures of the brain. Nowadays, chemical dyes are still commonly used to visualize cells and their environment.

Around the middle of the 20th century, **immunohistochemistry** (IHC) was proposed by Coons *et al.* [1]. Contrary to histochemical staining which relies on fortuitous physicochemical affinities between the dye and biological structures, immunohistochemistry is designed to specifically target molecules of interest. It benefits from the basic property of antibodies to bind specific antigens. In IHC, molecules

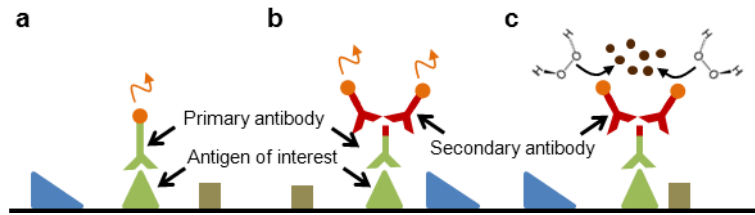


Figure 1.2: Immunohistochemistry principle. (a) Direct immunofluorescence. A single antibody is used to recognize the antigen and emits light when the fluorescent dye is excited. (b-c) Indirect immunohistochemistry. A secondary antibody recognizes the first antibody and is either coupled with a fluorescent dye (b) or is coupled with horseradish peroxidase which can react with DAB and hydrogen peroxide to form a characteristic brown deposit.

of interest are highlighted on tissue sections by incubating them with a specific antibody. If the antibodies are attached with a fluorescent dye, the staining will be observable under fluorescence microscopy. More often, IHC requires two different antibodies. The first one recognizes the antigen (primary antibody) and the second one recognizes the first antibody, thus acting as a signal amplifier (secondary antibody, Figure 1.2). The secondary antibody is often either bound to a fluorescent dye or to horseradish peroxidase. This latter produces a brown colored product in the presence of hydrogen peroxide and diaminobenzidine (DAB) which highlights the molecule of interest. IHC with a DAB revelation is observed under white light illumination with bright-field microscopy. IHC is a particularly popular technique because antibodies can be engineered to specifically recognize a vast amount of molecules. To give an illustration of this, *Sigma-Aldrich*, a leader in biological products distribution, lists 32884 primary antibodies for IHC on its website as of April 2015. IHC is very powerful to study the brain. Because each cell type expresses specific proteins, one can use IHC to differentiate cell types. Also, IHC can highlight pathological signatures of diseases such as $A\beta$ plaques and neurofibrillary tangles in Alzheimer's disease (Figure 1.3a).

Many other notable histological techniques exist. To name a few, *in situ* hybridization can detect nucleic acids and is used to reveal specific genetic mutations and to measure gene expression with high-spatial resolution in tissue sections [2]; enzyme histochemistry can be used to measure, not only the amount, but the activity of an enzyme [3]; colloidal gold staining techniques coupled with electronic microscopy have allowed to localize specific antigens with nanometric resolution [4]. Together, these techniques have vastly contributed to biology and medicine. For

example, histological examination of pathological tissue is necessary for cancer diagnosis and is also often important to choose the best therapeutic option for each individual patient. **In addition, drug discovery strongly relies on histological techniques.** In order to assess whether a compound is active in animals, one can examine the drug target via histological techniques and confirm if its level is indeed modulated by the drug. New compounds should also be tested for potential toxicity. Regulatory institutions such as the *Food and Drug Administration* and the *European Medicines Agency* regularly issue guidelines for drug discovery. These guidelines include a number of requirements for toxicity assessment using histology. For example, The *European Medicines Agency* requires that at least 37 organs should be histologically examined for safety assessment in repeated-dose animal studies [5]. Even though, histology is an old discipline, its use is as important as ever and, interestingly novel advances are still pushing its boundaries even further.

One front of investigations concerns multiplexed IHC. Indeed, if classical immunofluorescence allows to observe several markers on the same sample, it is usually limited to two or three markers. The main reason for this is that fluorescent proteins that are used as dyes have relatively large emission spectra, thus restricting the possibilities to use them together without overlapped emission. To circumvent this, one advance has been to develop fluorescent reporters with narrower emission peaks such as quantum dots [7]. Recently, 2 groups have proposed an approach that combines immunohistochemistry with mass spectrometry [6, 8]. Antibodies are conjugated with metal isotopes which are then detected through mass spectrometry. This allowed the authors to simultaneously image up to 32 different markers (theoretically, around a hundred markers could be stained on the same section without major overlap) but the technique is currently relatively slow (it takes about 2h to image a field of view of $500 \mu\text{m}^2$ at microscopic resolution). Clarification is another vibrant area of research and it has drawn major interest, especially from the neuroscience community. **Clarification** is a tissue processing procedures that removes lipids from organs which then become transparent to light. The advantage of clarification is that it enables to image the inside of an organ without losing structural integrity due to physical sectioning. A number of techniques have been proposed for this purpose [9, 10, 11, 12]. Clarification has been used to image brains from transgenic mice that express fluorescent proteins and thick sections stained by IHC [13]. However, it seems that one current limitation of clarification methods for intact organ IHC is that antibody penetration in thick tissues is very slow and hardly exceeds a few hundred micrometers [13]. Besides, optically imaging deep

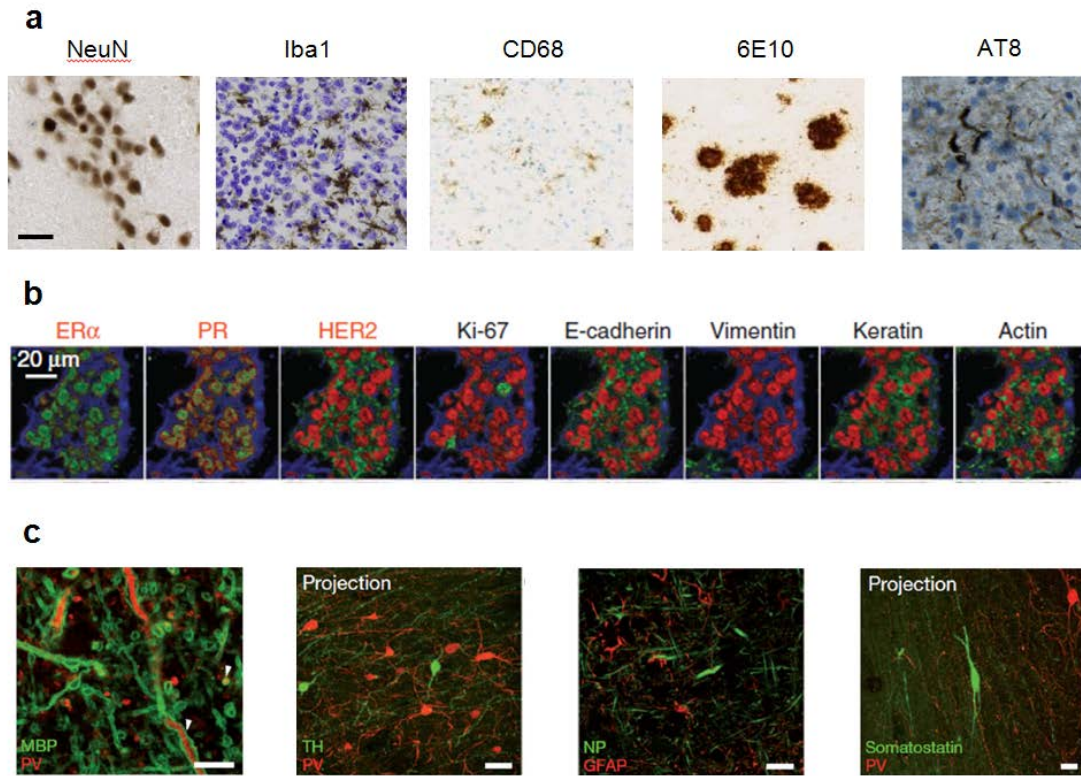


Figure 1.3: IHC staining techniques. (a) IHC staining in the brain. From left to right: neuronal staining with NeuN IHC, microglia staining with Iba1 IHC and a Nissl counterstaining, phagocytic cells staining with CD68 IHC and a light Nissl counterstaining, A β plaque staining using 6E10 IHC and neurofibrillary tangles staining with AT8 IHC and a Nissl counterstaining. (b) Multiplexed IHC of a breast tumor tissue section using mass spectrometry imaging. 8 markers of interest are shown in green, cell nuclei are in red (dsDNA staining) and hematoxylin staining in blue (images taken from [6]). (c) 3D thick section imaging thanks to prior tissue clarification.

CHAPTER 1: CONTEXT

inside organs raises the risk of resolution loss because of light scattering within the sample before reaching the microscope. If clarification techniques were to become widespread, it can be expected that optimized protocols for intact organ IHC will be developed. Finally another source of recent innovation come from new technologies for image acquisition and novel methods for histology image analysis. This will be discussed in more details in the two next sections.

1.1.2 Histology imaging

The goal of histology imaging is to obtain finer structural details about the tissue under study than is possible with the naked eye. The level of detail provided by an imaging device depends on spatial resolution which is defined as the minimum distance by which two observed objects must be separated to be resolved by the device. The Abbe distance can be used to approximate the resolution limit of an imaging device:

$$d = \frac{\lambda}{2n \sin \theta}, \quad (1.1)$$

where λ is the wavelength of the imaging radiation, n is the index of refraction of the medium between the tissue section and the objective and θ is half the angle of the image-forming cone of the imaging system (numerical aperture, Figure 1.4). The finest resolution achievable by an imaging system is diffraction limited and, according to Abbe's theory, can be improved by reducing the imaging radiation wavelength, by increasing the numerical aperture of the objective or by using media with larger index of refraction.

Broadly speaking, histology imaging devices fall into one of the following 3 categories: electron microscopes, fluorescence microscopes and bright-field microscopes. We will briefly describe the two first categories and then focus on bright-field imaging which was used throughout this work. Electron microscopy is used to image tissue samples with nanometric resolution. Compared with optical microscopy, higher resolution are attained because the electron radiation have shorter wavelength ($\approx 10^{-3}$ nm) as compared with visible light (400-800 nm). Contrast between the structures of interest and the remaining tissue require staining the section with heavy metal salts that can absorb or scatter electrons. **Electron microscopy** enables to resolve fine details of the intracellular architecture such as neuron's synaptic vesicles [14]. A lot of effort is currently undertaken to scale-up ultra-structural investigations from the single-cell level to the system-level [15, 16].

In **optical microscopy**, contrasts relies on various phenomena arising from the

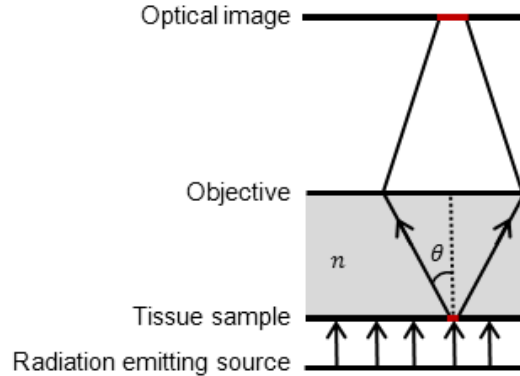


Figure 1.4: A simple one length imaging system.

interactions between photons from the light emitting source and electrons within the sample. In the case of **fluorescence imaging**, the stained tissue sample is penetrated by light of a specific color. The light emitting source is typically a laser or a white light lamp with an appropriate filter. Fluorescent dye's electrons within the sample get specifically excited by this light and then decay to their ground state by emitting photons of a lower wavelength. The emitted light is then collected by the objective to form the optical image and a camera records the digital image. Fluorescence microscopy is particularly popular in biology and a vivid area of research as demonstrated by advances for 3D imaging using laser scanning microscopy or 2-photon microscopy [17] and for sub-diffraction limit imaging with stimulated emission depletion microscopy and stochastic optical reconstruction microscopy [18, 19]. In contrast to fluorescence imaging, **bright-field imaging** uses white light illumination. When traversing the tissue sample, light gets attenuated at specific wavelengths by dyes (either by photon absorption or photon scattering). The transmitted light is gathered by the objective to form the optical image which is then digitized by a camera.

The choice between using fluorescence or bright-field imaging largely depends on the application. If using fluorescence, one can image multiple markers on the same section by choosing secondary antibodies coupled with fluorescent dyes which emission spectra are well separated. However, biological tissues are naturally fluorescent (autofluorescence), which impedes immunohistochemical signal detection. Besides, repeated imaging sessions of the same sample alter the dye resulting in decreased intensity (photobleaching). Bright-field imaging is faster than fluorescence imaging and the sections can be observed a great number of times without alteration but multiplexed immunostaining is practically very hard. One shared limitation of fluorescence and brightfield microscopy is that because the image field-of-view (FOV) is inversely proportional to the objective magnification, the fraction of a tissue section that can be imaged at high-resolution is relatively small.

Several approaches have been proposed to image whole tissue sections. To circumvent the problem of small FOV, one solution has been to motorize the microscope stage. The tissue section is successively imaged and then moved to the next position. The positions form 2 dimensional grid with constant spacing corresponding to the image FOV size. A set of small FOV tiles with known positions are collected and subsequently stitched together to provide the final digital whole-slide image. A number of commercial motorized microscope are available as well as "do it yourself" solutions [20]. Such microscopes, however, can only image one slide or at best a

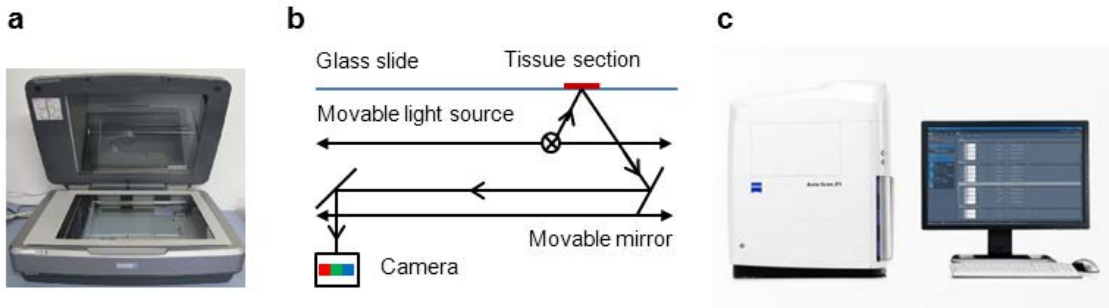


Figure 1.5: Whole-slide imaging systems. (a) A flatbed scanner (ImageScanner III, GE). (b) Flat bed scanner functioning. (c) A Whole-slide imaging scanner (Axio ScanZ.1, Zeiss). Note that for visual comfort, the two systems are not displayed at the same scale.

few slides per session which hinders their use when dealing with large amount of histological material. In order to image whole sections with high-throughput, our laboratory has proposed to use flatbed scanners. Flatbed scanners are commonly used in biochemistry to digitize electrophoresis gels and their functioning is different from microscopes. Slides are positioned on a glass slide which is progressively illuminated by a movable light emitting source and the transmitted light is collected by a camera on the fly. The number of slides that can be imaged in a single session only depends on the scanner effective surface and scanning time is fast compared with microscopy which results in very good imaging throughput. However, the main limitation of flatbed scanners is that their spatial resolution is limited by the camera resolution. Typically, a good commercial flatbed scanner can digitize images up to a few micrometers (μm) of resolution. As we will see in section 2.2, this resolution is sufficient to study some neuropathological markers such as $A\beta$ plaques but is too rough to image cells. Recently, so called “**whole-slide imaging scanners**”, “**whole-slide imaging microscopes**” or “**virtual microscopes**” have emerged as a leading technology to image a large number of whole sections at high resolution (Figure 1.5c). Whole-slide imaging microscopes integrate optical microscopy, robotics and software to seamlessly handle and image a large number of slides (typically between 10 to 200 depending on the system). Whole-slide images are obtained either by, similarly to motorized microscopes, acquiring tiles or by, similarly to flatbed scanners, scanning lines. In both cases, tiles or lines images are stitched together by the integrated software to obtain the final whole-slide image. In this work, we will abundantly use flatbed scanning and to some extent whole-slide imaging bright-field microscopy (Figure 1.5).

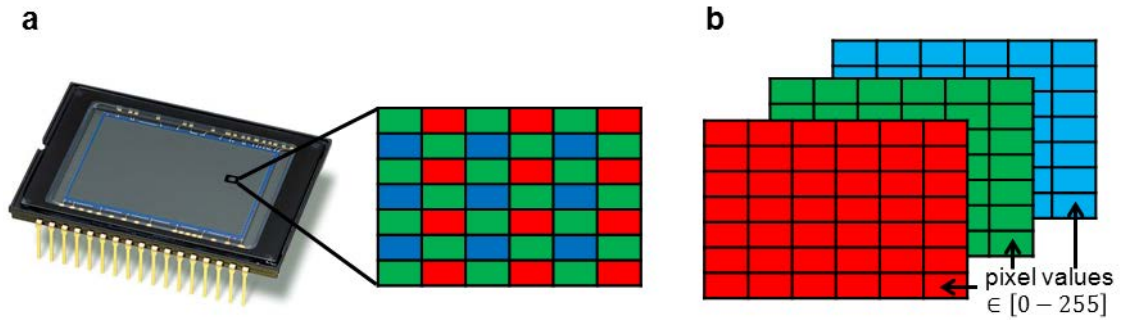


Figure 1.6: Color image digitization. (a) A CCD sensor with a Bayer mosaic filter on top. (b) 3 channels from an *RGB* image.

An essential aspect of histology imaging is the digitization process. It consists in converting the analog optical image into a digital image. A two-dimensional (2D) optical color image can be viewed as a bivariate continuous distribution of the light intensity for each wavelength of the visible light spectrum. The digital image is a discrete approximation of this optical image. In most microscopes, digitization is performed using coupled-charge device (CCD) cameras. A CCD camera consists of a large number of light sensitive elements arranged in a 1D or 2D array fashion. The photoactive region of the CCD consists of a layer of metal oxide semiconductor which converts the incoming photons into electrons. Electron are then stored and the signal is transferred to an analog-to-digital converter that assigns a digital value corresponding to the signal intensity. As CCD cameras cannot differentiate colors, a color filter array can be placed over the photoactive region to filter red (*R*), green (*G*) and blue (*B*) colors in order to reconstruct the color optical image (Figure 1.6a). Digital color images are arranged on a 2D array of pixels. Each pixel value is encoded as 3×8 -bits unsigned integer value (Figure 1.6b).

Several parameters are important for proper image digitization. As a matter of fact, digitization can be a source of significant image deterioration due to **noise**, **aliasing** and **geometric distortions**. Fortunately, commercial solutions are usually designed to minimize these problems as much as possible. The crucial parameter to be defined by the user is the image resolution. The resolution should be high enough to resolve the objects of interest within the tissue section, however, high-resolution comes at a cost in term of digitization time and file size. Image size increases proportionally to the square of magnification so that high-resolution whole-slide images typically consists of millions of pixels. For example, a single mouse brain tissue section at a resolution of $0.44 \mu\text{m}$ consists of approximately 500 millions pixels

which corresponds to a file of around 1.5 GB of size. High-throughput digitization techniques constitutes a great opportunity for researchers in neurology and more generally in biomedical sciences to access large amount of information on tissue organization and composition. Nevertheless, managing and analyzing large collections of whole section images is a challenging task that requires dedicated methods. In the next section, we will review current methods for analyzing neuropathology section images.

1.1.3 Histopathological biomarkers quantification

One essential question that arises during histological investigations is how much of a given marker is present in a tissue of interest. As histological processing relies on tissue sectioning, answering this question involves two steps: (1) evaluate the amount of marker in tissue section images and (2) infer the marker quantity at the tissue-level using data obtained from the sampled tissue sections. The first step has been thoroughly investigated and is still a source of innovations but, interestingly, the second step has been relatively poorly addressed in the literature. Here, we will mostly focus on available methods to address the first step, while the second aspect will be the topic of section 4.3.3. After reviewing general aspects of histopathological marker quantification, we will focus on available methods for pathological markers quantification in brain tissue section images.

Contrary to quantitative imaging modalities, such as positron emission tomography and autoradiography, where the imaging signal is directly related to the quantity of radioactive tracer within the tissue, **histology imaging provides contrasts that are not directly related to the underlying amount of marker of interest**. Depending on the nature of the investigated histopathological marker, 2 different approaches can be employed:

- **Pixel-level quantification** relates to the fraction of pixels that are considered to be positively stained within the tissue.
- **Object-level quantification** consists in detecting objects as groups of connected pixels according to some criteria and to evaluate the number of objects within the tissue.

In this work, we will mostly study neuropathological markers of Alzheimer’s disease. Pathological markers are by definition, not well-defined objects, thus, the question that we will try to answer relates to how much of the tissue is affected

by pathological markers. Therefore, the pixel-level quantification approach is usually more biologically relevant than the object-level quantification. On the contrary when studying cellular markers, object-level quantification is often more relevant because cells have a clearly defined structure and are separated from each other by their membrane. Many algorithms have been developed for computer-based cellular object-level quantification, mostly in the context of tumor histopathology [21].

Another important aspect concerns the scale in which is expressed marker quantification:

- **Categorical scale:** tissue samples are assigned to one of a few ordered categories. For example, the Braak stages consist of 6 categories and are used by pathologists to evaluate the severity of neurofibrillary tangle deposition in Alzheimer’s disease [22]. Sometimes this approach is referred as *semi-quantitative*.
- **Continuous/discrete scales:** in the case of pixel-level quantification, the fraction of positively stained pixels is a positive continuous random variable. In the case of object-level quantification, object count is a positive discrete random variable.

Categorical scales are very common in clinical practice. In research settings and especially in preclinical research, continuous/discrete scales are often preferred because they allow for more nuanced description of the tissue sample than categorical scales.

At the beginning of this work in 2013, we did a literature survey on methods for neuropathological marker quantification. We focused on articles referenced in the NCBI database (<http://www.ncbi.nlm.nih.gov>) that included a protocol to quantify the **A β load** (*i.e.* the fraction of tissue occupied by A β plaques) in mouse models of Alzheimer’s disease. Among those publications, 51 were chosen for further analysis. Articles were selected based on journal impact factor (2012 impact factor had to be at least equal to 2) and if the quantification method was adequately described. Results from the survey are shown in Figure 1.7. In our publication sample, most of the scientists analyzed a total of 3 to 6 sections per brain and defined 1 or 2 regions of interest (ROIs) on tissue section images prior to analysis. Once ROIs were specified, a variety of A β plaque quantification methods was used. The different methods fell into one of these 3 categories: “manual”, “stereology” and “segmentation”. **Manual techniques** refers to a minor fraction of protocols that rely on manual counting or manual delineation of A β plaques within ROIs.

Stereology also involves manual quantification but it relies on a set of rules from sampling theory to ensure that the marker quantification estimate is unbiased. A famous stereological technique is the *Optical Fractionator*, where an operator counts all positively stained objects within a set of regularly spaced frames [23]. Manual and stereological techniques are both labor intensive and thus usually restricted to limited parts of the brain. Besides, while stereology ensures that the estimate is unbiased in the sense that its expected value is equal to the true parameter value, it cannot ensure that the actual estimate is close to the true parameter value.

In our sample of publications, the most common approach for $A\beta$ load quantification relies on **image segmentation**. A simple way of segmenting a grey-scale 2D image $I(x)$ into background and foreground classes is to apply an intensity threshold:

$$M(x_i) = \begin{cases} 0 & (\text{Background}), \text{ if } I(x_i) < T \\ 1 & (\text{Foreground}), \text{ if } I(x_i) \geq T \end{cases} \quad (1.2)$$

where $M(x)$ is the thresholded image, and later referred as the **binary mask**, and T is the threshold. In the context of $A\beta$ load quantification, one can generate a binary mask for the tissue and a binary mask for $A\beta$ plaques and then simply calculate the **ratio** between the $A\beta$ plaque surface and tissue surface. Thresholding is a simple and computationally efficient way to quantify histopathological markers which explains why it is so popular. Segmentation is very sensitive to the threshold which, in turn, needs to be carefully adjusted. In our sample of publications, most often threshold was manually defined by an operator and then applied to all images in the dataset. Thresholding works best in cases of strongly contrasted and very reproducible staining. Adaptive thresholding has been proposed for $A\beta$ plaque segmentation in cases when the staining is uneven within or between sections [24]. In adaptive thresholding, images are partitioned into non-overlapping blocks and a threshold is automatically computed for each parcel using, for example, the Expectation-Minimization algorithm (EM) (Figure 1.8a) [25].

Another possibility to segment images is to use **machine learning classification** algorithms. This approach has several advantages compared to thresholding: (1) while thresholding is performed using only grey-scale information, machine learning algorithms can **integrate several, hopefully informative, features**, (2) machine learning algorithms can often be seamlessly extended to **more than 2 classes**, (3) in the case of **supervised classification**, algorithms can be **trained** to generate more relevant segmentation. Given a **training set** $Z = \{x_i, y_i\}_1^n$ of n pixels with feature vector $x_i \in \mathbb{R}^m$ and ground-truth class $y_i \in [1, \dots, k]$, the goal of

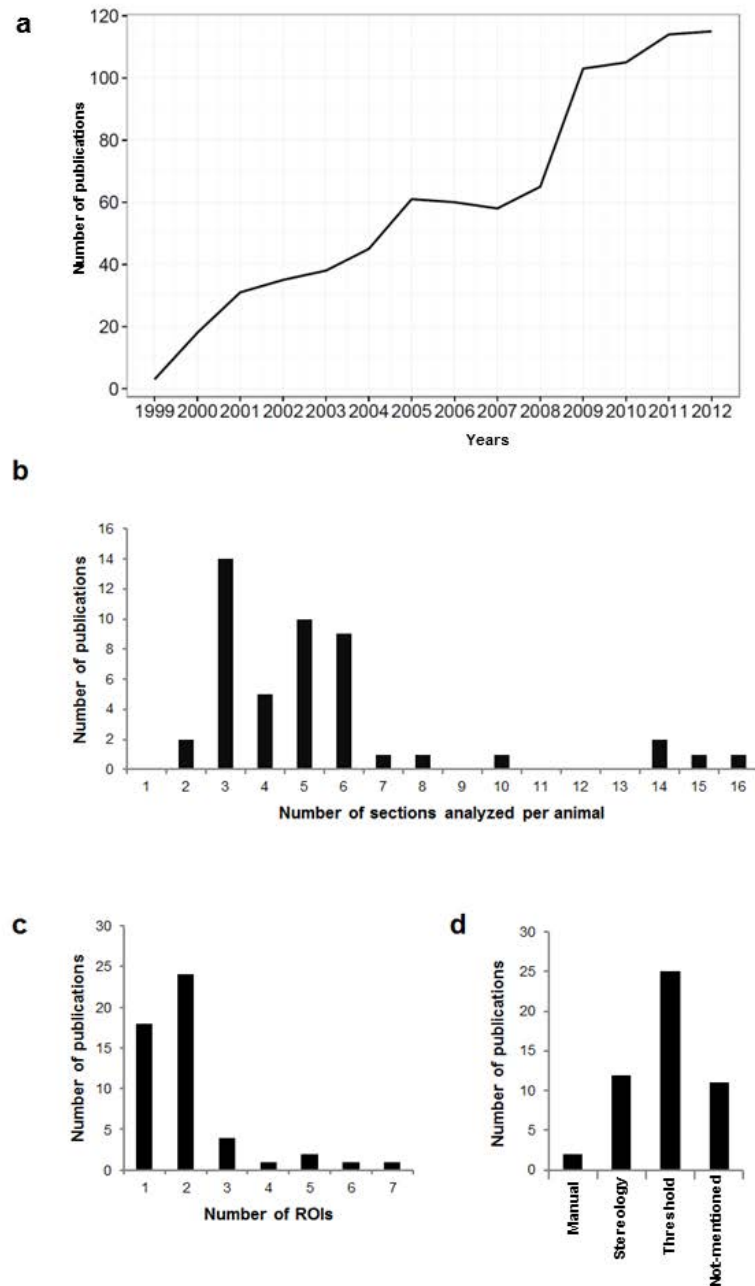


Figure 1.7: Literature survey of $A\beta$ load quantification. (a) Evolution of the number of publications that quantify $A\beta$ deposition in mouse models of AD over the 1999-2012 period. Histograms with number of sampled sections per animal (b), number of investigated ROIs (c) and quantification techniques (d).

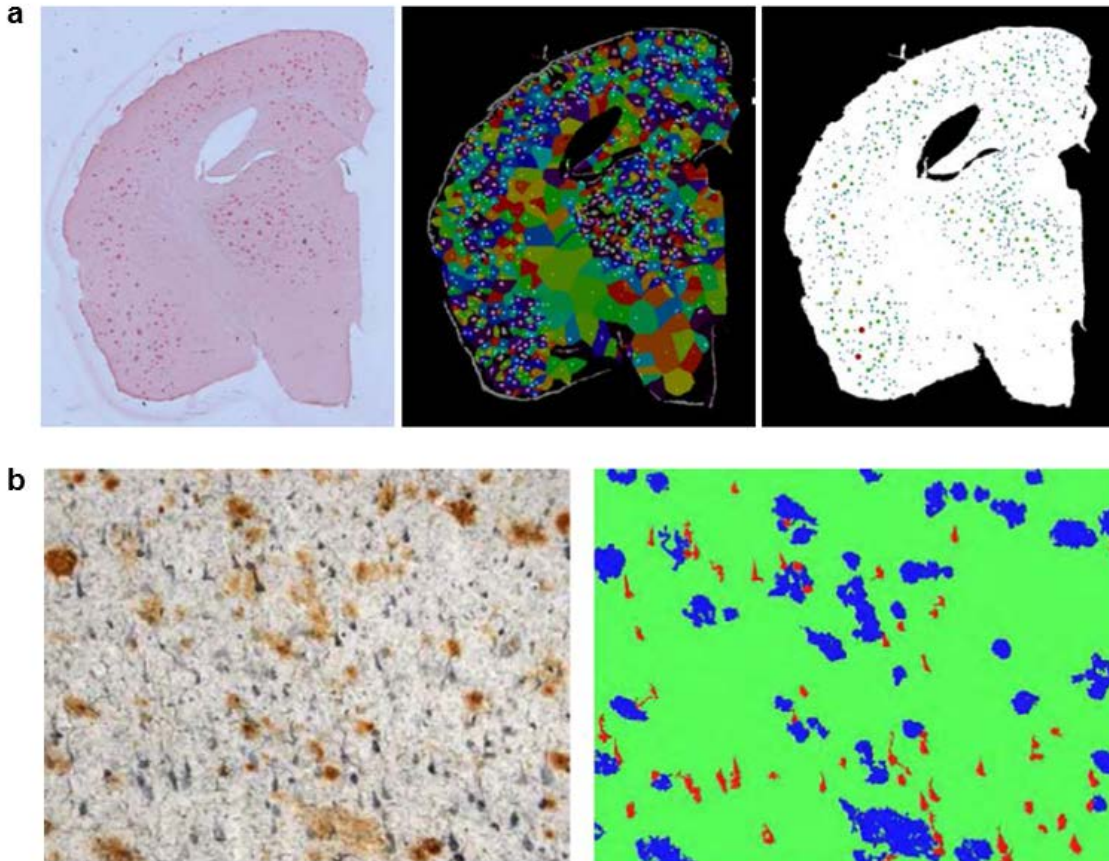


Figure 1.8: Neuropathological markers segmentation. (a) Adaptive thresholding from Feki *et al.*. The image is partitioned with Voronoi tessalation and a threshold is fixed within each Voronoi cell to segment $A\beta$ plaques. (b) 3-class supervised classification with BioVision. On the right panel, background appear in green, neurofibrillary tangles in red and $A\beta$ plaques in blue.

supervised classification is to find a function $Q : X \rightarrow Y$ which can be then used to predict the class of non-annotated pixels.

In Chubb *et al.* [26], authors propose a supervised classification approach, called **BioVision** to segment neuropathological markers of Alzheimer’s disease (Figure 1.8b). In the learning step, BioVision extracts RGB and local intensity features from ground-truth manually annotated images which leads to a 4-dimensional feature vector for each pixel. Local intensity can be calculated for each pixel of the histology image as the mean of the RGB intensity values within a defined neighborhood of pixels. BioVision then estimates the features joint probability density for each class

$j \in [1, \dots, k]$ using **Gaussian Mixture Models** (GMM):

$$f_x(x|y = j) = \sum_{l=1}^s \frac{\rho_l}{(2\pi)^2 \sqrt{|\Sigma_l|}} e^{-\frac{1}{2}(x-\mu_l)^T \Sigma_l^{-1} (x-\mu_l)}, \quad (1.3)$$

where, for each component l , ρ_l is the mixing coefficient, μ_l is the mean and Σ_l is the co-variance matrix of the 4-dimensional Gaussian distribution. Component means and co-variance matrices as well as the number of Gaussian components s are determined via a temperature minimization algorithm [27]. In the **classification step**, the conditional probability that a pixel x_i belongs to class j can be obtained via Bayes rule:

$$P(y_i = j|x_i) = \frac{P(y_i = j)P(x_i|y = j)}{\sum_{a=1}^k P(x_i|y = a)}, \quad (1.4)$$

where $P(y_i = j)$ is obtained by computing the fraction of pixels of class j in the learning set. Finally, each pixel is assigned to the class that maximizes $P(y_i = j|x_i)$.

BioVision is computationally efficient and shows higher accuracy compared to threshold based methods. As a matter of fact, BioVision algorithm was implemented in our laboratory and used at several occasions during this work. In section 2.4, BioVision shortcomings will be discussed and a new method for neuropathological markers segmentation will be presented for cases where BioVision does not suffice to provide robust segmentation.

1.2 Alzheimer’s disease

1.2.1 Impact on public health

Thanks to improved health care over the last decades, people live longer than ever before. One of the main challenges that come with longer lives is the increasing prevalence of dementia. It is estimated that between 25 and 35 million people are affected by dementia worldwide and this number is expected to double every 20 years [28, 29]. Dementia is a syndrome that is characterized by a progressive loss of cognitive function. A variety of conditions can cause dementia including cerebrovascular accident, Parkinson’s disease and, most frequently, Alzheimer’s disease.

As in other dementias, patients with Alzheimer’s disease experience progressive loss of memory, communication and judgment skills. Studies suggest that it is possible to prevent the onset of Alzheimer’s disease symptoms. Higher education, leisure

activities in elders, regular physical activity and some diets have been associated with lower risk of Alzheimer's disease but more studies are needed to confirm this [30, 31]. Unfortunately, once people show signs of cognitive decline, no drug can slow its progression. Besides loss of cognitive functions, patients also present high risks of cardiovascular and psychiatric co-morbidities [32, 33]. While the disease progresses, they become less autonomous up to a point when they become fully dependant on caregivers. Eventually, patients with Alzheimer's disease die between 3 to 7 years after the initial diagnosis [34].

Alzheimer's disease is an important burden in our society. Family members often spend substantial amount of time and energy to care their relatives. After a period of relative autonomy, patients often needs institutionalisation which comes at important costs for the family and the society. Also, as patients have co-morbidities and tend to under-report medical problems, hospitalisation-associated costs are higher than for healthy elders [35]. The World Health Organization has estimated the global worldwide cost of Alzheimer's disease to be of 555 billion euros in 2010 which corresponds to about 1% of the world's gross domestic product.

Despite this situation, Alzheimer's disease receives relatively less attention from the public and researchers than other major public health concerns such as cancer or cardiovascular diseases. One reason for this is that patients with Alzheimer's disease are isolated and do not communicate about their illness nor do they form strong patients associations. Furthermore, Alzheimer's disease lack of public understanding because it is an abnormal conception that a medical condition can severely impact mental abilities. In recent years, public awareness is increasing as witnessed by national plans to prioritize this major health issue in France and other countries. In addition, consortia in imaging and genetics have been formed to foster research on Alzheimer's disease. Efficacious drugs to treat Alzheimer's disease are still pending but research on pathological mechanisms is moving forward at a fast pace.

1.2.2 Pathological hypotheses

Progressive and extensive neuronal death is responsible for the cognitive impairment in **Alzheimer's disease**. In 1907, using histochemical techniques, Alois Alzheimer reported the case of a patient who suffered cognitive decline and which brain was affected by neuronal death and the presence of pathological deposits. Since then, the role of the two neuropathological hallmarks of the disease described by Alois Alzheimer, $A\beta$ plaques and neurofibrillary tangles, has been vastly studied. Alzheimer's disease pathophysiology is fundamentally progressive and symptoms

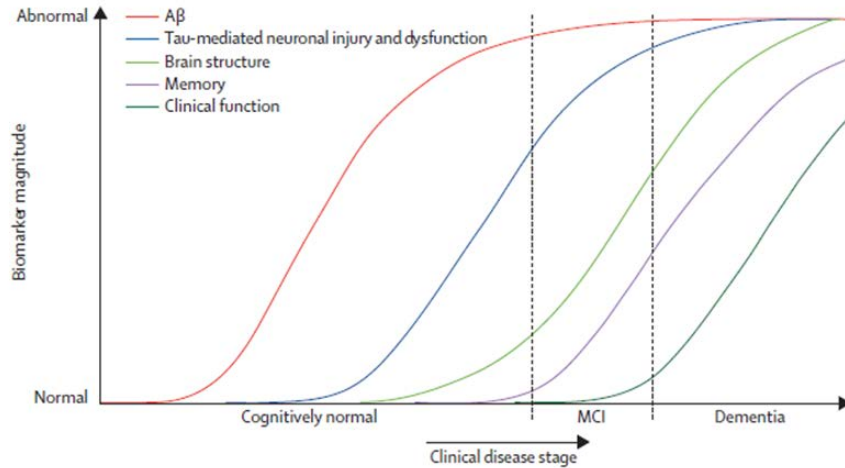


Figure 1.9: Progression of Alzheimer's disease biomarkers with disease course (image from Jack *et al.* [36])

appear long after the initiation of the pathology (Figure 1.9). Along the disease progression $A\beta$ pathology, neurofibrillary tangles, neuroinflammation and brain glucose metabolism impairment are successively implicated and interact with each other in ways that are yet to be fully described.

The first event during the disease course seems to be the appearance and spreading of the $A\beta$ pathology. $A\beta$ plaques are extracellular deposits made of aggregated $A\beta$ peptides. Amyloid Precursor Protein (APP), a membrane protein which function is not yet fully understood, is metabolized into several peptides including the $A\beta$ peptides. The cleavage of APP into $A\beta$ peptides involves the successive action of two proteic complexes: the β -secretase and the γ -secretase which most important constituents are the Presenilin-1 (PS1) and Presenilin-2 (PS2) proteins. The **amyloid cascade** hypothesis states that the over-production of $A\beta$ peptides triggers a range of neurotoxic and neuroinflammatory effects resulting in synaptic dysfunction and eventually neuronal death [38] (Figure 1.10). Because of their structure $A\beta$ peptides are prone to aggregation under high concentrations and rapidly form small oligomeric assemblies which then aggregate to form mature plaques. Oligomeric forms of $A\beta$ peptides have been shown to be particularly toxic for neurons and $A\beta$ plaques have been shown to alter synaptic function in their periphery [39, 40]. In turn, synaptic activity seems to increase $A\beta$ peptide secretion [41]. In favor of the amyloid cascade hypothesis is the discovery of polymorphisms on the APP, PS1 and PS2 genes which cause familial forms of Alzheimer's disease [42, 43, 44]. In these rare forms of Alzheimer's disease, genetic mutations result in a dramatic in-

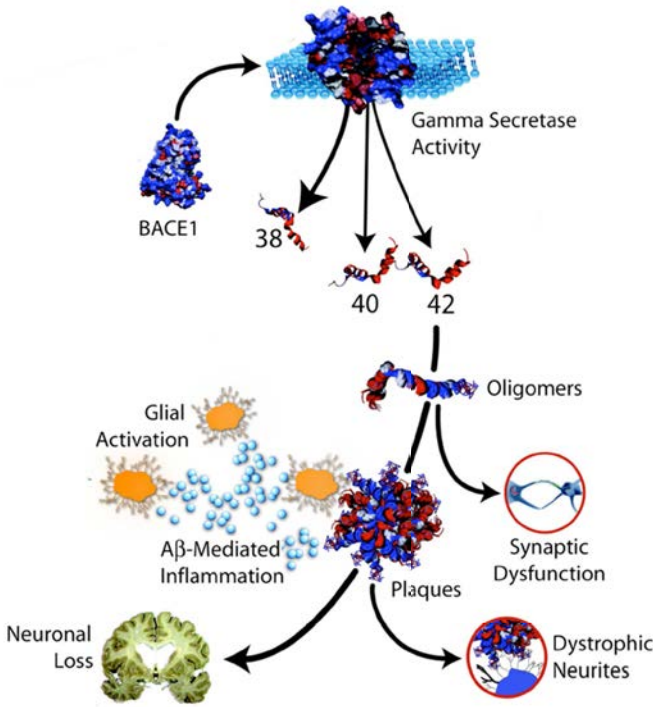


Figure 1.10: Amyloid cascade hypothesis (modified from Imbimbo *et al.* [37]). The APP is catabolized into several $A\beta$ peptide species which assemble in oligomers that have toxic properties on synapses. Eventually oligomers gather into plaques that trigger inflammation.

crease of the APP metabolism and a severe accumulation of $A\beta$ plaques. Besides, the strongest genetic risk factor for sporadic Alzheimer's disease is the ApoE gene which is implicated in $A\beta$ clearance from the brain. While $A\beta$ pathology is clearly at the origin of familial forms of Alzheimer's disease, its role in the sporadic form is debated. Repeatedly, studies have shown no clear correlation between the $A\beta$ load and cognitive function in Alzheimer's disease [45]. In addition, it seems that a minority of patients diagnosed with Alzheimer's disease do not display $A\beta$ deposition at all [46]. This could indicate that other mechanisms may be central in the sporadic form of the disease or that Alzheimer's disease regroups distinct pathologies yet to be clearly defined. Another argument against the amyloid cascade hypothesis is the failure of drugs targeting the $A\beta$ pathology. Several therapeutic strategies have been tested in clinical trials for either lowering the production of $A\beta$ species through β - and γ -secretase inhibitors or for increasing $A\beta$ species clearance with anti- $A\beta$ immunotherapies but results on cognitive impairment have been disappointing. Nonetheless, anti- $A\beta$ immunotherapies have shown promising results to slow the disease progression in patients with mild cognitive impairment or sub-clinical Alzheimer's disease [47]. This is in line with recent studies suggesting that the $A\beta$ pathology starts as early as 25 years before the onset of the disease and would have a role in the early progression of the disease rather than in the late stages of cognitive impairment [48]. Recently, PET radio-tracers for $A\beta$ pathology have been marketed (Figure 1.11). Hopefully, these radio-tracers will enable to detect patients with early-stage Alzheimer's disease and to better select patients that can respond to anti- $A\beta$ therapeutics.

While $A\beta$ plaques are extra-cellular, neurofibrillary tangles resides within cells. They are formed by the accumulation of the **hyperphosphorylated Tau protein** which is important for axonal stability. Similarly to the $A\beta$ pathology, neurofibrillary tangles spread by succesively affecting functionally connected brain areas [50]. The relationship between $A\beta$ and Tau pathologies is yet to be fully understood but it seems that $A\beta$ peptides influence Tau phosphorylation which in turn results into Tau aggregation [51]. In contrast to the $A\beta$ pathology, Tau pathology strongly correlates with cognitive impairment in Alzheimer's disease. Cognitive deficits associated with Tau aggregation seems to result from both normal Tau protein loss of function and from a gain of toxic functions.

Both $A\beta$ plaques and neurofibrillary tangles trigger neuroinflammation. Astrocytes and microglia, the two cell types responsible for neuroinflammation, respond to brain insults by releasing pro-inflammatory signals attracting more neuroinflam-

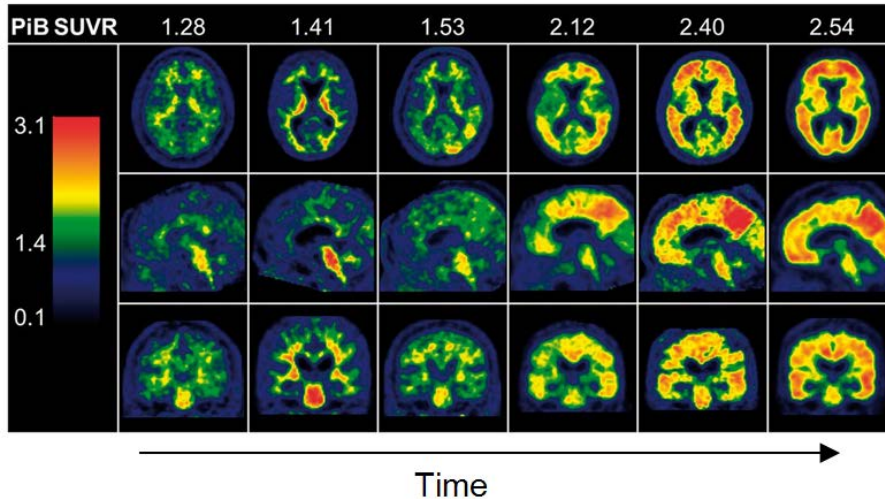


Figure 1.11: Positron emission tomography imaging of $A\beta$ pathology with the PIB radio-tracer at different stages of the pathology (image from Murray *et al.* [49])

matory cells to the site of the injury. Neuroinflammatory cell seems to have an ambiguous role in Alzheimer’s disease [52]. On the one hand, they participate in protecting the brain by eliminating pathological aggregates. On the other hand, they release toxic compounds that are harmful to neurons.

Eventually, the brain structure and function gets significantly altered leading to cognitive deficits. These alterations manifests in the form of a reduction of brain glucose metabolism and a shrinkage of the brain tissue, predominantly in cortical and hippocampal areas.

1.2.3 Preclinical research on Alzheimer’s disease

Substantial knowledge about Alzheimer’s pathophysiology comes from **animal studies**. $A\beta$ plaque and neurofibrillary tangle deposits have been observed in some species including dogs, cats and non-human primates [53, 54] but the presence of Alzheimer’s disease neuropathological markers in animals does not strongly correlates with neuronal death or cognitive decline. Nevertheless, in mouse lemurs, a well-studied small non-human primate, brain atrophy and cognitive decline appear in a small fraction of old animals but this is not correlated with $A\beta$ and neurofibrillary tangle deposition [55]. For ethical and practical reasons, non-human primates are not commonly used as models of Alzheimer’s disease and mouse models have been developed.

As mouse do not naturally develop Alzheimer’s disease, transgenic mouse mod-

els have been developed to mimic the pathology. APP, PS1 and PS2 mutations found in familial forms of Alzheimer's disease have been transferred to mice which resulted in the generation of a number of lines of transgenic mice harboring single or multiple mutations. These mice typically show increased production of $A\beta$ peptide, $A\beta$ plaque deposition and Tau hyperphosphorylation but they do not present neuronal death or neurofibrillary tangles [56]. Nonetheless, $A\beta$ plaque deposition seems to have a wide range of effects in these mice including synaptic impairment and moderate cognitive deficits [56]. Also, 3D-autoradiography studies in our laboratory suggest that transgenic mouse models of Alzheimer's disease present brain glucose metabolism that resemble early Alzheimer's disease [57, 58]. Triple transgenic mice harboring APP, PS1 and Tau mutations found in rare forms of familial human Tauopathies have been developed in order to model the full range of pathological markers in Alzheimer's disease. These mice develop $A\beta$ plaques and neurofibrillary tangles with time and synaptic dysfunction but only moderate neuronal death and cognitive impairment [59].

Since 1995, when the first transgenic mouse models of Alzheimer's disease became available [60], many therapeutics have shown promising results in preclinical studies but failed in clinical trials. Zahs *et al.* argued that preclinical studies fail in to translate into clinical applications because transgenic mouse models resemble to early Alzheimer's disease when patients still do not show signs of cognitive impairment [61]. Recently, many of the drugs that have failed to show any effect in Alzheimer's disease are being investigated again in patients that show first signs of mild cognitive impairment. Since $A\beta$ load PET tracers are available, clinicians can detect patients at risk much earlier than the onset of cognitive impairment and propose them to participate in clinical trials with anti- $A\beta$ therapeutics with the hope that these therapies can slow the progression of the disease before brain damage is too important.

1.3 Motivation

Histopathology is widely adopted to study the organization and composition of tissues. In particular, histology techniques are important for Alzheimer's disease research as they allow to study the amount and spatial distribution of $A\beta$ plaques and neurofibrillary tangles, the two pathological hallmarks of the disease. **In mouse models of Alzheimer's disease, neuropathological markers quantification is essential to evaluate the effect of experimental interventions (drug**

treatments, gene knock-in/-out experiments).

Nowadays, technology for high-throughput histology processing and image digitization exist. However, current methods for the analysis of brain histopathological markers still heavily rely on manual intervention to delineate ROIs and quantify the staining. As shown in the literature survey on $A\beta$ load quantification (section 1.1.3), data collection is usually restricted to a few tissue sections and a few manually defined brain ROIs. This limits the scope of histopathological investigations to tiny portions of the brain. It also heightens the risk of sampling error as well as inter-operator and intra-operator variability.

A solution would be to image and analyze the entire brain in 3D. Several approaches have been proposed for brain *ex vivo* 3D microscopy imaging. Recently, clearing techniques such as ultramicroscopy, CLARITY, SeeDB, CUBIC and 3DISCO, have drawn considerable attention [10, 11, 62]. Clearing protocols have been proposed as a preprocessing step to optically image thick tissues in 3D. Thick tissue immunostaining is possible with some of the aforementioned techniques but it requires long incubations to allow for antibody diffusion [63, 13]. Thus, for practical use, a rodent brain needs to be cut into thick sections before it is stained. So far, 3D reconstruction of section images seems to be the only way to obtain images of entire rodent brains. 3D reconstruction of 2D histology sections has been proposed for brain anatomy visualization in mice [64], primates [65] and humans [66]. Previously in our laboratory, Dubois *et al.* [57] and Lebenberg *et al.* [67] have developed tools to reconstruct brains in 3D and they have used 3D Nissl-histology as an anatomical reference for 3D autoradiography studies. However, to date, there is no generic method for quantifying cellular or pathological markers at the whole-brain level. Also, a pending question is, once pathological markers are properly segmented, how to make sense of large amount of brain histopathological data to provide new biological insight.

This work builds on previously developed methods in our laboratory in the fields of **high-throughput brain tissue processing, staining, image acquisition** and **3D reconstruction of histology images**. The main methodological objectives of this work consists in:

1. **Recovering the 3D geometry of the rodent brain** from 2D tissue section images for **multiple histopathological markers**.
2. **Quantifying neuropathological markers** in large histopathology image datasets in a **robust** way.

3. **Analyzing neuropathological markers differences between groups of animals at the whole-brain level** via:
 - **ontology-based analysis** to detect regional changes at various hierarchical levels of the brain,
 - **voxel-wise analysis** to detect local changes without spatial *a priori*.
4. Using 3D histopathology as a ground-truth for the **validation of *in vivo* imaging modalities**.
5. Initializing the extension from neuropathological markers analysis to **cellular markers analysis**.

3D whole-brain histopathology is applied in three preclinical studies that will illustrate the method and show its benefits for neuropathological markers exploratory analysis. The proposed approach is particularly advantageous when the investigator does not have strong *a priori*, if any, on where to look for an effect and would be keen on having more exhaustive information to avoid missing interesting phenomena. In the context of preclinical research on Alzheimer's disease, this could translate into greater knowledge of the pathology in transgenic mouse models and in a more accurate and reproducible evaluation of drug preclinical efficacy.

Chapter 2

High-throughput 3D histopathology

2.1 Large-scale tissue section processing

This section will present the successive steps needed for obtaining series of stained tissue sections for several markers. First, we describe how this is performed for medium size studies using in-house facilities at MIRCen. Then we will describe how this process can be scaled-up using Multibrain technology (*NeuroScience Associates*).

Brain sectioning

After the mouse brain has been extracted from the skull and frozen, it needs to be cut to collect tissue sections. The brain is first embedded in a blue-colored medium which provides sharp contrast with the pale brain tissue color. Brain sectioning is performed using a cryostat which consists of a refrigerated chamber within which the brain is progressively sectioned with a blade. We adopted the coronal cutting

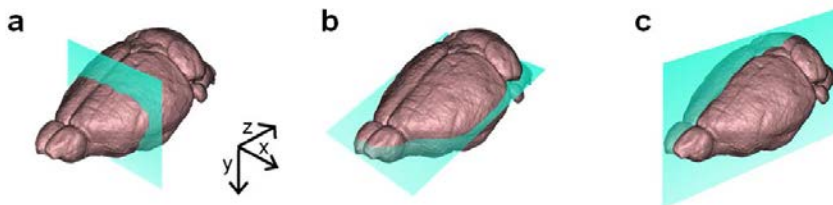


Figure 2.1: A 3D representation of a mouse brain with (a) coronal cutting plane, (b) axial cutting plane and (c) sagittal cutting plane.



Figure 2.2: Block-face photography. Left: A camera device is fixed on top of a cryostat during brain sectioning. Right: Block-face photographs of a tissue section before it is removed from the tissue block.

plane because it is the most practical to collect joint tissue sections encompassing the whole brain (2.1). Sections between 20 and 40 μm of thickness usually ensures good physical integrity which is important for further staining. As the brain rostro-caudal length is about 12 millimeters, approximately 400 sections can be collected for a single brain. This process takes 2 to 3 hours per brain and still heavily relies on manual intervention to maneuver the cryostat and collect the sections.

Block-face photography

Block-face photography imaging is performed in order to keep track of the 3D brain geometry while cutting it. The principle is to record photographs before sections are removed from the tissue block (Figure 2.2). Either a photograph is recorded for every single section or, more frequently, a sampling scheme is adopted with a regular interval between each block-face photograph. The sampling scheme is decided based on the number of histological series that will be further stained. If n histological series are planned, a block-face photograph will be recorded every n sections so that there are as many block-face photographs as the number of tissue sections in each series.

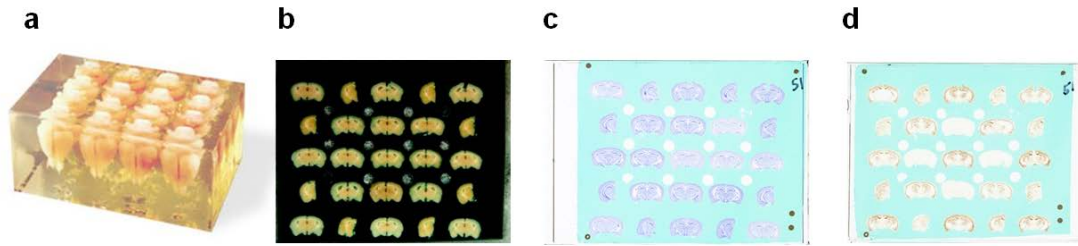


Figure 2.3: Multibrain processing. (a) Brains are all embedded and processed together in a matrix (picture from www.neuroscienceassociates.com). (b) Multibrain block-face photography. (c-d) Multibrain slides with a Nissl staining (c) and an $A\beta$ plaque staining (d).

Serial staining

The total number of collected sections can be divided in several series that are stained for different markers. If, for instance, 4 different markers are to be investigated and, and if the brain is cut into 400 sections, 4 series of 100 sections each will be processed for a single brain. Traditionally, histology staining involves manual handling of tissue sections and chemical reagents but this is not feasible in reasonable time when staining large series of sections. We used an automatic slide staining system (*Ventana Discovery XT*, Roche) which allows us to simultaneously perform IHC staining for 60 standard slides in about 5 hours.

Altogether, brain sectioning, block-face photography acquisition and IHC staining for 1 series can be performed in a single day. Using this protocol, multiple-markers whole-brain histology can be achieved in a timely manner for studies up to about 10 animals. If larger cohorts are to be processed, the multibrain technology provides much higher throughput.

Multibrain processing

The steps of multibrain processing are the same as mentioned above, except that all brains are embedded together in a solid matrix (Figure 2.3). Up to 25 mouse brains can be embedded together and collectively sectioned and stained. The multibrain technology is currently proposed by NeuroScience Associates (www.neuroscienceassociates.com), a contract research organization. Protocols for multiple brain embedding have been described in the literature so it possible to transfer this technology in any histology laboratory willing to increase brain histology throughput [68].

2.2 Whole-slide imaging strategies

A single histological series typically contains 100 sections per mouse brain. Thus, for group-studies with several histological series, thousands of sections need to be digitized. As mentioned in section 1.1.2, high-throughput histology imaging implies the use of dedicated systems such as flatbed scanners and whole-slide imaging microscopes. In the next chapters, both approaches will be used depending on the application. Here, **we will discuss advantages and weaknesses of both systems and how to choose between them.** This will be illustrated with results obtained using systems that were available during this work, namely, the *ImageScanner III* (GE) flatbed scanner and the *Axio ScanZ.1* (Zeiss) whole-slide imaging microscope.

The first and obvious difference between both systems is the **resolution**. Flatbed scanners resolution is limited by the CCD camera and, in our case, ImageScanner III can image sections at resolutions of $25\ \mu\text{m}$ or $5\ \mu\text{m}$. Whole-slide imaging microscopes use lengths to magnify the image. In our case, Axio ScanZ.1 can image sections with $10\times$, $20\times$, $40\times$ magnifications which correspond to resolutions of, respectively, $0.44\ \mu\text{m}$, $0.22\ \mu\text{m}$ and, theoretically, $0.11\ \mu\text{m}$. The scope of what can be resolved with both systems is very different. The flatbed scanner is limited to imaging rather big objects. Brain cells, which vary in size around a few μm , cannot be resolved properly by the flatbed scanner and studying them will require the use of the whole-slide imaging microscope. Figure 2.4a shows an example where neither individual phagocytic cells nor individual Nissl-stained cells can be resolved with the flatbed scanner. In addition to cellular markers, some intra-cellular neuropathological markers such as neurofibrillary tangles may not adequately be resolved as well.

Other types of neuropathological markers such as $A\beta$ plaques or brain blood leakages are clearly discernable with the flatbed scanner (Figure 2.4c). However, the amount of detail is much lower than when using the whole-slide imaging microscope and more noise is introduced by the digitization process. We investigated whether these differences alter $A\beta$ load quantification. A set of 96 sections from brains of 12 transgenic APP/PS1 mice stained for $A\beta$ plaque detection (6E10 IHC) were imaged at both microscopic ($0.44\ \mu\text{m}$) and mesoscopic ($5\ \mu\text{m}$) resolutions. Images were then segmented using BioVision algorithm [26] and the $A\beta$ load was calculated as the percentage of positively stained pixels within the brain tissue. Figure 2.5 shows that quantification at both resolutions is very strongly correlated. While some microscopic details may not be apparent with the flatbed scanner, the overall quantification is very close to that obtained at high-resolution which indicates that

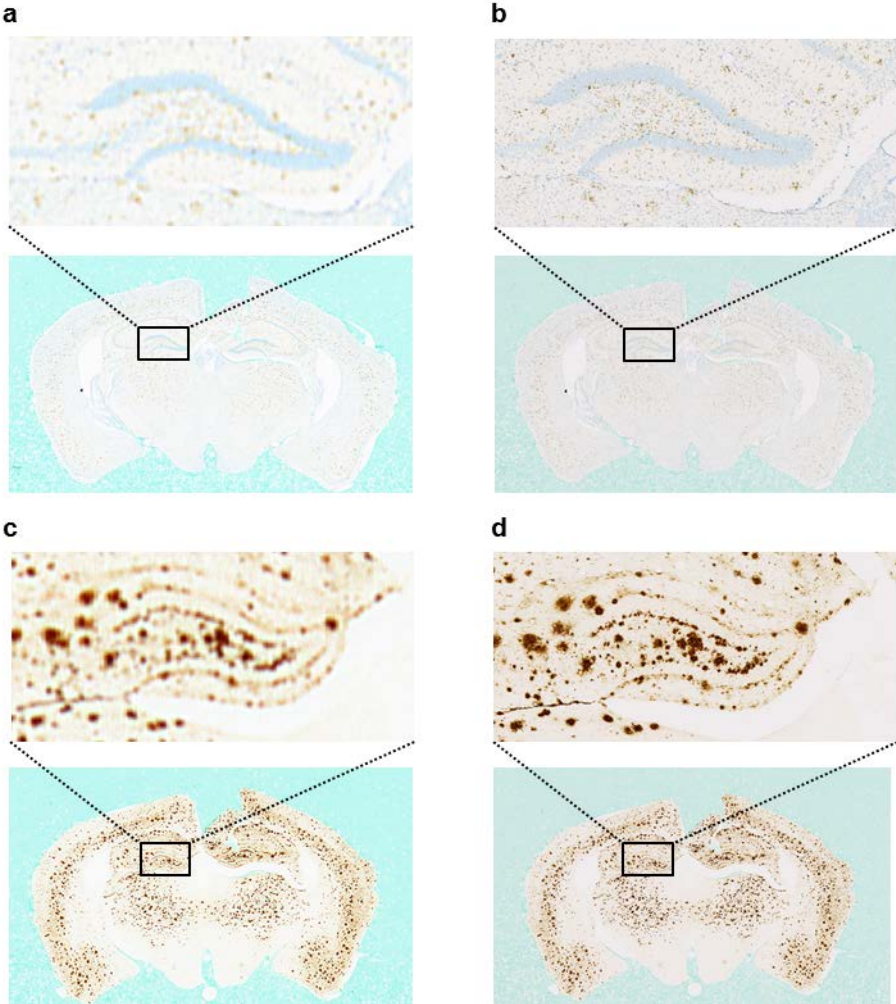


Figure 2.4: Image acquisition with ImageScanner III and Axio ScanZ.1. A section stained for phagocytic cells (CD-68 IHC in brown) and Nissl bodies (Cresyl violet in blue) and imaged with (a) ImageScanner III or (b) Axio ScanZ.1. A section stained for Aβ plaques (6E10 IHC in brown) and imaged with (c) ImageScanner III or (d) Axio ScanZ.1.

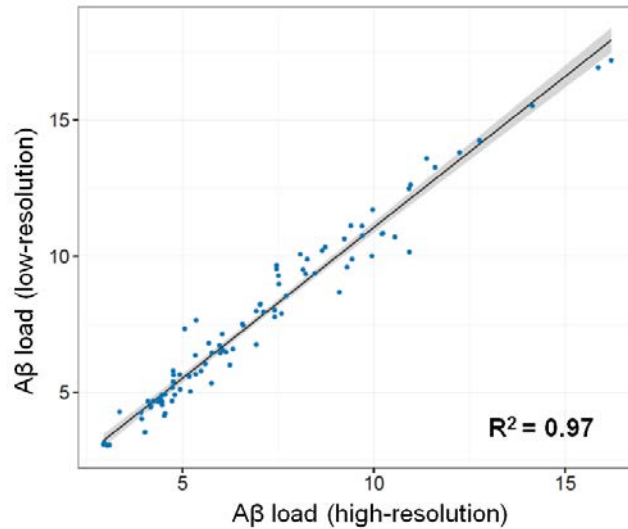


Figure 2.5: $A\beta$ load quantification at high and low resolution. Each dot corresponds to a tissue section image. A linear regression is shown in black with 95CI in grey.

the flatbed scanner is a valid imaging system to study the $A\beta$ load despite the relatively low resolution.

Another important aspects are the scanning **time** and **workload**. The overall time for scanning 100 sections at lateral resolution of $5 \mu m$ is about 2 minutes with our flatbed scanner while, at lateral resolution of $0.44 \mu m$, it takes a few hours with our whole-slide imaging microscope. Flatbed scanner imaging requires less time and workload than when using whole-slide imaging microscopy for the following reasons:

- Lower resolution images are smaller in size and, thus, faster to digitize (it is, however, possible to fairly reduce high-resolution microscopy imaging time by detecting sections on a preview low resolution image and image only these regions at high-resolution).
- Image digitization via line-scan CCD camera is rapid and whole slides images are obtained without tile/line stitching.
- As depth of field reduces with high-resolution microscopy imaging, additional time is needed for fine focus adjustment. Also, sometimes, automatic focusing will fail to find an adequate focal plane and the section will have to be imaged one more time.

In summary, image resolution and quality is better with whole-slide imaging microscopy but overall scanning time is shorter with flatbed

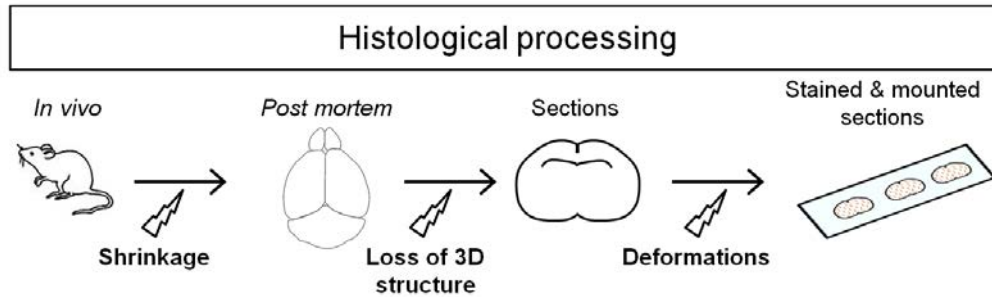


Figure 2.6: Histological processing steps and resulting brain structure insults.

scanning. This latter factor is essential when digitizing large sets of sections. When quantifying large objects, such as $A\beta$ plaques, flatbed scanner imaging seems to be the best option, while studying cellular level markers requires the use of whole-slide imaging microscopy.

2.3 Brain multi-modal 3D reconstruction

Brain structure is subject to several insults during histological processing (Figure 2.6). First, the brain is extracted from the skull resulting in the loss of cerebrospinal fluid which fills the cerebral ventricles *in vivo*. Depending on the protocol, the brain can also be fixed and dehydrated at this stage. These steps produce a global shrinkage of the brain. Then, sectioning causes the brain to lose its 3D structure. Finally, sections may be sheared and shrunk during histological staining and during mounting. Global shrinkage due to brain extraction can hardly be estimated without *in vivo* imaging. Here we will consider the registration problem that is, given several histological staining series and a block-face photography series, how to recover the *post mortem* 3D brain structure for each modality. In this section, we will describe a protocol that attempts to compensate section deformations and to recover the brain 3D structure. **This protocol is mostly based on previous developments made in the laboratory for 3D autoradiography imaging [65, 69, 57, 67]** and was extended here for multiple histological staining series reconstruction and scaled-up to large-scale animal studies.

Our approach strongly relies on the use of block-face photographs as a geometrical reference. As block-face photographs are taken prior to sectioning at the same position section after section, a simple stack of block-face photographs naturally respects the original *post mortem* shape of the brain and can be used as a 3D reference for histology modalities. After stacking the 2D block-face photographs, the

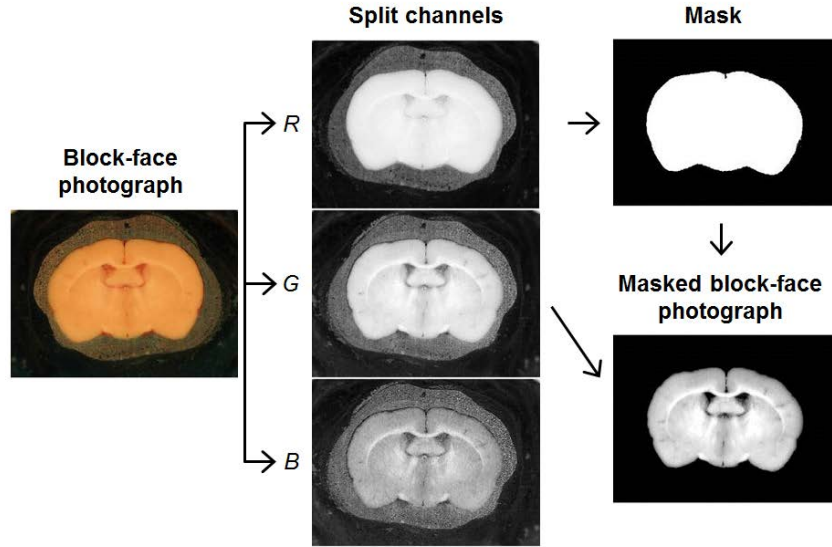


Figure 2.7: Block-face photographs image processing steps to extract the brain from the background.

resulting volumes are automatically segmented and masked so that voxels which do not belong to the brain tissue are all assigned a value of 0. Masking the block-face photography volume significantly improves further registration steps because brain tissue contours are clearly defined [57]. Thanks to the blue-colored embedding medium, there is a sharp contrast between the photographed brain tissue and the background in the R channel of the block-face photography volume. Also the G channels usually shows the best dynamic range inside the brain tissue. Therefore, the brain tissue is segmented by, first, extracting the R channel from the RGB block-face photography volume and then by applying a threshold corresponding to 40% of the upper intensity values. The resulting binary image is used to mask the G channel of the block-face photography volume (Figure 2.7).

Sections are automatically extracted from histological whole-slide images and sorted from the most rostral to the most caudal position using a protocol described in Dubois *et al.* [69]. Briefly, a binary mask is generated for each whole-slide image using an intensity threshold, connected components that do not meet a minimum size criterion are excluded and the remaining connected components are then sorted using their mass center positions. Section images are stacked to provide one non-geometrically coherent volume per histological series. Once the reference block-face photography volume has been generated, the strategy to reconstruct coherent 3D histological volumes consists in registering each histological section image to its cor-

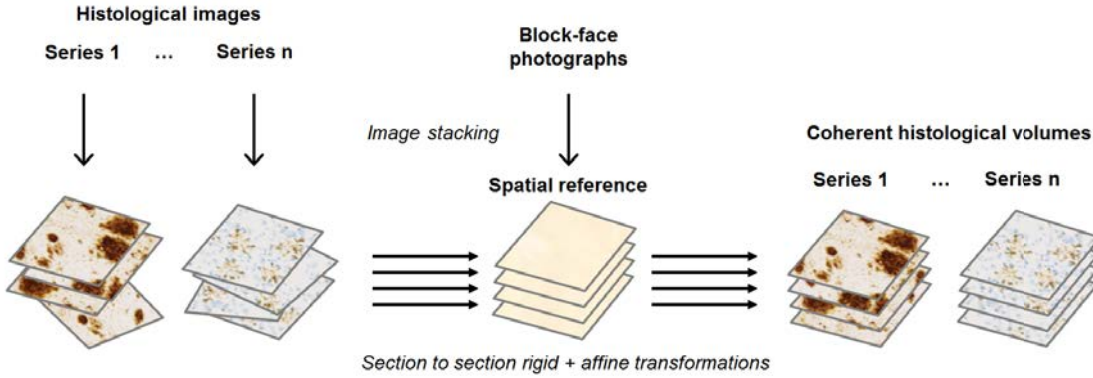


Figure 2.8: Multiple series section-to-section registration.

responding block-face photograph or, if no block-face photograph is available for this section, to its most spatially related block-face photograph (Figure 2.8). Registration between an histology image and its block-face photograph is an optimization problem where we need to find transformation parameters values that either maximize or minimize an objective function. The number of free parameters depends on the type of transformation:

- A 2D **rigid transformation** consists in 1 rotation parameter and 2 translation parameters,
- A 2D **affine transformation** consists in 1 rotation parameter, 2 translation parameters, 1 scaling parameter and 1 shearing parameter.

In practice, to estimate transformations, we first extract the most contrasted channel from the *RGB* histology volumes (this varies depending on the staining of interest). Then, for each section image, we successively estimate a rigid transformation and then use this transformation to initialize an affine transformation estimation. The rigid transformation between each histological section image I_{hist} and the its corresponding block-face photograph I_{photo} , is estimated as follows:

$$\hat{T}_r = \arg \max_{T_r \in \mathcal{T}_r} Cor(I_{photo}, I_{hist} \circ T_r), \quad (2.1)$$

where \hat{T}_r is the estimated optimal transformation within a set of \mathcal{T}_r possible rigid transformations and $Cor(., .)$, is the correlation coefficient between the intensity values of the block-face photography image and the intensity values of the transformed histology section image.

The rigid transformation is applied to the histological section image and the block-matching method is then used to estimate the affine transformation in two

steps [64, 65]. In the first step, blocks are defined on both images. The Pearson’s correlation coefficient is then computed for each pair of between-image blocks to find a list of best matches and a deformation field is generated using vectors linking the best matching blocks. In the second step, the affine transformation \hat{T}_a is estimated by minimizing the squared loss:

$$\hat{T}_a = \arg \min_{T_a \in \mathcal{T}_a} \sum_i \|y_i - T_a(x_i)\|^2, \quad (2.2)$$

where x_i and y_i are the positions of best matching blocks.

This two-step protocol allows to correct for deformations due to histological procedures and provides coherent histological volumes. Figure 2.9 shows the reconstructed block-face photographic volume and corresponding histology volumes for one mouse brain. While this protocol works for the majority of cases, it may fail to correct for non-linear deformations that can occur during histology processing or when a part of the tissue section is missing. In such cases, we replace the faulty tissue section image by its most geometrically resembling neighbor. In practice, when using automated staining devices, tissue sections are only rarely damaged so that section replacement is occasional.

2.4 Supervised segmentation of neuropathological markers

Neuropathological markers are extensively studied in human brain samples and animal models of Alzheimer’s disease and they represent important therapeutic targets. Thus, their precise quantification is a critical issue for both physiopathological research and drug development. Quantification is commonly performed by segmenting histology whole slide microscopy images and computing the proportion of positively stained pixels relative to the remaining brain tissue.

In this context, global and adaptive thresholding are popular segmentation approaches for they are simple and fully automated (see section 1.1.3). However these methods are prone to errors. Indeed, histological procedures often lead to the presence of artifacts, such as debris and tissue folding, which have similar color properties to the marker of interest. In addition, histological staining can lead to important background nonspecific staining. This hinders methods based solely on color to provide optimal segmentation results and, as neuropathological markers represent a tiny portion of the brain tissue, minor segmentation errors can strongly impact the

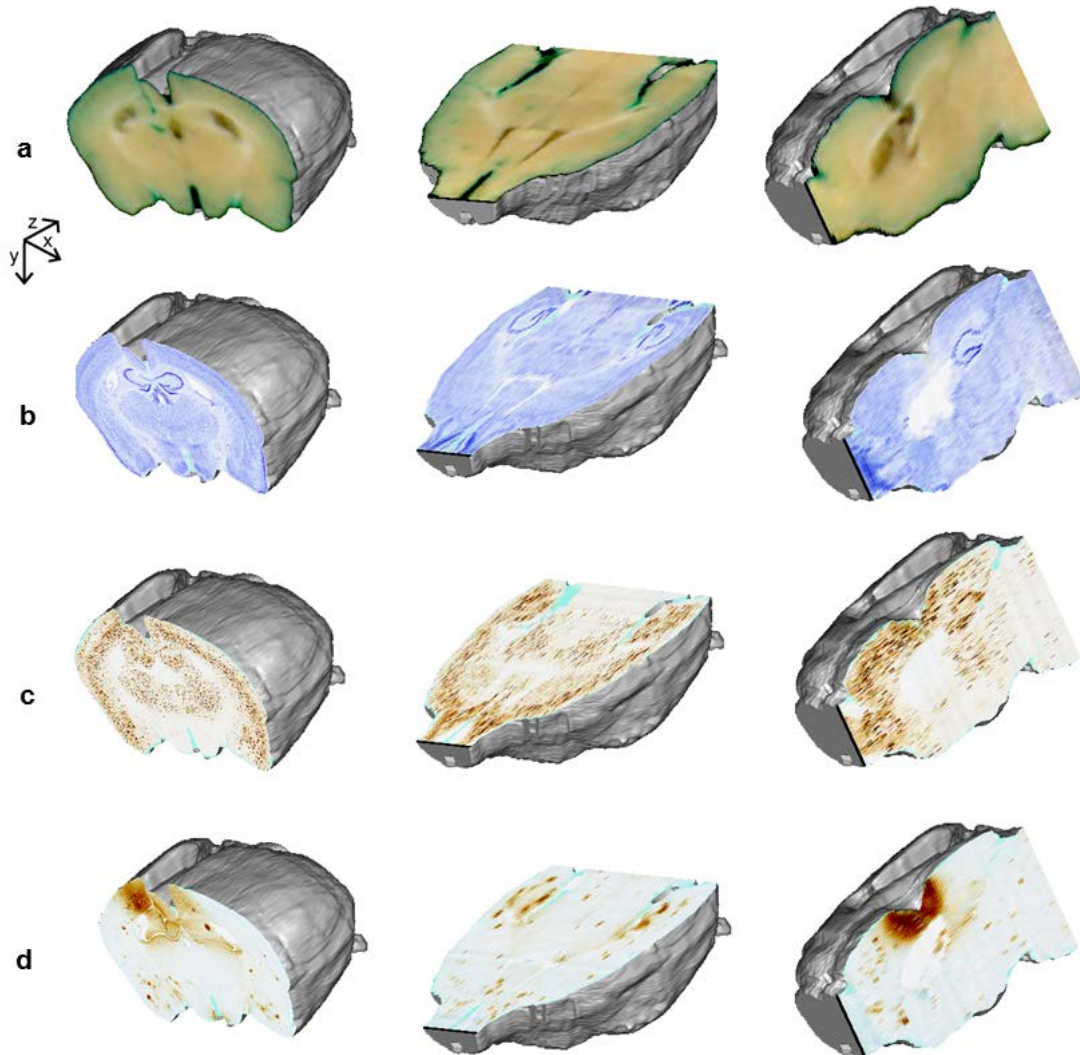


Figure 2.9: 3D multimodal reconstruction for one APP/PS1 mouse brain in coronal (left), axial (middle) and sagittal (right) cutting planes. (a) Block-face photography volume, (b) Nissl-stained histology volume, (c) AP histology volume (6E10 IHC staining), (d) blood-brain-barrier leakage histology volume (anti-IgG IHC staining).

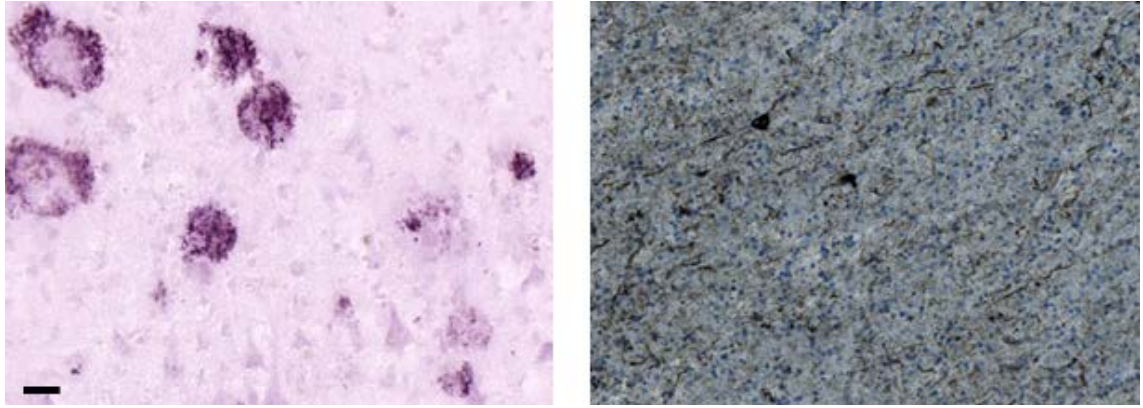


Figure 2.10: Immunohistochemistry of a brain sample from a patient with Alzheimer’s disease. Left: $A\beta$ plaques appear as dark purple clusters. Right: neurofibrillary tangles appear in black over a blue Nissl counterstaining. Scale bar: 20 μm .

overall quantification.

To overcome these limitations, Chubb *et al.* [26] proposed **BioVision**, a supervised classification approach which uses color and local intensity information (mean of the R , G and B channels in a 16-pixels diagonal neighborhood, section 1.1.3). This latter feature is particularly helpful to account for noise in neuropathology images. For each class, BioVision estimates the joint distribution of the predictors using Gaussian Mixture Models. In the segmentation step, each pixel is classified with a Bayesian classifier. Class imbalance between neuropathological markers and the rest of the tissue can be accounted for by injecting prior probabilities of each class in the decision. Although numerous contextual features have been shown to be efficient for image segmentation, they are typically high-dimensional and because of the curse of dimensionality, density estimation for these features with GMM is hazardous. Thus, one limitation of BioVision is that it cannot adequately incorporate complex contextual features, such as texture descriptors, which could be beneficial to the classification task. The authors proposed to use an automatic post-processing step to remove incorrectly classified pixels based on shape and size features. However, pathological aggregates are not well-defined objects. As shown in Figure 2.10, they present irregular shapes and disparate sizes. Hence, misclassified pixels are hard to detect with morphological features and a robust one-step segmentation approach would be preferable.

In the next subsections, we describe a supervised classification approach that incorporates color and texture features in order to better discriminate markers of

interest from noise. We propose to use **Weighted Random Forest (WRF) for robust classification and parallel computing to handle large whole slide images**. We show that this approach is more robust to artifacts and background signal than BioVision. Furthermore, the proposed approach was applied to analyze images from both human and mouse brain tissue samples and we show its usability on a large scale by segmenting a mouse high-resolution 3D whole-brain histology dataset.

Datasets

The first two datasets were used as benchmarks for $A\beta$ plaque and neurofibrillary tangle detection. A cortical brain tissue sample (GIE NeuroCEB brain bank) from a patient with confirmed diagnosis of Alzheimer’s disease was sectioned. Ten tissue sections were stained for $A\beta$ plaque detection (4G8 IHC). Two sections were stained for neurofibrillary tangle detection (AT8 IHC with a Nissl counterstaining) (Figure 2.10). All sections were digitized using Zeiss Axio ScanZ.1 whole-slide imaging microscope at a resolution of $0.44\ \mu\text{m}$. At this resolution, each image has a size of approximately 15000×15000 pixels. Fifty representative image patches (200×200 pixels) for each staining were then extracted from whole-slide images and each patch was manually segmented into 3 classes: marker of interest, tissue and glass slide background. The patches were extracted so as to represent the variety of patterns present in the whole-slide images and manually segmented using *Anatomist* software. For each staining, patches were split so that half of them were used for learning and model selection and the other half was kept for final validation and comparison between algorithms.

The third dataset is a 3D reconstruction of the whole brain of an APP/PS1 mouse model of Alzheimer’s disease. To generate the whole brain histology volume, a set of 78 sections were stained for $A\beta$ plaque detection (6E10 IHC), sections were digitized at a resolution of $0.44\ \mu\text{m}$ and the 2D images were reconstructed in 3D with an inter-section distance of $125\ \mu\text{m}$ using the protocol described previously with some adaptations to account for the large size of the images (section 5.2.1). The 3D histology dataset has a size of about 100GB.

Feature extraction

Our approach includes color, local intensity and texture features. For color features, *HSV* (for Hue, Saturation and Value) color space was chosen over *RGB*. While the *RGB* color space is convenient for image display, each channel

is correlated with light intensity (see section 1.1.2). This means that for the same perceived color, if intensity changes, R , G and B values will vary together. Thus, it can be misleading to evaluate color dissimilarity based on a distance measure in the RGB space. The HSV color space has been developed in an attempt to better adhere to the human perception. It can be represented as a cylinder with Hue being the angle around the central axis and representing the tint; Saturation being the distance from the center and representing the purity (that is how much white that is added to the color) and Value being the height and representing the brightness.

Similarly to BioVision, local intensity was computed for each pixel as the mean of the grey-scale converted intensity values within a disk-shaped neighborhood of a given radius.

Images were convolved with a family of **Gabor filters** to extract texture information. Gabor filtering is among the most popular approach for texture classification and it has been shown to model the function of simple cells in the mammalian visual system [70]. The 2D Gabor filter kernel consists of a sinusoidal wave multiplied by a Gaussian function and it has a real and an imaginary component:

$$g(x; y; \lambda; \theta; \psi; \sigma; \gamma) = \exp\left(-\frac{x'^2 + \gamma^2 y'^2}{2\sigma^2}\right) \cos\left(2\pi \frac{x'}{\lambda} + \psi\right) \text{ (real part)} \quad (2.3)$$

$$g(x; y; \lambda; \theta; \psi; \sigma; \gamma) = \exp\left(-\frac{x'^2 + \gamma^2 y'^2}{2\sigma^2}\right) \sin\left(2\pi \frac{x'}{\lambda} + \psi\right) \text{ (imaginary part)} \quad (2.4)$$

where x and y are 2D coordinates, $x' = x \cos \theta + y \sin \theta$, $y' = -x \sin \theta + y \cos \theta$, λ is the wavelength of the sinusoidal wave, θ is the orientation, ψ is the phase offset, σ is the Gaussian envelope standard deviation and γ is the Gaussian envelope aspect ratio. The domain of the Gabor function is infinite and filtering would theoretically require an infinite window size. Here, we truncated the filter window to a size of 4σ when γ is 1 (*i.e.* if the Gaussian function is symmetric relative to its mean). This was chosen because, for a two-tailed normal distribution, we know that the interval spanning 4 standard deviations around the mean will contain 95% of the area under the curve. If $\gamma \neq 1$ then the window size in x and y directions can be calculated as:

$$sx = \max(|4\sigma \cos \theta|, |4\frac{\sigma}{\gamma} \sin \theta|), \quad (2.5)$$

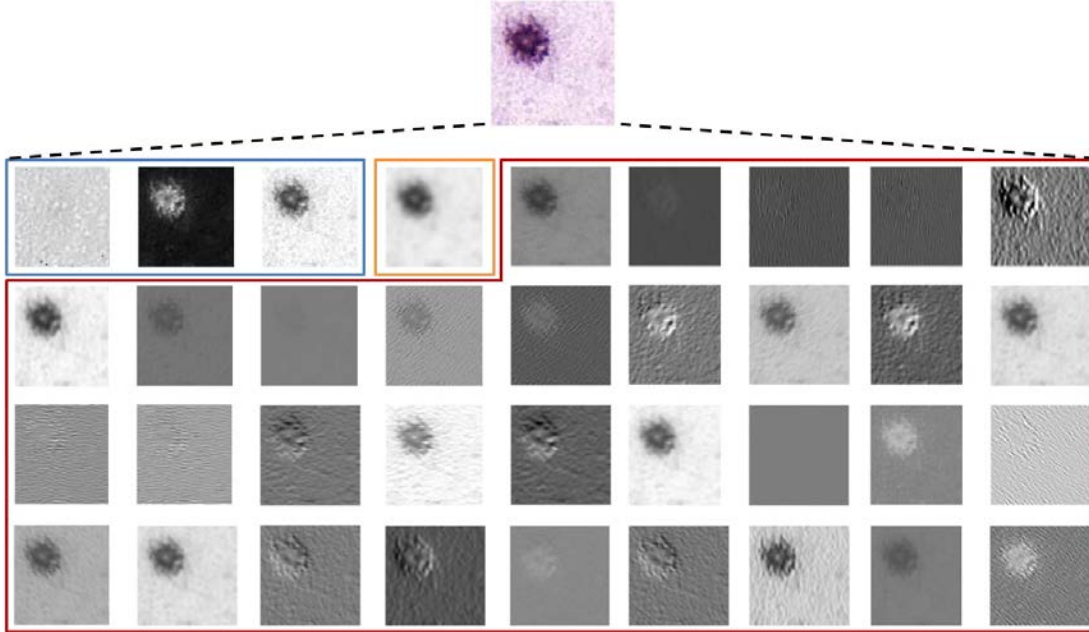


Figure 2.11: Feature extraction. A small patch with an AP in purple (top) is processed to extract features: HSV channels (blue), local intensity (orange) and Gabor filter responses (red).

$$sy = \max(|4\sigma \sin \theta|, |4\frac{\sigma}{\gamma} \cos \theta|). \quad (2.6)$$

Here, we used a family of filters with 4 orientations and 4 wavelengths [71]. σ and γ values were tuned by cross-validation as will be explained on page 45 and ψ was held constant at 0. This led to a 36-dimensional feature vector for each pixel (Figure 2.11).

Weighted Random Forest

Random Forest (RF) is an ensemble of fully grown classification decision trees [72]. A classification decision tree is a set of hierarchically organized binary splitting rules that segments the features space. During tree growing, the feature space is partitioned at each node to minimize the cross-entropy, defined by:

$$H = - \sum_{j=1}^m p_j \log(p_j), \quad (2.7)$$

where p_j is the proportion of pixels of class j at a given node. The tree is fully grown when each region of the feature space contains observations only from one

class. Single trees are, however, usually not very accurate when predicting the class of new observations. This is mostly because decision trees over-fit the learning data and, therefore, cannot adequately generalize to new observations.

In RF, each classification tree is built using a bootstrap sample of the original learning set and only a subset of randomly selected features at each node of the tree. This allows RF to have a low variance compared to a single decision tree and eventually, a better performance. RF can fit highly nonlinear decision boundaries which makes it particularly useful to discriminate the markers of interest from artifacts. Besides, classification performance is not very sensitive to RF algorithm parameters (number of trees and number of randomly selected features at each split). Thus, parameters can be chosen using rules of thumb rather than by using cross-validation which is computationally advantageous. Several open-source implementations for classification decision trees and RF exist. Here, we used the *scikit-learn* python implementation (<http://scikit-learn.org/>) [73] .

One limitation of decision tree learning algorithms is that when the classification problem is highly imbalanced, they tend to be biased toward the majority class. To overcome this problem, we propose to use a weighted form of RF modified from Chen *et al.* [74]. Each class is assigned a weight ω_j . At a given node, we have a population of pixels x_i with $i = 1..n$, $Y \in \mathbb{R}^n$ their corresponding class labels, a vector of weights $W \in \mathbb{R}^n$ such that $W_i = \omega_{Y_i}$ and a matrix of indicator variables $M \in \mathbb{R}^{n \times m}$ such that $M_{j,i} = 1$ if x_i is of class j and 0 otherwise.

In equation 2.7, p_j is calculated as a weighted proportion:

$$p_j = \frac{M_j W}{\sum_{i=1}^n W_i}. \quad (2.8)$$

If class weights are equal, this is equivalent to the classical RF. If the minority class is given a higher weight than other classes, this results in an increase of its influence in the tree building process. After growing an ensemble of B trees $\{T_b\}_1^B$, class prediction for any new pixel x is done by weighted majority voting:

$$\hat{Y} = \arg \max_{j \in [1-m]} \omega_j \sum_{b=1}^B I(T_b(x) = j), \quad (2.9)$$

where $I(\cdot)$ is the indicator function. For a good trade-off between performance and computational burden, we chose $B = 100$ trees to build the ensemble models.

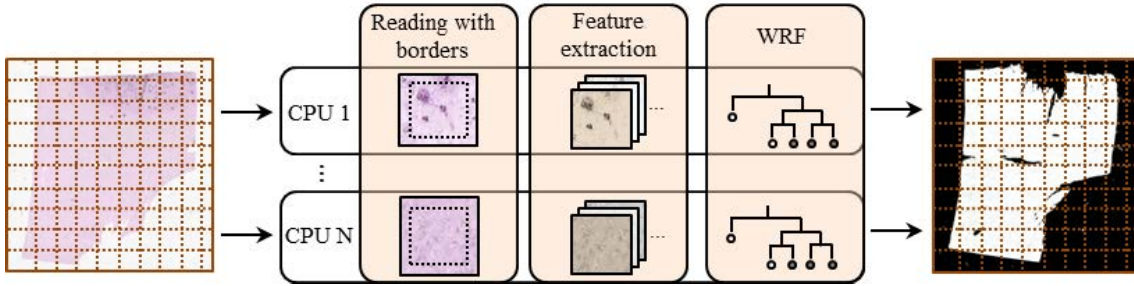


Figure 2.12: Parallel processing of a whole slide microscopy image.

High-performance computing for whole-slide images analysis

Because lots of features are extracted for each pixel, segmenting large whole-slide images using this approach is computationally intensive. When processing *RGB* pixels encoded in 24 bits, 36 features are computed and encoded as 32-bits floating point values. This results in generating data 48 times bigger than the original *RGB* image.

Features extraction was implemented in C++ to ensure reasonable computation time. Besides, we took advantage of recent developments in our laboratory enabling partial input/output access. This allows to read small chunks within big whole-slide images, process them and write the result at the right position inside a big output image without loading whole images into memory [75]. As feature extraction can be particularly time and memory consuming, large images are divided in small chunks that are processed in parallel (Figure 2.12). In order to take into account chunk borders properly during feature extraction, each chunk is processed with additional width equal to the size of the largest convolution kernel. This ensures that the global segmentation will be strictly the same whatever the number of jobs and image size. Also, to minimize memory usage during feature extraction, each feature is sequentially computed, saved in the output file and deleted from memory before processing to the next feature. Finally WRF classification is applied to each chunk in parallel.

Model selection via leave-one-image-out cross-validation

We investigated the effect of feature extraction and learning parameters on classification performance with a full factorial design. We hypothesized that the local intensity neighborhood radius could have an impact on classification. Furthermore, according to Bianconi *et al.* [76], who evaluated the effect of the Gabor filter parameters on texture classification, we considered the effects of the standard deviation of

the Gaussian envelope and its spatial aspect ratio. Finally, we considered the effect of increasing the weight of the minority class in the WRF (while the weights of tissue and background classes were kept equal to each other). A factorial design with three levels per parameter was constructed, leading to a total of 81 combinations (Table 2.1).

Table 2.1: Levels of the factorial design.

Parameter	Values
Local intensity radius	4, 8, 16 (pixels)
Gaussian envelope standard deviation (σ)	1, 2, 3 (pixels)
Gaussian envelope aspect ratio (γ)	0.5, 1, 1.5
Minority class weight	1.0, 1.25, 1.5

As RF relies on bootstrapping the original data, it is tempting to evaluate model performance by computing an out-of-the bag estimate for each model. However, unlike cross-validation, out-of-the bag estimation is valid if the observations used for estimating classification performance are independent of those used for constructing the model. In our case, neighboring pixels are correlated, hampering pixel-level resampling to provide independent samples. In contrast, the 25 patches in the training set are nearly independent since they are not neighboring and were sampled from various tissue sections. We used these patches as blocks for cross-validation as follows. Let $Z = (X, Y)$ be the learning set with X the feature vectors for all pixels and Y their corresponding class labels. For each image $i = 1, \dots, k$ included in the learning set, let $Z_i \subset Z$ be its subset in the learning set and let $Z_i^c \setminus Z$ its complement. A model $Q(Z_i^c)$ is constructed for each i and used to make predictions \hat{Y}_i over X_i . This leads to a leave-one-image-out cross-validation scheme. Precision and recall were calculated for each class j as, respectively, $P(Y = j \mid \hat{Y} = j)$ and $P(\hat{Y} = j \mid Y = j)$. A mean cross-validation f1 score was calculated for each parameters combination t as:

$$\bar{f1}(t) = \frac{1}{n} \sum_{j=1}^n 2 \frac{Precision_{t,j} \times Recall_{t,j}}{Precision_{t,j} + Recall_{t,j}} \quad (2.10)$$

Using $\bar{f1}$ ensures that all classes are equally important. Finally, the optimal combination corresponding to $\arg \max \bar{f1}(t)$ was chosen to construct the final model using the whole learning set. The final model was compared to our implementation of the BioVision algorithm using test set images.

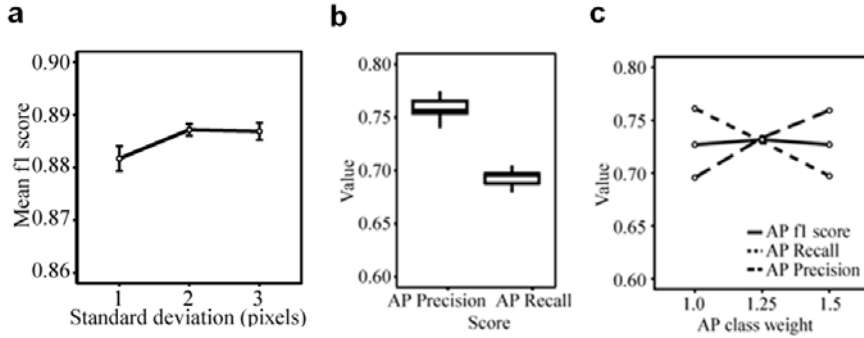


Figure 2.13: (a) Effect of Gaussian envelope standard deviation on $\bar{f}1$ score. (b) Systematic imbalance between precision and recall for $A\beta$ plaque classification with Random Forest. (c) Effect of adjusting $A\beta$ plaque class weight.

Segmentation results and comparison with BioVision

Leave-one-image-out cross-validation scores for the $A\beta$ plaque and neurofibrillary tangle datasets remained relatively stable ($\bar{f}1$ between 0.87 and 0.90 for the $A\beta$ dataset and between 0.89 and 0.90 for the neurofibrillary tangle dataset) using the previously defined parameter levels. Similarly to Bianconi *et al.* [76], the smoothing parameter of the Gabor filter had a significant influence on classification (Figure 2.13a). As shown in Figure 2.13b, there was a systematic bias between precision and recall when class weights are equal (*i.e.* for RF). Figure 2.13c, shows how this shift could be compensated by adjusting the minority class weight. Recall increased with weight which led to an inevitable decrease of precision. Over-weighting the minority class provided little improvement of the $\bar{f}1$ score but the equilibrium between precision and recall is valuable to ensure that the overall quantification is unbiased.

Table 2.2 shows the comparison of the proposed approach with BioVision in term of classification performance on the 25 test images for the two datasets. Both methods appropriately classified tissue and glass slide background. Our approach showed the best score for every class in both datasets. While both methods achieved good $A\beta$ plaque (Figure 2.14a) and neurofibrillary tangle segmentation (Figure 2.14b), the proposed approach was clearly more robust than BioVision in the presence of high background noise (Fig. 2.14c) and artifacts (Fig. 2.14d).

The 3D whole brain dataset and its associated segmentation are shown in Figure 2.14e,f. Using parallel computing on a 16-core workstation, we were able to extract features and segment the whole slide image (24000×16000 pixels) of a mouse brain section in 25 minutes. Computing time speed-up was nearly linear with the

Table 2.2: f1 scores for A β plaques (AP), neurofibrillary tangles (NFT), tissue (Ts), background (Bk) and mean f1 score (Mn) for the two benchmark datasets.

Methods	AP dataset f1 scores				NFT dataset f1 scores			
	AP	Ts	Bk	Mn	NFT	Ts	Bk	Mn
BioVision	0.68	0.96	0.95	0.87	0.49	0.95	0.97	0.80
Proposed approach	0.76	0.98	0.96	0.90	0.56	0.96	0.98	0.83

number of CPUs which indicates that segmentation time for large images can be significantly decreased using computer clusters. In comparison, BioVision had a shorter computing time (7 min).

The proposed approach performs accurate and scalable segmentation of whole neuropathology tissue section images from both human and mouse brain samples. This one-step classification approach limits the need for automatic or heavy manual post-processing to remove incorrectly classified pixels. However, it should be noted that, in order to get a robust model, the learning set has to be as much representative as possible of the different structures in the neuropathology images including noise and artifacts. A remaining question is, how much data should be included in the learning set. Manually annotating images is time consuming and it would be interesting to explore how many patches should be annotated in order to get a good model. It can be expected however, that the optimal number of patches to include in the learning set will vary with different markers and staining protocols. Future work could also be undertaken to compare classification performance and computing time using different color features (*RGB*, *HSV*, *Lab*) and various contextual descriptors, such as Gabor features variants [77] and co-occurrence matrices [78]. Besides, dimensionality reduction methods could be applied in order to reduce computational burden due to file size when dealing with very large microscopy datasets. Indeed, because whole-slide images are typically very large, one limitation of the proposed approach is the computation time that it requires. In this respect, BioVision is more competitive but fast computation comes at a cost in term of accuracy. In conclusion, both approaches can be successfully applied and the choice between them should be driven by the image complexity. **If signal-to-noise ratio is high, BioVision will provide good results in a short time. On the other hand, if the amount of noise is significant (artifacts, background non-specific staining...), the proposed approach will be more accurate and will limit the need for manual post-processing to obtain proper results.** In chapter 4, when segmentation will be performed on a large-scale in group studies, both

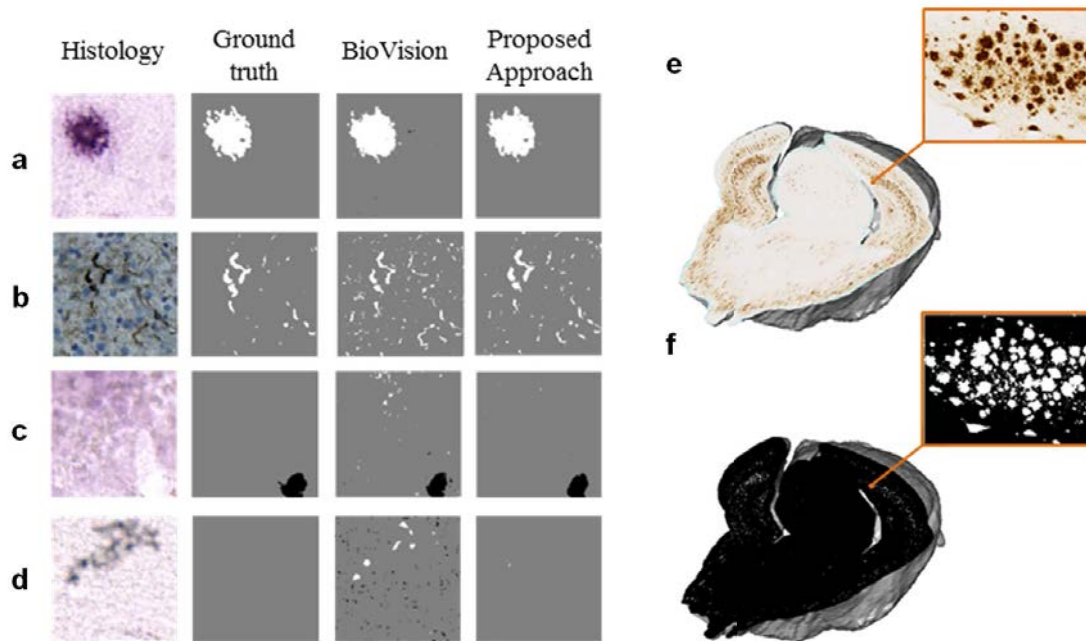


Figure 2.14: Segmentation results. (a-d) Comparisons of BioVision and our approach on test set images for $A\beta$ plaque and neurofibrillary tangle detection: $A\beta$ plaque and neurofibrillary tangle classes appear in white, tissue class in gray and background class in black. (e) 3D reconstruction of a mouse brain with $A\beta$ plaques appearing in brown and (f) the corresponding segmentation.

methods will be used depending on the image complexity.

Chapter 3

Brain-wide quantitative analysis of neuropathological markers

Increasingly, biomedical researchers look for methods that can provide them with a system-level understanding of biological phenomena. *In vivo* neuroimaging modalities allow to study the human brain anatomy and function as a whole. Thus, a number of analysis methods have been developed to analyze clinical datasets at the whole-brain level. The 2 main approaches that have been proposed to analyze neuroimaging datasets are **atlas-based** or **voxel-based**. The first one allows to study imaging biomarkers in anatomical regions of interests that can be automatically identified using digital atlases. In contrast, the voxel-wise approach allows to study imaging biomarkers without any anatomical *a priori*. To our knowledge, the extension of these methods to the quantitative analysis of brain histopathological markers has not been made yet. This chapter will describe the **adaptation of the atlas-based and voxel-based analysis to extract meaningful biological information from 3D histopathology studies**. The first section will focus on the **ontology-based** analysis which is a natural extension of the atlas-based method and the second section will describe the adaption of **voxel-wise analysis** to histopathological data.

3.1 Ontology-based analysis

3.1.1 3D mouse brain atlases

A benefit of using 3D whole-brain imaging compared to 2D histopathology imaging is that one can register 3D digital brain atlases to the studied individuals in order

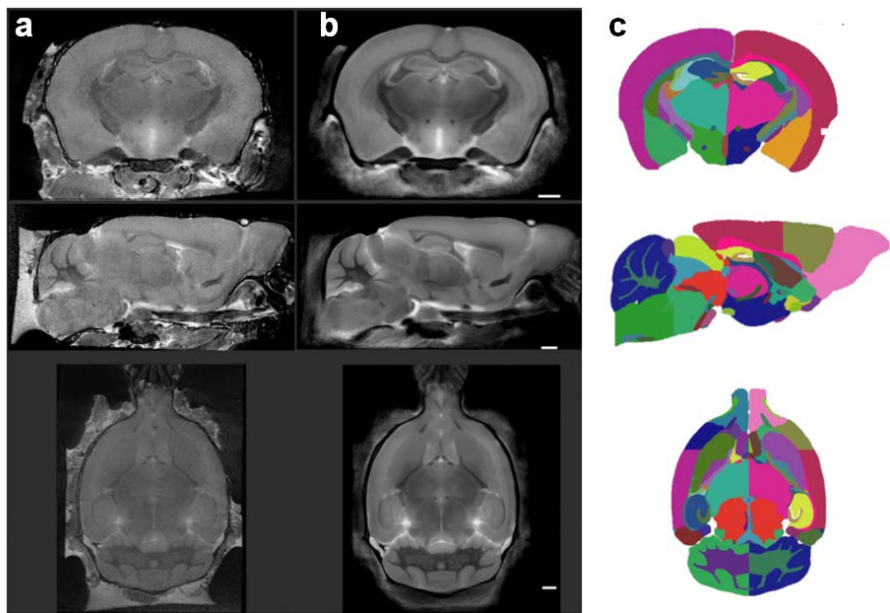


Figure 3.1: Mouse brain digital atlas from Dorr *et al.* [79]. (a) MRI scan from a single mouse brain. (b) Averaged MRI scan from 40 individuals (scale bar: 1 mm). (c) Atlas label image: each color corresponds to a particular anatomical region. From top to bottom: coronal, sagittal and axial views.

to automatically delineate regions of interest. A **digital brain atlas** consists of 2 images:

- An **anatomical volume** which provides good contrasts between brain structures, typically an MRI scan. Sometimes several imaging protocols are performed on the same subject to generate a multi-modal anatomical image.
- A **label volume** which indicates the anatomical region membership of each voxel within the brain of the anatomical image.

Constructing brain atlases is a labor-intensive process since regions of interests are manually delineated on the anatomical image. Fortunately, several groups have made their atlases publicly available for research purpose. Notably, the *Center for In Vivo Microscopy* at *Duke University* (www.civm.duhs.duke.edu) in North-Carolina and the *Mouse Imaging Centre* in Toronto (www.mouseimaging.ca) have released a number of atlases on their website over the past few years.

Mouse digital brain atlases are numerous and very diverse. During this work, we chose to use an atlas from the Mouse Imaging Centre which was published by Dorr *et al* [79] (Figure 3.1). This atlas partitions the adult mouse brain (C57BI/6J

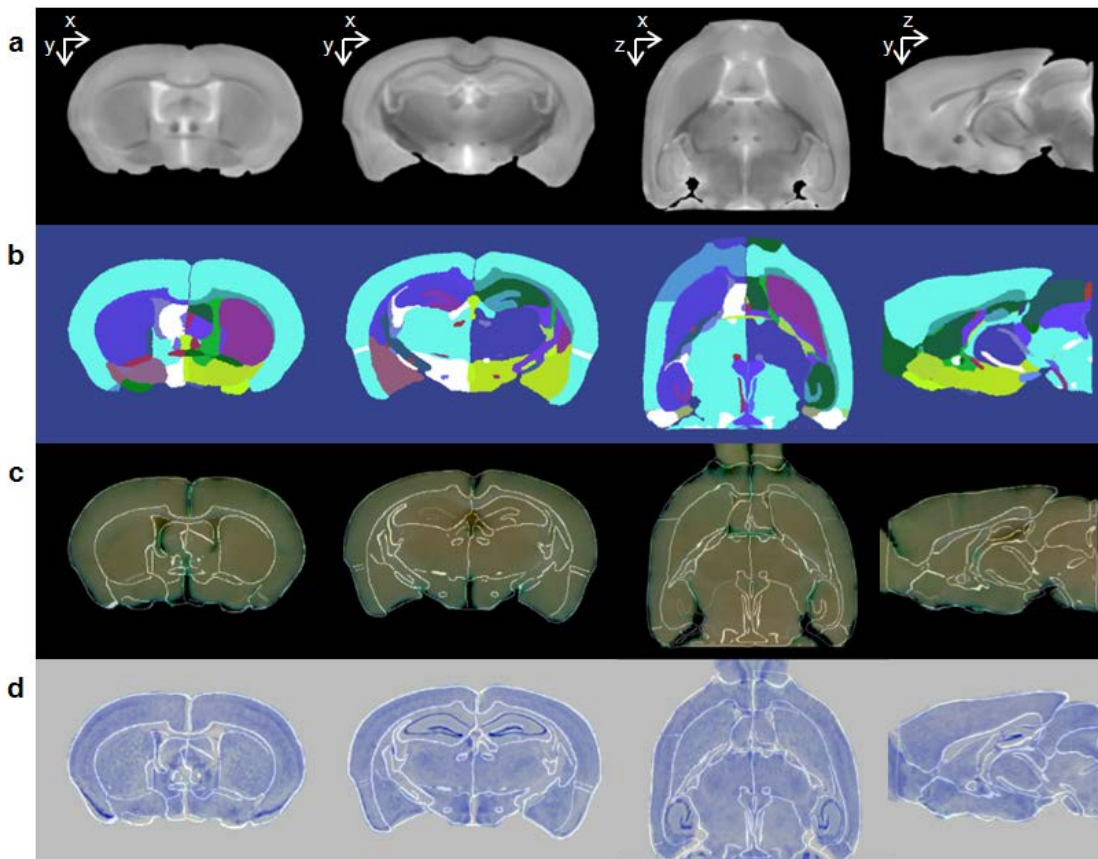


Figure 3.2: Mouse brain digital atlas registration with 3D histopathology. (a) Atlas MRI and (b) Atlas labels from Dorr et al. [79]. (c) Registered atlas label contours superimposed with block-face photographic volume. (d) Registered atlas label contours superimposed on the corresponding Nissl-stained reconstructed volume.

strain) into 62 regions of interest. The anatomical image has been constructed by registering 40 mouse brain MRI scans into a common reference and by averaging the registered images. This allowed the anatomical image to be representative of the C57BI/6J mouse brain anatomy and to have a high signal-to-noise ratio (Figure 3.1b). This atlas was chosen for the quality of the anatomical image and as well as the precision of regions segmentation.

3.1.2 Atlas registration to histopathological data

The essential step to perform atlas-based analysis is to match the atlas labels with the images to analyze. As seen in the previous chapter (section 2.3), for one individual, all the histopathological volumes are matched to the block-face photography volume. Hence, if the atlas label image is correctly registered to the block-face pho-

tography volume, it will be possible to use it to delineate regions of interest for each histopathological volume of this individual. Registration of the atlas image on the block-face photography volume involves to, first, estimate transformations between the atlas anatomical image and the block-face photography image and then, to apply these transformations to the atlas label image.

The protocol that was used to estimate transformations between the atlas anatomical image and the block-face photography volume has been largely described and validated by Leberberg *et al.* [67]. Briefly, a global rigid transformation (rotation, translation) is estimated based on mutual information similarity criterion optimization [80]. Then, an affine registration initialized with the rigid transformation is performed with the Block-Matching technique [64]. To improve registration locally, we used an elastic transformation, based on **Free-Form Deformation (FFD)** using mutual information as the optimization criterion and a grid of $10 \times 10 \times 10$ regularly spaced control points [81, 82]. Figure 3.2 shows an example of a registration between the atlas and 3D histopathological data.

3.1.3 Mouse brain ontology

The registered atlas labels enable to perform global regional measures of the ratio occupied by the histopathological marker of interest compared to the volume of the region. Nonetheless, relevant regions may vary according to each study and with each marker and, sometimes, the atlas may not include a particular region of interest. Also, Leberberg *et al.* [67] have shown that the registration between the atlas and block-face photography is usually of good quality for rather large regions but, due to small errors, it does not suffice to precisely match small regions. Thus, in most cases, many small regions of the atlas may not be relevant to study and it could be more sensible to fusion them into bigger structures.

A **brain ontology** adapted from the NeuroNames ontology [83] was constructed in order to allow the aggregation of regions at different anatomical levels of the brain (Figure 3.3). This virtually increased the number of regions in the atlas and it allows to compute results at multiple levels of anatomical detail.

CHAPTER 3: BRAIN-WIDE QUANTITATIVE ANALYSIS OF NEUROPATHOLOGICAL MARKERS

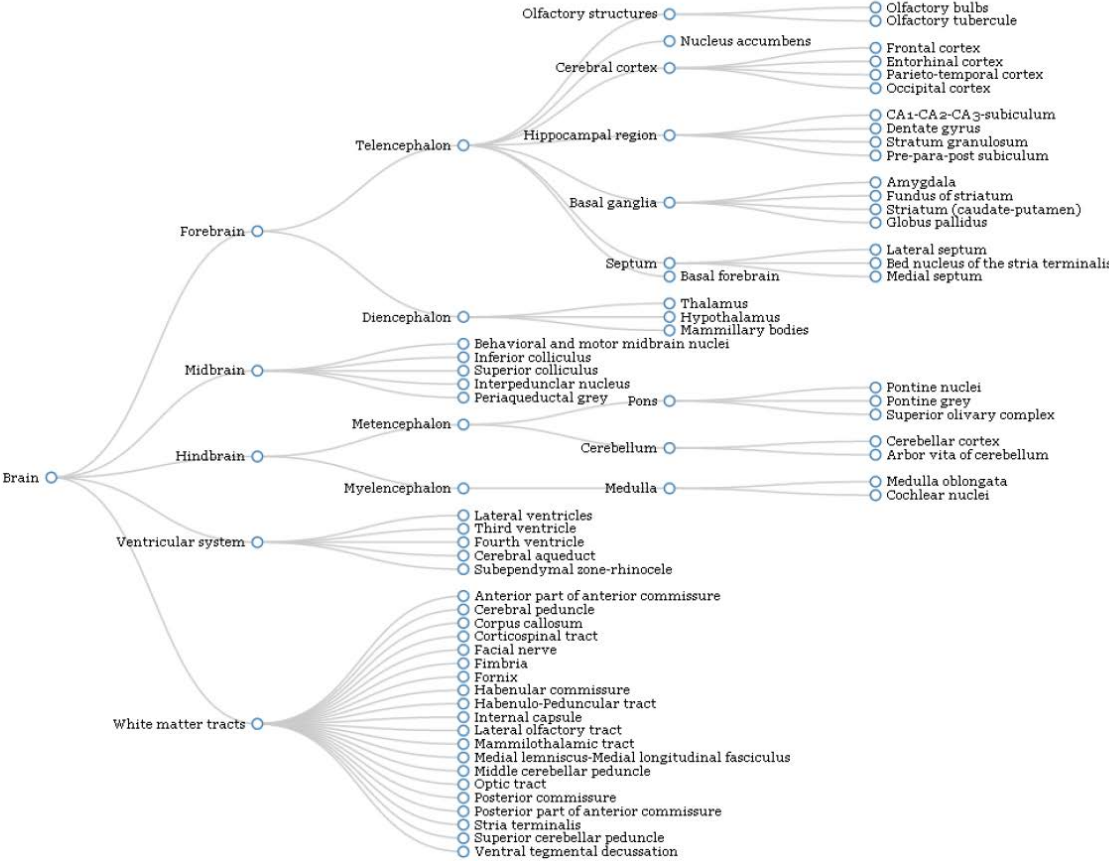


Figure 3.3: Mouse brain ontology. Most elementary structures correspond to the mouse brain atlas labels. The brain ontology was adapted from the NeuroNames ontology (<http://braininfo.rprc.washington.edu>) to match the original MICE atlas labels.

3.2 Voxel-wise analysis

3.2.1 Principle and issues for histopathological data analysis

Ontology-based analysis allows to explore much more regions than it would be possible with manually defined ROIs. Voxel-wise analysis pushes exploratory analysis even further by enabling to infer differences between groups at the voxel-level. This allows to detect effects that cannot be easily characterized by regions of interest such as very local effects or diverging effects within close proximity.

Voxel-wise analysis has been developed in the early 1990s to detect local differences between PET scans [86]. Since then, voxel-wise analysis has been successfully and broadly applied for the analysis of functional imaging (PET, fMRI). Besides, its use has been extended to a vast range of applications such as brain structure analysis via *Deformation-based morphometry* or *Voxel-based morphometry* and small-animal imaging analysis [87]. In our group, voxel-wise analysis has been previously employed to analyze 3D autoradiography data and allowed to finely characterize the alterations of brain glucose metabolism in mouse models of Alzheimer’s disease and Huntington’s disease [84, 85] (Figure 3.4). The use of voxel-wise analysis has been largely promoted by *Statistical Parametric Mapping* (SPM), a software package that includes an extensive set of tools for voxel-wise analysis. In order to perform voxel-wise hypothesis testing with a given set of images, each voxel should represent a **continuous** and, ideally, normally distributed parameter such as, for example with 2-deoxyglucose PET and autoradiography imaging, the local amount of glucose uptake. In addition, the parameter at study should be **spatially smooth** to ensure that the detected clusters are spatially consistent. Provided these assumptions hold, differences between groups can be inferred at the voxel-level in 2 main steps: (1) **spatial normalization** to match all the individuals to a common anatomical reference and, (2) **voxel-wise hypothesis testing** to infer the location and size of the effects. These general steps will be briefly described in the next subsections before addressing the issues of voxel-wise analysis for histopathological data.

Spatial normalization

Spatial normalization consists in registering every individual image in a common spatial reference so that voxels coordinates correspond to the same anatomical locations in all the individuals. This often involves to, first, generate an anatomical reference. Ideally, an anatomical reference should be generated from images acquired with an imaging modality providing good anatomical contrasts such as anatomical MRI or

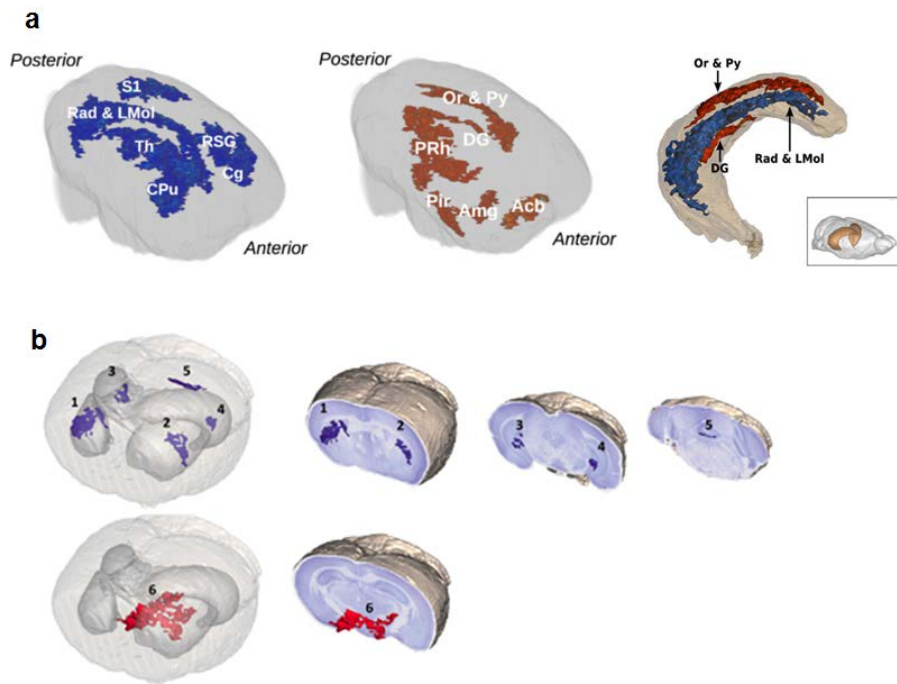


Figure 3.4: Examples of voxel-wise analysis studies of the brain glucose uptake impairment in mouse models of neurodegenerative diseases. Blue areas were identified as significantly hypo-metabolic whereas red areas were identified as significantly hyper-metabolic. (a) 3D renderings of glucose uptake impairments in APP/PS1 mice compared to wild-type mice [84]. Interestingly, in the hippocampal region (right), diverging effects were found with hypo-metabolic areas in the dentate gyrus while the stratum oriens and the pyriform layer were identified as hyper-metabolic. (b) 3D renderings of brain glucose uptake impairment in BACHD mice compared to wild-type mice [85]. Local hypo-metabolic effects were identified in the striatum (regions 1 and 2), the hippocampal region (regions 3 and 4) and the cerebellum (region 5) while hyper-metabolic effects were found in the hypothalamus (region 6).

block-face photography. The anatomical reference is generated by registering all or a subset of the anatomical images of the study onto one chosen individual and then by averaging the registered images to obtain a mean anatomical image which is referred as the **anatomical template**. Anatomical images are then registered to the anatomical template to spatially normalize all the individuals of the study. Finally, images that we wish to analyze at the voxel-level are spatially normalized by applying the previously calculated transformations between the anatomical images and the anatomical template.

SPM comes with the DARTEL registration algorithm to spatially normalize the individuals. In our case, the FFD registration algorithm was used as it was already implemented in BrainVISA.

Hypothesis testing

Once every image has been spatially normalized, hypothesis tests can be performed separately at each voxel of the brain to locally infer statistically significant differences between groups. Prior to hypothesis testing, images are smoothed with a Gaussian filter to reduce noise and intra-group variance. Typically, the tested hypothesis is that there is a difference between means of 2 or more groups. For a 2 groups study, if we can assume that the observations are drawn from normally distributed populations, the Student's t-test can be used to assess if means between groups are significantly different. A **T-statistic** is first calculated which reflects how much different are the means of the 2 groups. Under the hypothesis that there is no difference between means, the T-statistic follows a Student's distribution. The computed T-statistic is compared with this null-distribution to compute the **p-value**. The p-value of the test indicates how likely it is to obtain at least such a difference between the means when groups are drawn from the same population. If the p-value is lower than some predefined α threshold (often $\alpha = 0.05$) we can safely reject the hypothesis that the 2 groups are drawn from the same population, and hence, declare that the means are significantly different. Finally, once tests have been performed for each voxel of the brain, sets of neighboring voxels that present statistically significant differences between groups are termed **clusters**.

In SPM, hypothesis testing is carried-out with general linear models which provide a general mathematical framework for parametric inference [88]. The advantage of the general linear models formulation compared to the classical formulation of statistical tests is that it allows to account for covariates. This is particularly useful to remove the effect of possibly confounding factors when studying heterogeneous pop-

ulations (age, sex etc...) or for *in vivo* longitudinal studies. In preclinical studies, however, populations tend to be much more homogeneous and confounding factors are usually better controlled than for clinical studies. Thus, in this work, hypothesis tests were carried-out using the classical t-test rather than general linear models.

Correction for multiple comparisons

One important issue to take into account for voxel-wise studies is the correction for multiple comparisons. Indeed, as the number of statistical tests rises, the null-hypothesis cannot be safely rejected at $\alpha = 0.05$ without introducing some false positives. Brain images often consist of millions of voxels, thus, uncorrected voxel-wise tests may very likely result in a number of false positives. Common techniques to correct for multiple comparisons include the **Bonferroni** correction, the **False Discovery Rate** correction (FDR) [89] and **cluster-based inference** [90].

Bonferroni and FDR procedures both correct for multiple comparisons at the voxel-level but with different goals. With Bonferroni correction, we ensure that the risk of making one or more errors among all the tests is equal to α . Contrastingly, with the FDR procedure, we ensure that among all the tested mean differences that were deemed statistically significant, on average, a fraction equal to α are false positives. In practice, the FDR procedure is often preferred to the Bonferroni procedure because this latter is very conservative.

Another approach is to perform cluster-based inference. The advantage of cluster-based inference is that it takes into account the spatial correlation between voxels. The principle is to evaluate how likely were the inferred clusters to happen by chance. This involves to calculate descriptive statistics on the inferred clusters and to compare their values to a null-distribution. The usual descriptive statistics that can be computed are the **cluster-size** or the **cluster-mass**. The cluster-size is simply the number of voxels in the cluster and the cluster-mass is the sum of the T-statistic values in the cluster [90]. Cluster-mass is particularly interesting as it integrates information about the cluster-size and the effect-size. As there is no predefined null-distribution for cluster-size or mass, we need to construct it from the data. An efficient way to construct the null-distribution non-parametrically and that was implemented in BrainVISA is based on **random permutations** [91]. Finally, using the null-distribution, we can calculate the probability that a cluster could have appeared only by chance and declare the cluster as significant if this probability is smaller than some predefined threshold which is typically equal to 0.05 or 0.01.

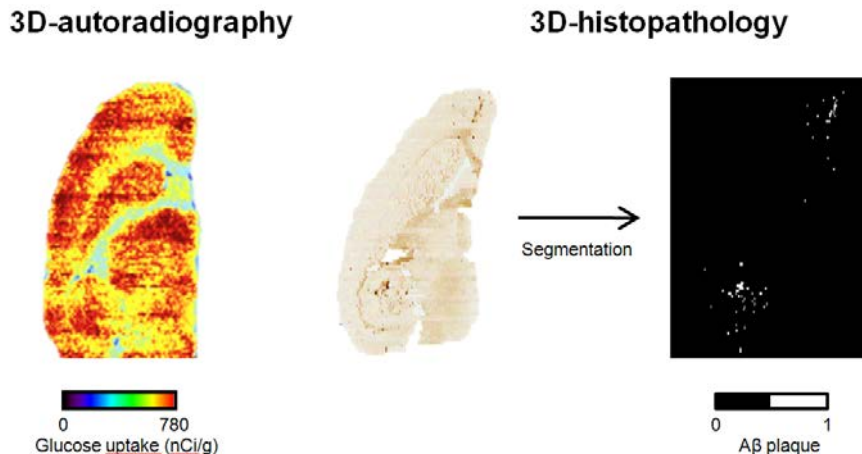


Figure 3.5: Axial views from 3D autoradiography imaging and 3D histopathology imaging in mouse models of Alzheimer’s disease (3D autoradiography image taken from Lebenberg *et al.* [67])

Can voxel-wise analysis be applied to 3D histopathology?

In the case of 3D histology, we would like to detect locations in the brain where the mean load of a given histopathological marker is different between groups of animals. For each individual of a 3D histopathology study, reconstruction and segmentation methods described earlier enable to generate a block-face photography volume as well as, in the same anatomical referential, a 3D whole-brain mask of the marker $M(x)$ such that for each voxel $M(x_i)$ with coordinates $x_i \in \mathbb{R}^d$:

$$M(x_i) = \begin{cases} 1 & \text{if the voxel corresponds to the staining and} \\ 0 & \text{otherwise.} \end{cases} \quad (3.1)$$

In contrast to autoradiography or PET imaging, histopathological markers appear as more or less densely distributed **discrete patterns** (Figure 3.5).

As block-face photography provides good anatomical contrasts, naturally, it can be used to create an anatomical template for the study. Subsequently, masks can be spatially normalized by registering them onto the anatomical template. After spatial normalization, in a study with 2 groups, for each voxel at coordinates x_i in the brain, we have 2 samples: $S^1 = \{M_1^1(x_i), M_2^1(x_i), \dots, M_{T_1}^1(x_i)\}$ and $S^2 = \{M_1^2(x_i), M_2^2(x_i), \dots, M_{T_2}^2(x_i)\}$. Using the 2 samples, the goal is to evaluate the

hypothesis

$$H_0 : \mu_{x_i}^1 = \mu_{x_i}^2 \quad (3.2)$$

against the alternate hypothesis

$$H_A : \mu_{x_i}^1 \neq \mu_{x_i}^2 \quad (3.3)$$

where $\mu_{x_i}^k = P(M^k(x_i) = 1)$ is the mean of the population k at the voxel x_i .

Naively, the sample mean

$$\overline{M^k(x_i)} = \frac{1}{T} \sum_{j=1}^T M_j^k(x_i) \quad (3.4)$$

could be used to estimate the population mean and significance testing could be carried out to test the null hypothesis. Although, we know that the sample mean tends to the population mean when the number of individuals gets very large, in preclinical studies the number of individuals per group is usually between 5 and 10. With this sample-size, $\overline{M^k(x_i)}$ has a very high-variance due to the binary nature of the data. For instance, if our sample has 5 individuals with the coordinates x_i never corresponding to the staining, $\overline{M^k(x_i)} = 0$ but if x_i were to correspond to the staining in only one individual, the estimate would jump to 0.2. In this context, **because of high-variance, the sample mean cannot be directly used to perform hypothesis testing.**

Another issue is that, **it is not realistic to look for voxel-level differences between groups at the microscopic scale.** This is mainly for 2 reasons:

- **Unattainable spatial normalization:** the block-face photography resolution is in the range of a few dozens of micrometers. Thus, small registration errors introduced during spatial normalization would lead to very important shifts at the microscopic scale.
- **Lack of interpretability:** microscopic differences between groups of animals would be hard to biologically interpret because their anatomical location would not be precisely identifiable based on our current knowledge of the brain anatomy.

The next section will present methods that can resolve these issues by (1) **reducing the image resolution** and (2) **providing more reliable voxel-wise estimates of histopathological marker load.**

3.2.2 Heat map generation

Thanks to the spatial correlation between voxels of one’s individual brain, we can improve the reliability of the sample mean by exploiting each voxel’s neighborhood. By properly combining together neighboring voxel values, we can produce a **low-resolution, smooth and continuous-scale image** that locally describes the load of the marker. We will refer to these images as **heat maps**. Each individual heat map from a group k is an attempt to estimate $P(M^k(x) = 1)$ from the discrete patterns in the mask. In spatial statistics, this is referred as intensity estimation. Most common methods for intensity estimation include binning, Voronoi tessalation [92] and Gaussian kernel smoothing. Before applying intensity estimation methods on a simulated dataset in the next section, we will briefly describe them and propose a novel method to tune Gaussian kernel smoothing.

Image binning

We can estimate the marker intensity, $H(x)$, via image binning. Images are simply partitioned into disjoint d -dimensional equally-sized windows and each voxel in $H(x)$, is assigned the maker occupation ratio in its corresponding window V_j :

$$H(x) = \sum_{x \in V_j} \frac{M(x)}{|V_j|}. \quad (3.5)$$

$H(x)$ forms a grid from which we can generate a smaller image which voxel-size is equal to the binning window-size. Thus, in addition of estimating the intensity, **image binning can be used to map large high-resolution images to smaller low-resolution images that are more suitable for voxel-wise analysis**. In practice, binning can be used systematically to reduce the size of the images before voxel-wise inference. The window-size can be determined by considering the original image resolution and the resolution at which we wish to study the marker of interest. **The choice of the heat map voxel-size is arbitrary but it should roughly correspond to the smallest cluster-size that would be biologically relevant.**

Voronoi tessalation

Another possibility is to use a Voronoi estimator. Voronoi tessalation consists in dividing the image into as many regions R_j as the number of particles so that each region corresponds to the particle area-of-influence. Thus, the intensity at each location x belonging to R_j can be estimated using the inverse of the region area and

the particle area:

$$H(x) = \sum_{x \in R_j} \frac{M(x)}{|R_j|}. \quad (3.6)$$

Equation 3.6 is equivalent to equation 3.5 but, contrary to image binning, Voronoi region sizes vary depending on the particle density. In low density areas, Voronoi regions will tend to be big and inversely, they will be small in dense areas. Contrary to binning and Gaussian kernel smoothing, **Voronoi tessalation is parameter-free** but it is rather computationally expensive on large images.

Gaussian kernel smoothing

The intensity can also be estimated via smoothing the mask $M(x)$ with a Gaussian kernel:

$$H(x) = \sum_{i=1}^n \frac{1}{(\sqrt{2\pi}h)^{\frac{d}{2}}} \exp \left[-\frac{1}{2} \left(\frac{\|x\| - \|x_i\|}{h} \right)^2 \right] M(x_i). \quad (3.7)$$

The choice of h , the Gaussian kernel standard deviation, is essential. The optimal h value is the one leading to an intensity estimation that has both low **variance** and low **bias**. Intrinsicly, there is a trade-off between variance and bias. Indeed, **if h is too small**, the intensity estimation will be wiggly from one voxel to another and the **sample mean will have a high variance**. The variance decreases monotonically as h increases, but **if h is too large**, images will be over-smoothed and **local spatial information about the marker of interest will be lost**.

Gaussian kernel standard deviation selection

Classically Gaussian kernel smoothing is used as a preprocessing step before voxel-wise inference in order to reduce noise and intra-group variance which could have been introduced by the image acquisition system or by small registration errors. The rule-of-thumb in the voxel-wise analysis literature is to use a Gaussian kernel with a full-width at half maximum equal to 3 times the voxel-size which is equivalent to a standard deviation of about 1.27 times the voxel-size. While this rule-of-thumb is very practical when dealing with noise, here, Gaussian kernel smoothing is not only used to limit noise but also to estimate the marker intensity. Typically, intensity estimation for a very sparsely distributed marker in the brain may require a larger kernel-size than intensity estimation for a very dense marker. In addition, if the sample-size is small, the Gaussian kernel size may need to be larger than for large sample-size. Therefore, it is crucial to adapt the kernel-size to the data at hand.

A practical way to choose the standard deviation would be to smooth the images with various kernel-sizes and to select the kernel size which provides the most visually appealing results. **An automatic method for optimal kernel-size selection is however desirable to ensure more objective results. The optimal Gaussian kernel-size is the one leading to the minimum mean squared error between the heat maps sample mean and the true underlying population mean:**

$$Err_{true}^k = \frac{1}{n} \sum_{i=1}^n (\hat{\mu}_{x_i}^k - \mu_{x_i}^k)^2, \quad (3.8)$$

where $\hat{\mu}_{x_i}^k = \overline{H^k(x_i)}$ is the heat map sample mean in group k at coordinates x_i . Of course, we do not know the population mean so we cannot explicitly calculate the **true error**. Nonetheless, if a second set of independently and identically distributed individuals was available, we could evaluate the heat map sample mean obtained from the first set of individuals by calculating how well it predicts the voxel values of these new individuals. We can use **squared loss function** to calculate the error between the heat map sample mean and a newly sampled individual:

$$L(M^k(x), \hat{\mu}_x^k) = \frac{1}{n} \sum_{i=1}^n (\hat{\mu}_{x_i}^k - M^k(x_i))^2, \quad (3.9)$$

where $M(x)$ is the mask of some individual drawn from population k and not used to estimate the heat map sample mean. In practice, we cannot spare individuals to create a validation set. To remedy this, we propose a **bootstrap sampling** approach. Bootstrap sampling is a simple yet powerful tool to create independent samples from the original sample. A bootstrap sample is generated by **sampling individuals with replacement**. It has the same size as the original sample with possible duplicates and some individuals may be left-out. In our procedure, a large number of independent bootstrap samples are drawn and heat maps are generated with individuals in the bootstrap samples. For each bootstrap sample b , we calculate $\hat{\mu}_x^{k,b}$, the sample mean of the heat maps included in the bootstrap sample. Finally, the **bootstrap error** [93] is calculated as follows:

$$\widehat{Err}_{boot}^k = \frac{1}{T} \sum_{j=1}^T \frac{1}{|C_{-j}|} \sum_{b \in C_{-j}} L(M_j^k(x), \hat{\mu}_x^{k,b}), \quad (3.10)$$

where T is the number of individuals in the original sample, C_{-j} is the subset of bootstrap samples that do not contain individual j and $|C_{-j}|$ is the number of such samples. The error is calculated for each group separately and can be averaged over

the groups to get a single, global, estimation of the error. In the next section, we will assess if the bootstrap error is minimized at the same Gaussian kernel-size that the true error using simulated data.

It should be noted that while Gaussian smoothing is described here with a **fixed standard deviation**, adaptive smoothing methods have been developed to locally select the Gaussian kernel standard deviation [94]. Potentially, adaptive Gaussian smoothing could be suited to estimate histopathological markers intensity as it allows to preserve spatial information in very dense regions while smoothing sparser regions. However, adaptive Gaussian smoothing relies on several parameters which have to be jointly tuned. Preliminary work on adaptive Gaussian smoothing showed that parameters optimization is non-convex and non-smooth (data not shown). Thus, it seemed much more difficult to obtain a robust estimation than for fixed standard deviation and this approach was not investigated any further.

3.2.3 Cluster detection with simulated data

The simulation dataset was designed to mimic images of segmented $A\beta$ plaques. Two types of images were generated to model individuals drawn from a **control population** and an **exacerbated population where $A\beta$ plaques are more frequent in spatially defined areas** (Figure 3.6). The goal was to infer the localization of the clusters as precisely as possible using the intensity estimation methods described in the previous section.

Poisson process simulations

$A\beta$ plaques were modeled as disks which radii were drawn from a Gaussian distribution and which centers correspond to seeds of a **Poisson process**. $A\beta$ plaques seeds localization was modeled using Poisson processes so that the probability of an $A\beta$ plaques being seeded at coordinates x of a simulation image is:

$$P(\text{seed}(x)) = \lambda(x)e^{-\lambda(x)} \quad (3.11)$$

where $\lambda(\cdot)$ is the intensity function of the $A\beta$ plaques seeds. The intensity can be held constant for every coordinate in the case of a homogeneous Poisson process or it can vary spatially in the case of an inhomogeneous Poisson process. Using $\lambda(\cdot)$ and the mean $A\beta$ size, **we can calculate the true population mean**, μ_x^k for each group k .

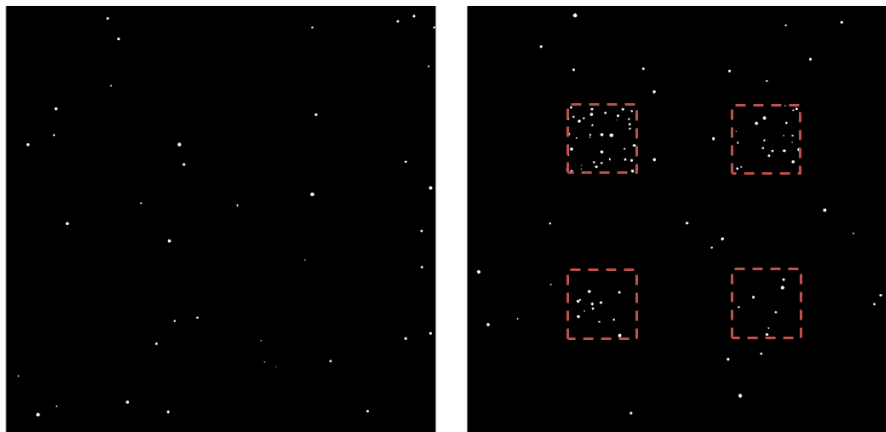


Figure 3.6: Simulation experiment with $\Lambda = 40$. An image from the control group is shown on the left and an image from the exacerbated group is shown on the right with the underlying cluster boundaries shown in orange dotted lines.

For images in the control group, $A\beta$ plaques were distributed according to a homogeneous Poisson process. In the exacerbated group, $A\beta$ plaques distribution was modeled by an inhomogeneous Poisson process with 4 square clusters where $A\beta$ plaques were more likely to appear. Three different experiments were carried out with various $A\beta$ plaques density conditions. In the first experiment, control group images had an expected total number of $A\beta$ plaques, Λ , equal to 40 which mimics the distribution of $A\beta$ plaques in a relatively low density condition. In the second and third experiments, $A\beta$ plaques density was increased with $\Lambda = 80$ and $\Lambda = 160$ respectively. In the exacerbated group, clusters had varying levels of exacerbation with increased probability of $A\beta$ plaques seeding of a factor of, respectively, 20, 10, 5 and 2.5 compared to the control group. Disks radii were drawn from a Gaussian distribution with the same mean and variance for both groups of images ($\mu = 7$ pixels, $\sigma = 2$ pixels). Seven pixels is a typical radius for an $A\beta$ plaque in an image with a pixel-size of $5 \mu\text{m}$. In each experiment, the control and the exacerbated group consisted of 10 images each. Simulation images had a size of 2560×2560 pixels.

Cluster detection

For each experiment, clusters were inferred using 3 different approaches. The first one consisted of image binning alone using a window size of 20 pixels. With a window size of 20, the binned image of a $5 \mu\text{m}$ resolution image would have a resolution of $100 \mu\text{m}$ which is a reasonable resolution at which to detect clusters of $A\beta$ load changes between groups. The second one consisted of a Voronoi estimator

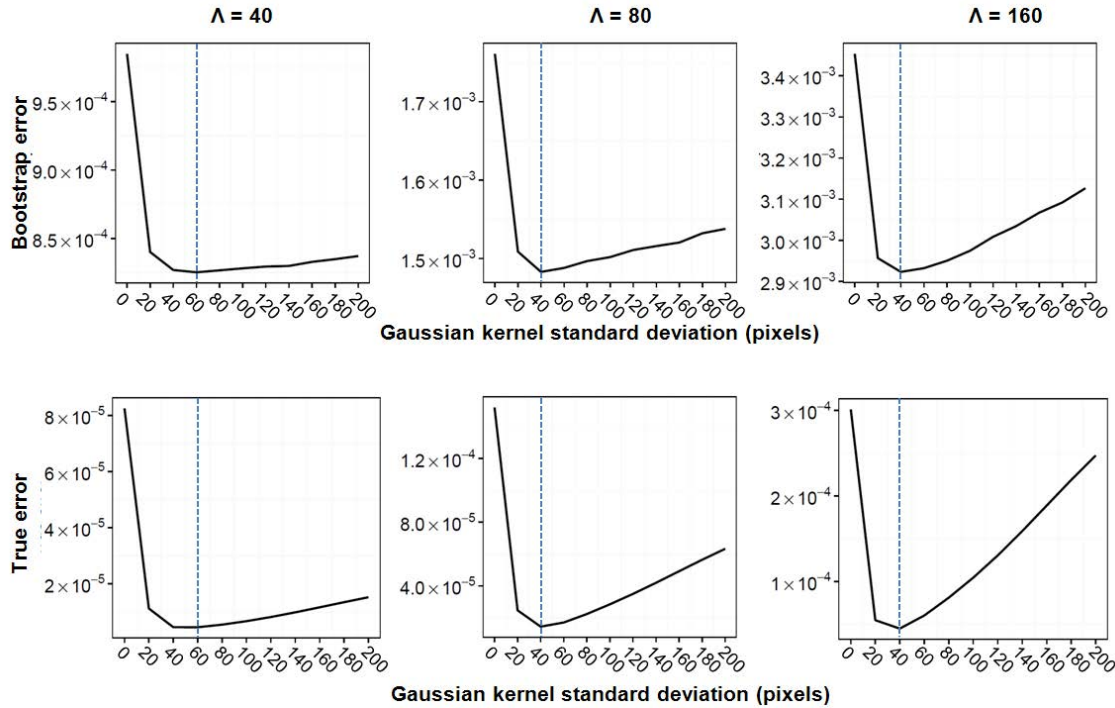


Figure 3.7: Gaussian kernel standard deviation selection for the three experiments (from left to right: $\Lambda = 40$, $\Lambda = 80$, $\Lambda = 160$). Bootstrap error (top) and true error (bottom) are shown for the exacerbated group. The bootstrap error was calculated using 1000 bootstrap samples. Ten Gaussian kernel sizes were tested, minima are indicated with a dashed blue line.

and a binning step and the last approach combined a Gaussian kernel smoothing which standard deviation was determined automatically through bootstrap error minimization and a binning step. **Each method was assessed by calculating the true mean squared error as described in equation 3.8.** Finally, **detected clusters were compared with the underlying true clusters.** F1 scores were calculated between detected and true clusters using the number of true positives (TP), false positives (FP) and false negatives (FN):

$$F1 = 2TP / (2TP + FP + FN). \quad (3.12)$$

Figure 3.7 illustrates Gaussian kernel-size selection using the bootstrap error. As it can be expected, the optimal kernel-size tends to decrease when the $A\beta$ plaque density increases (optimal sizes: 60 pixels, 40 pixels, 40 pixels for the experiments with, respectively, $\Lambda = 40$, $\Lambda = 80$, $\Lambda = 160$). For all three experiments, **the true error and the bootstrap error agreed on the optimal kernel-size which indi-**

cates that **the bootstrap error can be used to automatically tune Gaussian kernel smoothing when the population mean is not known**

From the images in Figure 3.8, we can see that each approach yields very different intensity estimations which results in very different cluster detection results as can be seen on Figure 3.9. Binning alone provided wiggly and noisy intensity estimation and it barely allowed to detect differences between the groups except for the last experiment with $\Lambda = 160$. This can be explained by high-variance of the binning estimator with the chosen window size. Concerning Voronoi estimation, as it can be expected, the intensity estimation in the cluster areas was higher in the exacerbated group than in the control group but this increase spread far outside the borders of the clusters. While the Voronoi estimator allowed to detect differences between the groups, the clusters shapes were not recovered properly and, overall, the cluster sizes were overestimated as a result of imprecise intensity estimation. The Gaussian kernel estimation yielded smooth intensity estimation and, overall, the clusters shapes were recovered. As it could be expected, detection of the clusters with the highest intensity difference between the groups was slightly over-estimated while the detection of clusters with mild difference between groups was slightly under-estimated. This discrepancy could be addressed using adaptive Gaussian kernel smoothing [94]. Table 3.1 shows that the intensity estimation error and the F1 scores were systematically better when using the Gaussian kernel smoothing.

In conclusion, in this simulation study, the **Gaussian kernel smoothing combined with image binning provided the best results across experimental conditions**. It should be noted that this conclusion only holds for the range of Λ values explored here. Indeed, the simulation study was intended to mimic the distribution of $A\beta$ plaques which are rather sparsely distributed in the brain. This conclusion may not hold if studying, much more densely distributed objects such as neurons. Thus, for each kind of markers, tailored simulation studies may be useful to pick the best estimation method prior to performing voxel-wise inference on real-data. In this study, the $A\beta$ plaque sizes were identically distributed for both groups. An interesting perspective would be to study the influence of objects size on cluster detection. Finally, the simulation study showed that the bootstrap error minimum predicts the true error minimum and that Gaussian-kernel smoothing with the optimal kernel-size ensures an accurate cluster detection. Therefore, the **bootstrap error can be used to select the Gaussian kernel standard deviation for real studies when the underlying clusters are unknown**.

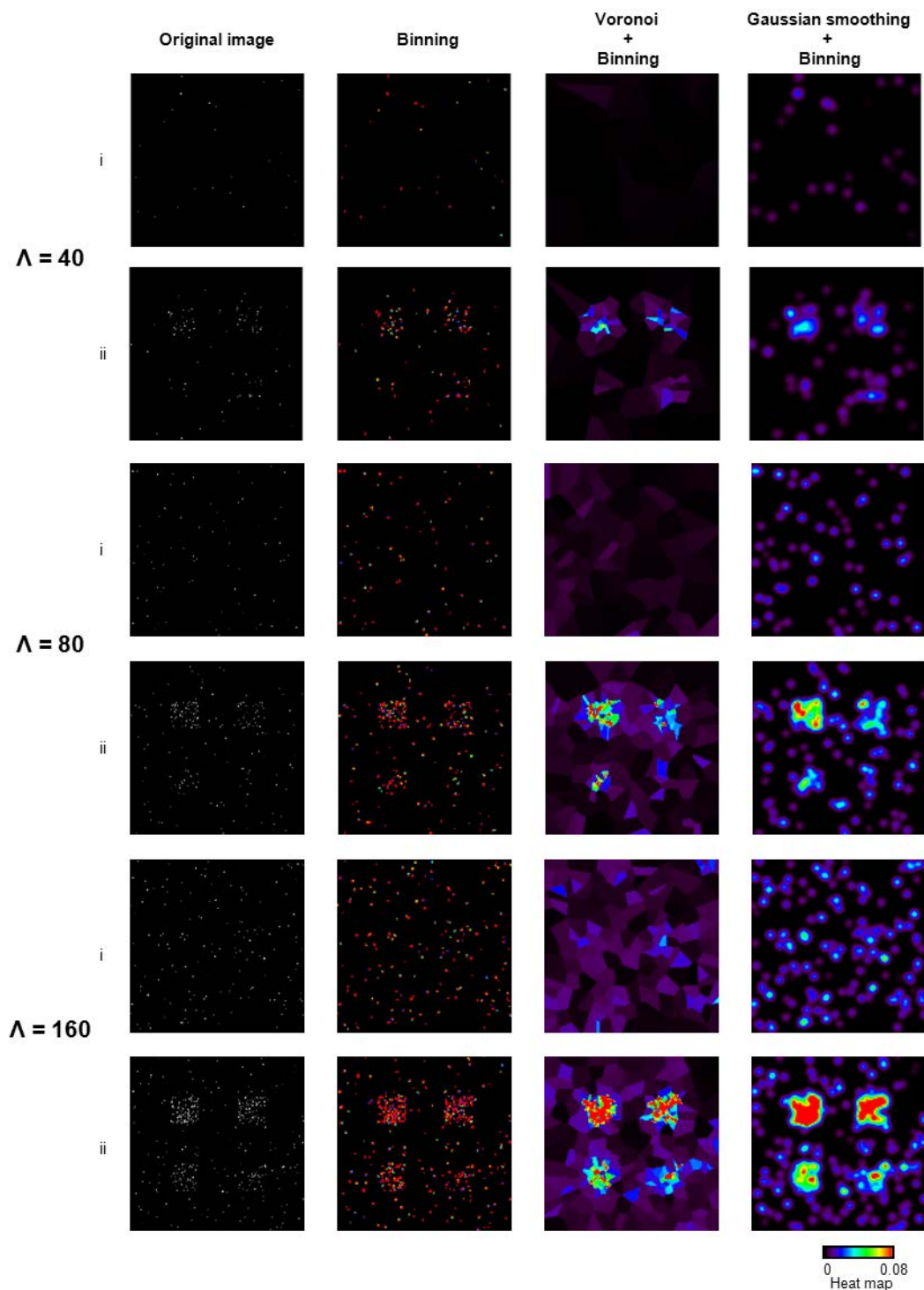


Figure 3.8: Heat map generation. For each of the three experiments, examples are shown with an image from the control group (i) and an image from the exacerbated group (ii). From left to right: original image, heat map generation with binning; heat map generation with Voronoi tessellation and binning; heat map generation with Gaussian smoothing with automatic kernel-size selection and binning.

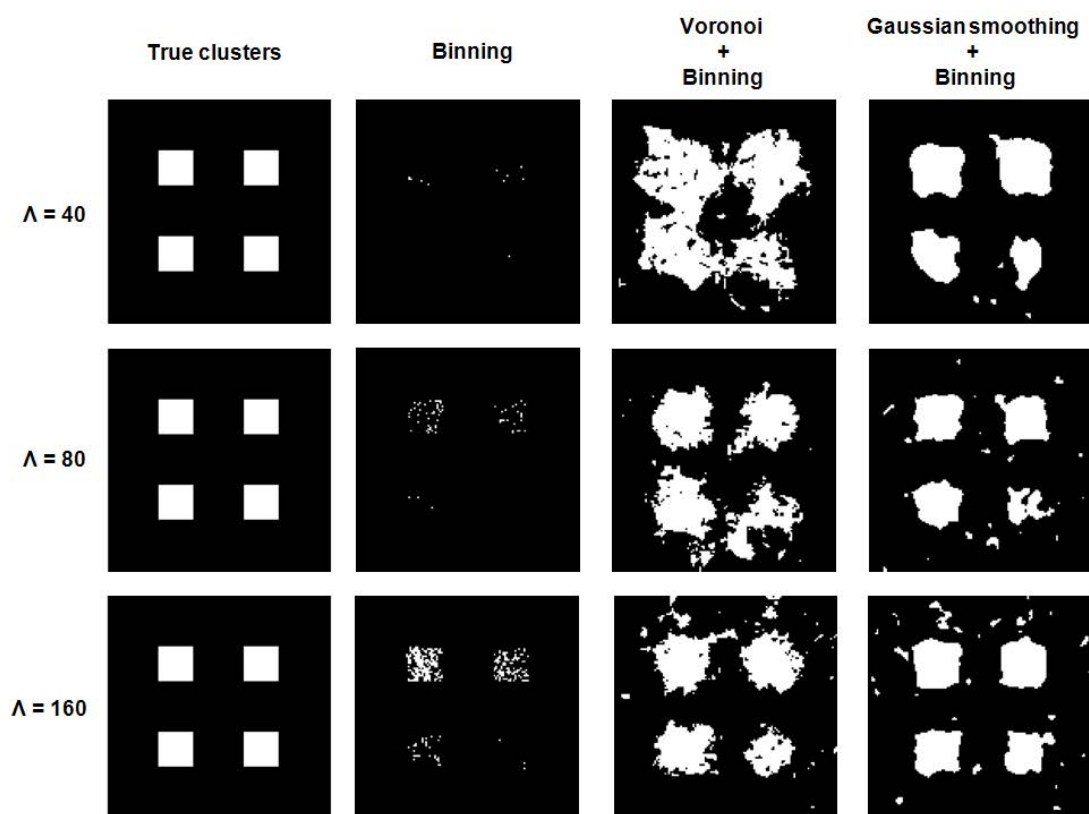


Figure 3.9: Clusters detection for the three experiments. Clusters were detected with a voxel-wise t-test at a significance threshold $\alpha = 0.05$ without correction for multiple comparison.

Method	True Error	F1
$\Lambda = 40$		
Binning alone	8.26×10^{-5}	0.13
Voronoi + Binning	8.27×10^{-6}	0.44
Gaussian smoothing + Binning	4.25×10^{-6}	0.74
$\Lambda = 80$		
Binning alone	1.52×10^{-4}	0.07
Voronoi + Binning	2.67×10^{-5}	0.55
Gaussian smoothing + Binning	1.44×10^{-5}	0.76
$\Lambda = 160$		
Binning alone	3.01×10^{-4}	0.37
Voronoi + Binning	8.14×10^{-5}	0.64
Gaussian smoothing + Binning	4.48×10^{-5}	0.73

Table 3.1: True error and cluster detection F1 scores for each method on the simulated dataset. Best scores appear in boldface.

CHAPTER 3: BRAIN-WIDE QUANTITATIVE ANALYSIS OF NEUROPATHOLOGICAL MARKERS

Chapter 4

Applications in mouse models of $A\beta$ deposition

4.1 Context of the studies

This chapter gives proofs of concept that 3D quantitative histopathology can be used on a large scale in studies on Alzheimer’s disease. The datasets come from studies involving three transgenic mouse strains: the $APP_{swe}/PS1dE9$, the $APP_{Sl}/PS1_{M146L28}$ and the $APP_{Swe,Ind}$ mouse strains. All these mouse models of Alzheimer’s disease harbor mutations which in humans are associated with the familial form of Alzheimer’s disease and lead to a significant $A\beta$ deposition in mice. For each study, protocols for the *in vivo* experiments, histology and imaging will be described. The image processing and analysis steps were all performed in BrainVISA and will only be briefly addressed as they have already been described in the previous chapters. Except for voxel-wise analysis, statistical analyses were performed in the R statistical environment. Summarized information about mouse models and experimental procedures can be found in the Appendix B.

The **first study** was initially aimed at evaluating the effect of a natural product extract on the $A\beta$ load and the glucose metabolism in $APP_{swe}/PS1dE9$ mice. The extract did not seem to have an effect whatsoever on the $A\beta$ load (data not shown) but the dataset was interesting in that it allowed to characterize a very popular mouse model of Alzheimer’s disease. Indeed, $APP_{swe}/PS1dE9$ are commonly used in preclinical research but **the distribution of the $A\beta$ pathology in various brain regions is yet to be established.**

The **second study** aimed at evaluating the effect of 13C3a, a new anti- $A\beta$ immunotherapy developed by Sanofi, on the $A\beta$ load in $APP_{Sl}/PS1_{M146L28}$ mice.

Anti- $A\beta$ immunotherapy for Alzheimer’s disease have been an active field of research since the late 90’s [95]. While many monoclonal antibodies have shown promising results in preclinical experiments, some concerns have been raised regarding their potential toxic effect in the human brain. Indeed, antibodies trigger inflammation response causing so called Amyloid Related Imaging Abnormalities that are observable with MRI. 13C3a is innovative because its structure have been engineered in a way that it does not trigger inflammation [96]. This could result in a much safer immunotherapy for Alzheimer’s disease. While the inflammation response can cause toxic side effects, it is also believed to have an essential role to lower the $A\beta$ load. In this study **we assessed whether the 13C3a can reduce the $A\beta$ load in $APP_{Sl}/PS1_{M146L28}$ mice** even if the inflammation response is restricted. In addition, this dataset was used to **validate and compare 3D quantitative histopathology against a more conventional histology quantification protocol performed by collaborators at Sanofi**. In addition to the histological investigation of 13C3a effect on $A\beta$ pathology, this study was also the opportunity for our collaborators at MIRCen (Marc Dhenain’s group) to investigate the effect of 13C3a on $A\beta$ load using an innovative *in vivo* MRI protocol that has been designed to visualize $A\beta$ plaques [58]. Here, our contribution was to assess the agreement between *in vivo* MRI measures and 3D histopathology quantification. These results are presented in Chapter 5. Finally, this dataset was also the opportunity to initiate the extension of 3D quantitative histopathology to cellular markers analysis and preliminary results are presented in Chapter 5.

The **third study** aimed at **assessing the effect of the over-expression of ADAM30 on the $A\beta$ load in $APP_{Swe,Ind}$ mice**. ADAM30 is a relatively poorly studied metalloprotease which has been recently linked to Alzheimer’s disease. Our collaborators at Institut Pasteur de Lille found that this protein is significantly less expressed in the brain of patients with Alzheimer’s disease compared to healthy controls. In addition, they found that the $A\beta$ protein levels in the brain negatively correlate with ADAM30 expression in humans. While this observation corroborate a link between ADAM30 expression and the $A\beta$ pathology, a causal link is yet to be demonstrated. Animal experiments can be carried-out to solve this question. ADAM30 expression is very low in mice but it is possible to genetically engineer mice to over-express ADAM30. By studying the effect of ADAM30 over-expression in mice that develop an $A\beta$ pathology, we can directly assess the effect of ADAM30 on $A\beta$ plaques. If ADAM30 is indeed a modulator of the $A\beta$ pathology it could constitute a novel drug target in Alzheimer’s disease. **Initially, our contribu-**

tion to this large-scale collaborative study was to evaluate the effect of ADAM30 on the $A\beta$ load in $APP_{Swe,Ind}$ mice using the ontology-based approach. Following this initial work, we further applied voxel-wise analysis to refine the evaluation of ADAM30 on the $A\beta$ load. Results from both approaches are presented and discussed.

4.2 Study 1: animal model characterization

4.2.1 Experimental procedures

In vivo study

In the first study, ten male $APP_{Swe}/PS1dE9$ mice were initially included in the animal model characterization study. Three mice died prematurely. Mice were euthanized at the age 13.5 months with lethal injection of sodium pentobarbital; brains were rapidly removed and snap-frozen in isopentane. Seven brains were kept for further analysis.

Tissue processing, histology and image acquisition

Fresh brains were snap frozen and embedded in a mixture of M1 embedding matrix (Thermo Fisher Scientific) and Fast Green (Sigma-Aldrich) before being entirely cut on a CM3050S cryostat (Leica). Four batches of serial coronal brain sections ($20\ \mu\text{m}$), ranging from the brain frontal pole to the end of the caudal part of the cortex, were collected, mounted on superfrost slides and quickly dried. The first series was dedicated to Nissl staining. The fourth series was dedicated to $A\beta$ plaque staining. The remaining series were stored at -80°C until processing. Images from the surface of the block were recorded every fourth section (before each section of the first series was cut) with a digital camera (Powershot G5 Pro, Canon) at a lateral resolution of $27\ \mu\text{m}$.

For the Nissl staining series, sections were stained in a solution of cresyl violet with the Shandon Varistain 24-4 automate (Thermo Electron Corporation).

To highlight $A\beta$ peptide aggregates, after post-fixation in 4% paraformaldehyde, IHC staining was performed with BAM10 primary monoclonal antibody (Sigma-Aldrich), a biotinylated secondary antibody (Vector Laboratories) and staining was revealed with DAB detection kit (Ventana Medical Systems, Roche). IHC experiments were performed with the automate Discovery XT (Ventana Medical Systems,

Roche). All the sections were processed identically. Sections were counter-stained with Bluing Reagent (Ventana Medical Systems, Roche).

A flatbed scanner (ImageScanner III, G.E. Healthcare) was used to digitize Nissl-stained series of sections (lateral resolution: 21 μm) and A β plaque series (lateral resolution: 5 μm).

4.2.2 Ontology-based characterization of A β deposition

Tissue section images were reconstructed in 3D according to the methods described in section 2.3. As the staining was reproducible and well contrasted, the A β plaque IHC volumes could be segmented using the BioVision algorithm. Finally, the mouse brain atlas was registered to each mouse brain block-face photographic volume.

After reconstruction of the 7 brains from 13.5 months old APP/PS1dE9 mice (Figure 4.1a), we took advantage of the brain ontology to quantify A β plaque deposition at different levels of the brain (Figure 4.1b,c). A β load peaked in the cortical regions and the hippocampus. Those results agree with previously published works reporting massive amyloid deposition in these regions in aged APP/PS1dE9 mice [97]. Furthermore, **ontology driven analysis highlighted infrequently examined ROIs presenting substantial A β deposition such as basal ganglia and white matter tracts.**

4.3 Study 2: preclinical immunotherapy evaluation

4.3.1 Experimental procedures

In vivo study

In the second study, twenty female APP/PS1 mice were initially included at the age of 5 months in the therapy evaluation study. They received weekly intraperitoneal injections of either 13C3a, an anti-A β peptide antibody (Sanofi, 10 mg/kg) or DM4, a control antibody (Sanofi, 10 mg/kg) for 3 months. In addition, 4 PS1 mice were included in the study as negative controls (PS1 mice are A β plaque free). At 5 and 8 months of age, APP/PS1 mice as well as PS1 mice received intracerebroventricular injections of gadolinium and 3D Gradient-echo MRI scans (x, y, z resolution: 29 \times 29 \times 117 μm^3) were recorded on a 7T-Spectrometer (Agilent) [58]. The second imaging session was performed just before euthanasia and brain removal. This protocol was

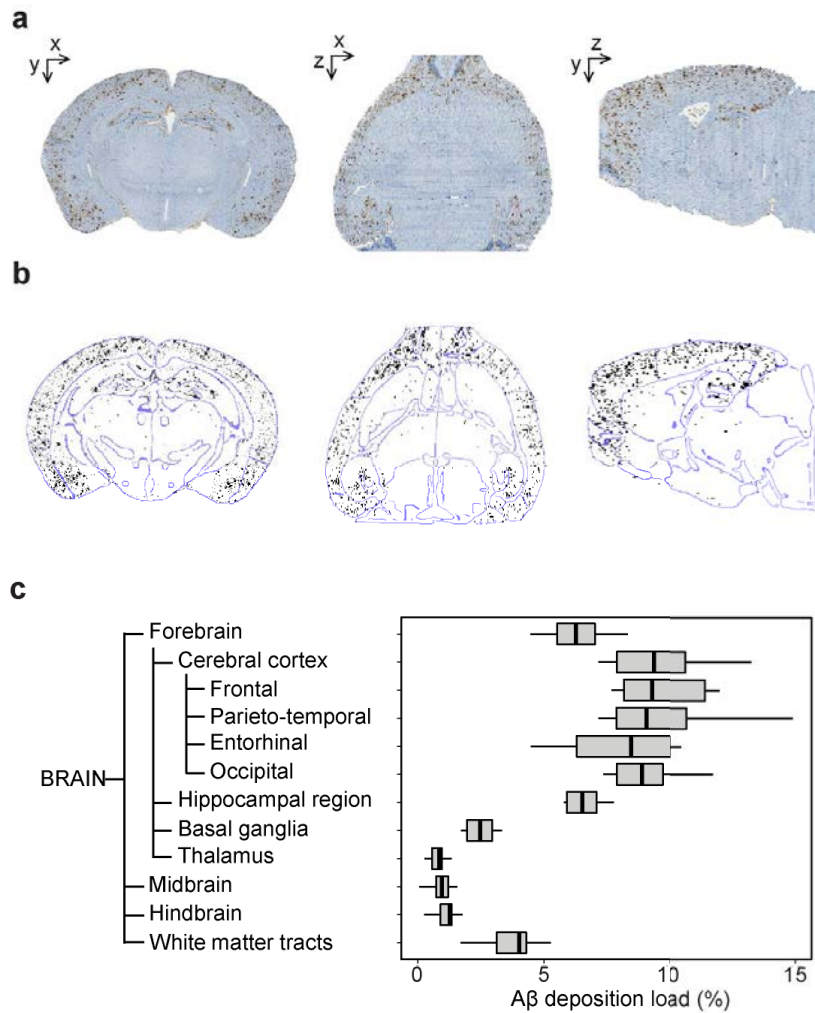


Figure 4.1: (a) A representative reconstructed $A\beta$ plaque volume in the coronal (left), axial (middle) and sagittal (right) views. (b) Segmented $A\beta$ plaque (black) superimposed with the atlas contours (blue). (c) $A\beta$ load quantification in 13.5-month-old APP/PS1dE9 mice (N=7). Boxplots upper and lower hinges correspond to the first and third quartiles. The whiskers extend from the hinges to the highest or lowest values that are within $1.5 \times$ inter-quartile-range. Bold lines represent median values.

used to visualize A β deposits *in vivo*. The correlation between A β detection with MRI and histology imaging will be the main topic of section 5.1.

At this stage, due to the high mortality rates of APP/PS1 transgenic mice, especially in the control-treated group, 8 13C3a-treated APP/PS1 mice and 3 DM4-treated APP/PS1 mice were included for analysis.

Tissue processing and histology

Brains from APP/PS1 and PS1 mice were processed by *NeuroScience Associates* using the Multibrain technology. Formalin-fixed brains were all embedded in one green-colored solid matrix to obtain a sharp contrast between the embedding material and the cerebral tissue. Brains were subsequently frozen and cut into 25 μm -thick serial coronal brain sections. Block-face photographs were recorded at a lateral resolution of 33 μm every fifth section (EOS Rebel T2i, Canon). The first series of sections was used for Nissl staining, the second for A β deposits staining (6E10 monoclonal antibody IHC), the third for phagocytic cells staining (anti-CD68 monoclonal antibody IHC) with a Nissl counterstaining, the fourth for blood brain barrier (BBB) disruptions staining (anti-IgG monoclonal antibody IHC) the fifth for microglia staining (anti-Iba1 monoclonal antibody IHC) with a Nissl counterstaining.

Nissl-stained series and A β IHC stained series were further processed to evaluate the anti-A β effect of 13C3a and the remaining 4 series were kept for further analysis (see chapter 5)

Image acquisition

Similarly to the first study, Nissl-stained series of sections and A β plaque series were imaged with a flatbed scanner (ImageScanner III, G.E. Healthcare) at a lateral resolution of, respectively, 21 μm and 5 μm . A subset of 8 A β -deposit-stained sections per animal was acquired at a lateral resolution of 0.35 μm with an Olympus VS120-S5 whole slide imaging microscope. These latter images were used to perform the routine 2D quantification protocol of A β deposition.

4.3.2 Whole-brain therapeutic intervention evaluation

3D brain reconstruction was performed for each mouse brain as described in previous section 2.3. The A β plaque IHC staining was highly contrasted and reproducible, therefore 3D histopathology volumes were segmented using the BioVision algorithm

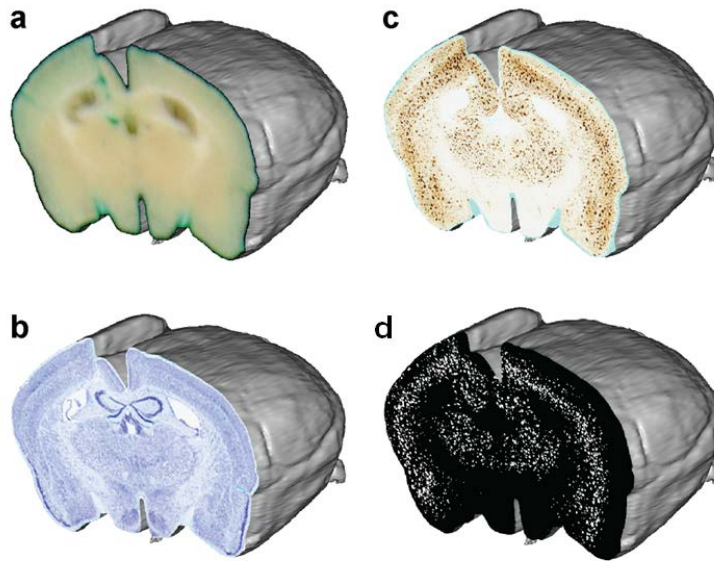


Figure 4.2: 3D histopathological volumes. (a) Block-face photographic volume. (b) Nissl volume displaying brain anatomy. (c) 6E10 immunohistochemistry (IHC) volume showing $A\beta$ pathology. (d) Segmented 6E10 IHC volume ($A\beta$ plaques appear in white).

(Figure 4.2). The MICE brain atlas was registered using the FFD to each mouse brain block-face photographic volume as described in section 3.1.2.

We evaluated the effect of a new anti- $A\beta$ immunotherapy in 8-months-old APP/PS1 transgenic mice in the entire brain and in four ROIs (cerebral cortex, striatum, hippocampal region and thalamus). As expected, $A\beta$ deposition load was close to none in brains of PS1 mice (Figure 4.3). We compared $A\beta$ deposition between APP/PS1 mice treated with either the anti-amyloid immunotherapy (13C3a) or the control antibody (DM4). In brains of APP/PS1 mice, 13C3a lowered $A\beta$ deposition compared with DM4 (Mann-Whitney test, $p < 0.05$; Figure 4.3). Besides, we detected a statistically significant $A\beta$ lowering effect of 13C3a in the cerebral cortex, the striatum and the thalamus but not in the hippocampal region (Table 4.1). Nevertheless, results regarding the effect of 13C3a should be taken carefully due to the small sample size of this study. Here, the analysis was limited to the entire brain and to 4 ROIs in order to avoid type I errors due to multiple comparisons. Also, the group sample sizes in APP/PS1 mice were too small to perform voxel-wise statistical analysis with proper correction for multiple comparisons.

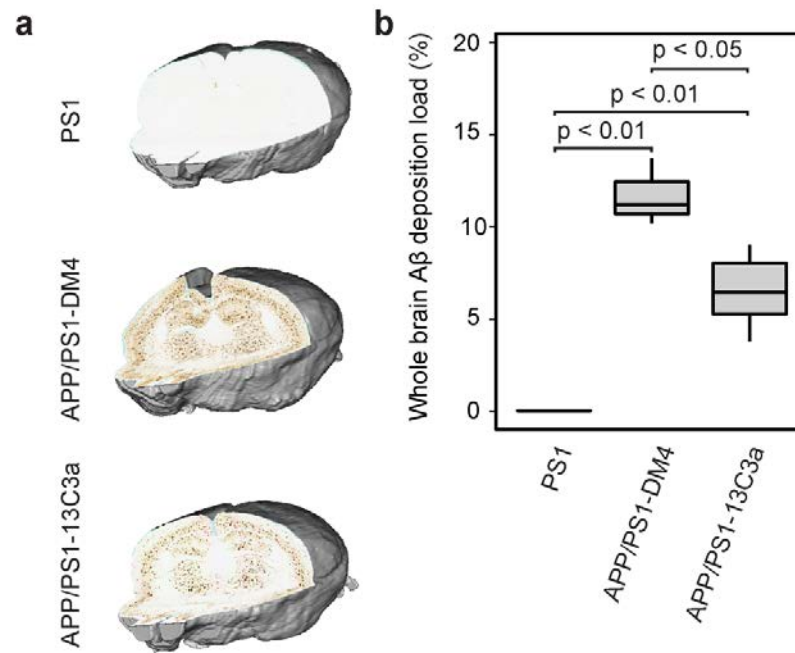


Figure 4.3: Brain-wide anti- $A\beta$ effect of 13C3a. (a) Reconstructed $A\beta$ deposition IHC volumes for one representative brain per group. (b) Reduction of $A\beta$ deposition in APP/PS1 mice treated with 13C3a (N=8) compared to mice treated with DM4 (N=3). PS1 mice are shown as negative controls (N=4) (Mann-Whitney tests, boxplot representation is the same as in Figure 4.1).

ROI	APP/PS1-13C3a (N = 8)	APP/PS1-DM4 (N = 3)	PS1 (N = 4)
Whole brain	6.61 \pm 2.75 * ^{oo}	9.84 \pm 1.80 ^{oo}	0.04 \pm 0.01
Cerebral cortex	10.43 \pm 3.21 * ^{oo}	18.48 \pm 3.45 ^{oo}	0.05 \pm 0.15
Striatum	1.79 \pm 0.9 * ^{oo}	4.72 \pm 0.64 ^{oo}	0.04 \pm 0.02
Hippocampal region	11.06 \pm 3.23 ^{oo}	16.36 \pm 3.33 ^{oo}	0.03 \pm 0.08
Thalamus	7.21 \pm 1.55 * ^{oo}	9.51 \pm 0.54 ^{oo}	0.03 \pm 0.02

Table 4.1: A β lowering effect of 13C3a immunotherapy in APP/PS1 mice. Data shown: mean \pm SD. * p<0.05 13C3a-treated APP/PS1 mice versus DM4-treated APP/PS1 mice (Mann-Whitney tests). ^{oo} p<0.01 versus PS1 mice (Mann-Whitney tests)

4.3.3 3D versus 2D histopathology comparison

A 2D quantification protocol was performed in order to validate 3D histopathology results and compare both approaches. Image analysis was performed with Mercator software (*Explora Nova*) by an expert from Sanofi who was blind to the quantification results obtained with the 3D quantification approach. Four ROIs (cerebral cortex, hippocampal region, striatum and thalamus) were selected for the analysis. The cerebral cortex was manually outlined on 8 sections per animal. The hippocampal region, the striatum and the thalamus were present and were outlined on 3 to 4 sections out of the 8 selected sections per animal. A threshold that appropriately separated A β plaques from the remaining unstained tissue was manually defined on one section and then applied to all images (Figure 4.4). Finally, A β deposition load was calculated in each selected ROI of each animal.

We validated that A β load quantification is consistent between the 3D whole-brain quantification and an independently performed 2D routine quantification protocol with a few sections per ROI. We correlated results for both methods in the 4 examined regions (cerebral cortex, striatum, hippocampal region and thalamus) in APP/PS1 transgenic mice (Figure 4.5a). Overall, the two methods well correlated but showed various levels of agreement according to the ROI (Spearman's $\rho = 0.97$, $p < 0.001$ in the cerebral cortex; $\rho = 0.96$, $p = 0.001$ in the striatum; $\rho = 0.88$, $p = 0.001$ in the hippocampal region; $\rho = 0.81$, $p = 0.001$ in the thalamus). We further attempted to explain differences between ROIs, by investigating the effect of lowering section sampling on A β load quantification. Using 3D histopathological data, simulations were performed for each animal by progressively discarding equidistant sections from the analysis and generating all possible combinations of sections at a given sampling rate. We then quantified A β deposition for each subset

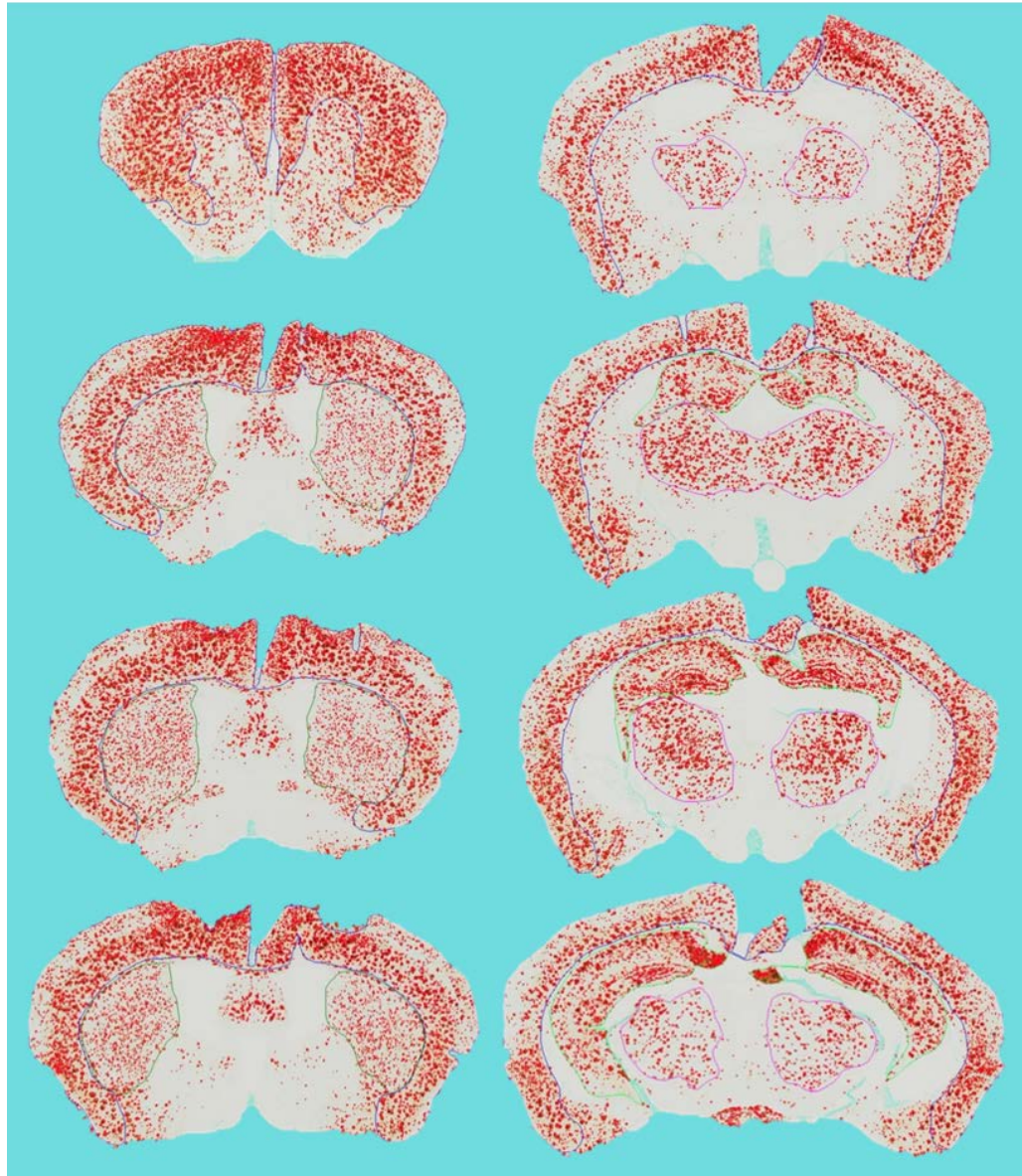


Figure 4.4: Standard $A\beta$ load quantification on 8 sections from an APP/PS1 mouse brain. Original images are superimposed with the $A\beta$ plaque binary mask (red) as well as with manually delineated brain ROIs. Cerebral cortex borders appear on every section in blue, striatum borders appear in green on sections 2-4 (left), hippocampal region borders appear in green on sections 6-8 (right) and thalamus border appear in pink on sections 5-8 (right).

and calculated the relative error to which the subset quantification deviated from reference 3D quantification as:

$$Error = \frac{|x_{subset} - x_{reference}|}{x_{reference}}, \quad (4.1)$$

where x_{subset} is the A β deposition load calculated with a simulated subset of sections and $x_{reference}$ is the A β deposition load when all sections are taken into account.

Figure 4.5b shows the effect of section sampling lowering on A β deposition quantification relative error. When decreasing sampling rate, the relative error remained relatively low in the cerebral cortex and in the striatum but increased in the thalamus and the hippocampal region, up to median relative errors of, respectively, 17.3 % and 11.9 % for subsets of 1.875 mm-separated sections. This corresponds to subsets of 2 or 3 sections per ROI which is fairly common in the literature (section 1.1.3). To better understand discrepancies between ROIs, A β load rostro-caudal dispersion was quantified for each ROI (coefficients of variation: 39% in the cerebral cortex, 37% in the striatum, 44% in the hippocampal region and 55% in the thalamus, Figure 4.5c,d). This indicates that differences between the 2D quantification approach and 3D histopathology can be explained by variations in marker spatial distribution inside ROIs.

4.4 Study 3: gene effect evaluation

4.4.1 Experimental procedures

In vivo study

Two transgenic mouse strains with a C57Bl6N background were generated (Taconic) either carrying the ADAM30 gene with a Cre promoter enabling its expression or only the ADAM30 gene. ADAM30-Cre mice express ADAM30 conditionally upon Neomycine-mediated Cre activation while the second line do not express the gene because the Cre is absent and, thus, served as negative control to test the effect of ADAM30 on the A β load. Conditional expression allowed to initiate ADAM30 expression after at the age of 3 months to avoid any confounding effect of ADAM30 on brain development. Cre-ADAM30 and ADAM30 mice were crossed with hAPP_{Swe,Ind} mice expressing the human APP gene bearing “Swedish” and “Indiana” mutations which are associated with familial forms of Alzheimer’s disease and cause pathological A β deposition (Jackson Laboratory) [98].

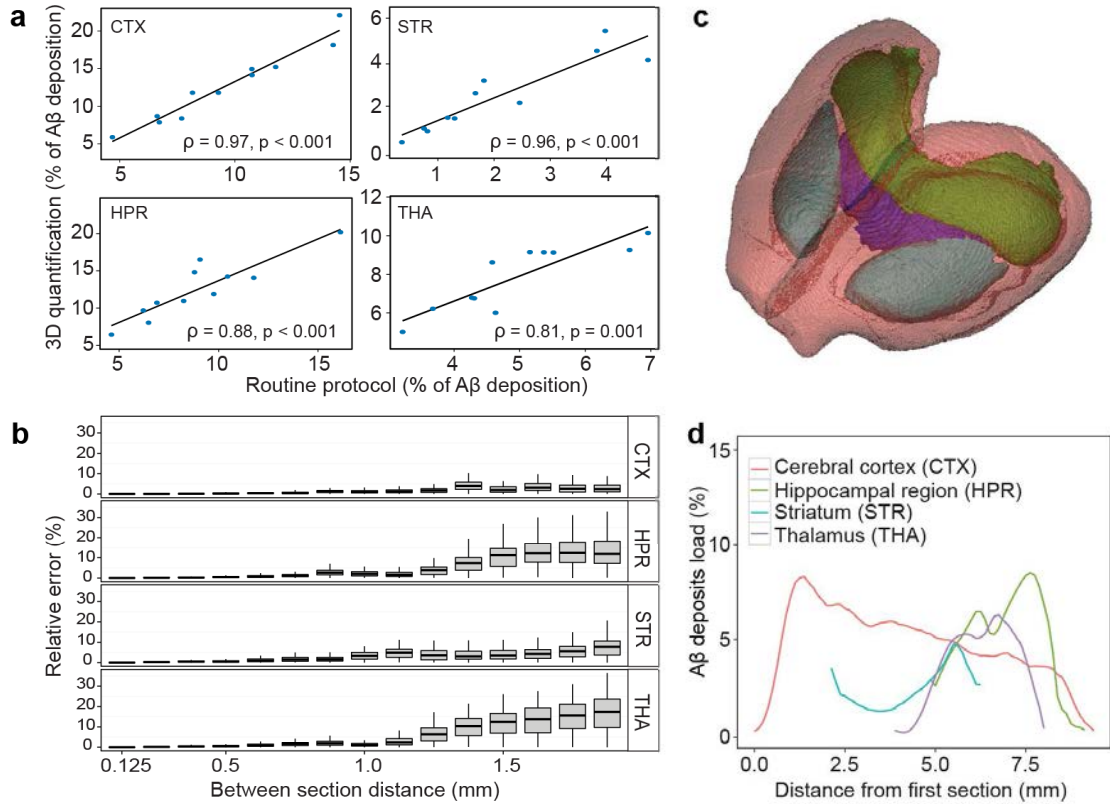


Figure 4.5: 3D quantification and 2D quantification correlation. (a) Correlations of A β deposition quantification using brain-wide histopathology and a routine quantification protocol in the 4 selected ROIs (CTX: cerebral cortex, STR: striatum, HPR: hippocampal region, THA: thalamus) in APP/PS1 mice (N=11, Spearman's rank correlation). A linear regression line is shown in black. (b) Relative error of A β deposition measures when increasing the distance between analyzed equidistant sections in APP/PS1 mice (N=11). Boxplot representation is the same as in Figure 4.1. (c) A 3D rendering of 4 selected ROIs (cerebral cortex in red, striatum in light blue, hippocampal region in green and thalamus in purple). (d) A β deposition distribution profile along the rostro-caudal axis in an APP/PS1-13C3a mouse in the 4 selected ROIs.

At 10 months of age, 10 $APP_{Swe,Ind-Cre-ADAM30}$ and 5 $APP_{Swe,Ind-ADAM30}$ were euthanized, the brains were removed from the skull and freshly frozen. For each individual, one hemi-brain was used for 3D histology investigations.

Tissue processing, histology and image acquisition

Hemi-brains were all embedded in one green-colored solid matrix to obtain a sharp contrast between the embedding material and the cerebral tissue (Neuroscience Associates). For each brain, 3 sets of 30- μm -thick coronal sections (n=100 per set) were collected. One set was used for $A\beta$ -peptide IHC experiments with a 6E10 monoclonal antibody and a DAB revelation. The two other series were kept for further analysis.

Block-face photographs of the brain were taken (lateral resolution: 13 μm) before each section was cut (EOS 5D Mark III, Canon). The resulting images could be stacked to yield a 3D coherent brain volume for each subject that respects the geometry of the brain [84].

All histology section images were digitized using a flatbed scanner (ImageScanner III, GE Healthcare) with a lateral resolution of 5 μm .

4.4.2 Image processing

3D reconstruction and template generation

For each individual, 3D reconstruction of block-face photographs and histology section images was done as described earlier in section 2.3 (Figure 4.6a). The mean anatomical template was generated by, first, registering all the block-face photography volumes onto one chosen reference block-face photography volume and then by calculating the mean image from the registered block-face photography volumes (Figure 4.6b).

3D registration between each block-face photography volume and the reference block-face photography volume was performed in 3 steps. Similarly to what was described in section 3.1.2 for digital atlas registration, a global rigid transformation was estimated based on mutual information similarity criterion, and then, an affine registration initialized with the rigid transformation was performed with the Block-Matching technique [64]. Finally, a non-linear transformation was computed using the FFD algorithm to improve registration locally [81].

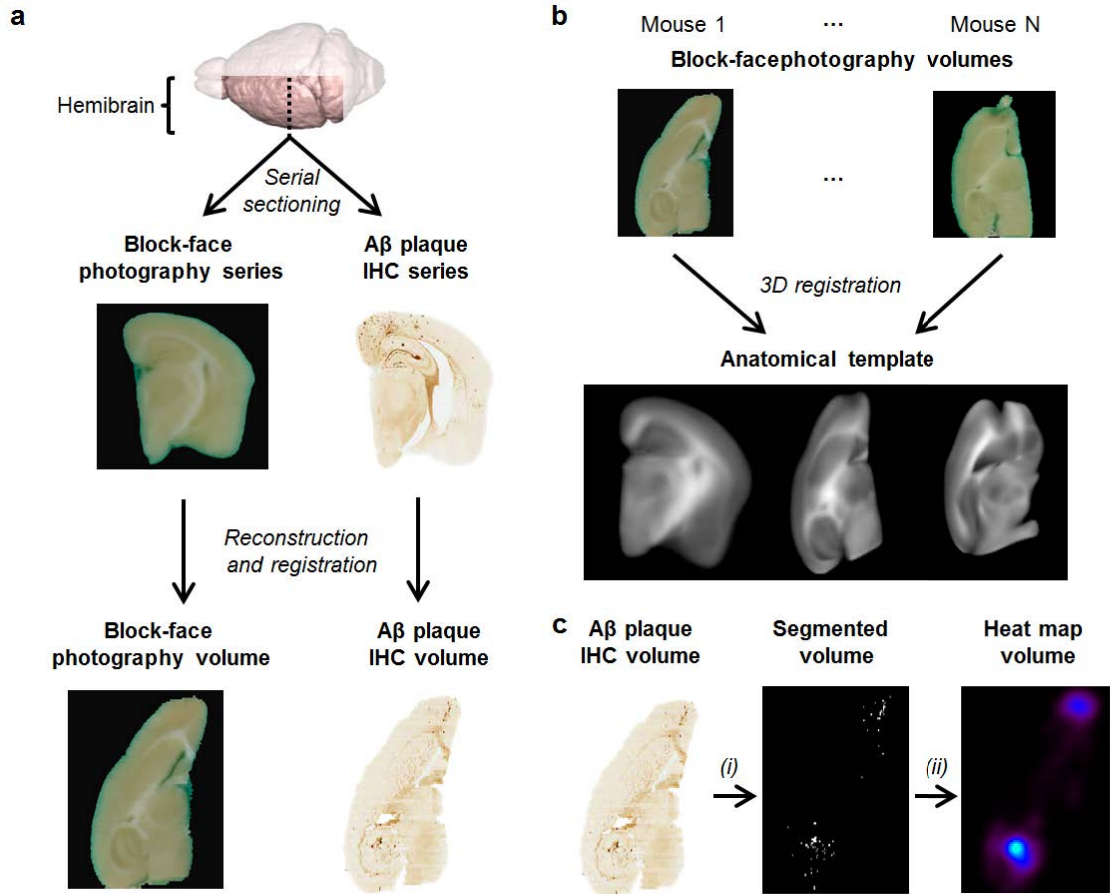


Figure 4.6: Overview of the image processing steps. (a) 3D reconstruction of block-face photography and histology volumes. The block-face photography volume for each mouse is generated by simply stacking each photograph. $A\beta$ plaque IHC stained section images are stacked and registered to their corresponding block-face photographs to provide $A\beta$ IHC coherent volumes for each mouse. (b) The anatomical template is generated by registering every block-face photography volume onto a common reference. (c) $A\beta$ plaques are segmented on histology volumes using Weighted Random Forest (i) and continuous-scale quantitative heat map volumes are derived from the binary volumes (ii).

Histology image segmentation

When this dataset was first analyzed as part of the initial collaboration with Institut Pasteur de Lille, we used BioVision to segment $A\beta$ plaques. Due to high non-specific staining in this mouse model, heavy manual quality control and post-processing were necessary to remove segmentation errors and provide a reliable segmentation. This work motivated the development of WRF as a more robust method for $A\beta$ plaque segmentation in the presence of noise. After WRF was ready to use, the $A\beta$ plaque IHC images were then reprocessed with WRF to provide a more reliable segmentation. **Results presented here were obtained using WRF with color and contextual features.** Color features consisted in image Hue, Saturation and Value channels. Local intensity provided short-range contextual information about image intensity and was computed for each voxel as the mean of the Value channel in a small 8-connex neighborhood around the voxel. Finally, texture features were extracted by applying a family of 2D Gabor filters in the coronal plane with 4 orientations and 4 frequencies as described in section 2.4.

A ground-truth dataset was constructed by extracting a set of 10 representative small 100×100 pixels image patches from $A\beta$ IHC volumes and subsequently manually segmenting them into 3 classes: background, non-stained tissue and $A\beta$ plaque. In the learning step, 100 classification decision trees were constructed using bootstrap samples of the original learning set as in the Random Forest algorithm [72] with additional weights to compensate for class imbalance. The weights were tuned by leave-one-image-out cross-validation as described previously (section 2.4). In the classification step, each voxel was assigned to a class by a weighted majority voting of the classification trees. Each $A\beta$ plaque IHC volume was fully segmented and a binary volume with segmented $A\beta$ plaques was generated for each mouse brain (Figure 4.6c).

Spatial normalization and heatmap generation

High-resolution segmented volumes were all put into the same spatial reference by registering them to the anatomical template (Figure 4.8a). As each segmented volume is in the same referential as its corresponding block-face photography volume, the registration was estimated between each block-face photography volume and the anatomical template using the aforementioned 3D registration approach and then the transformation was applied to each segmented volume.

Finally, $A\beta$ load heat maps were generated by successively applying a Gaussian

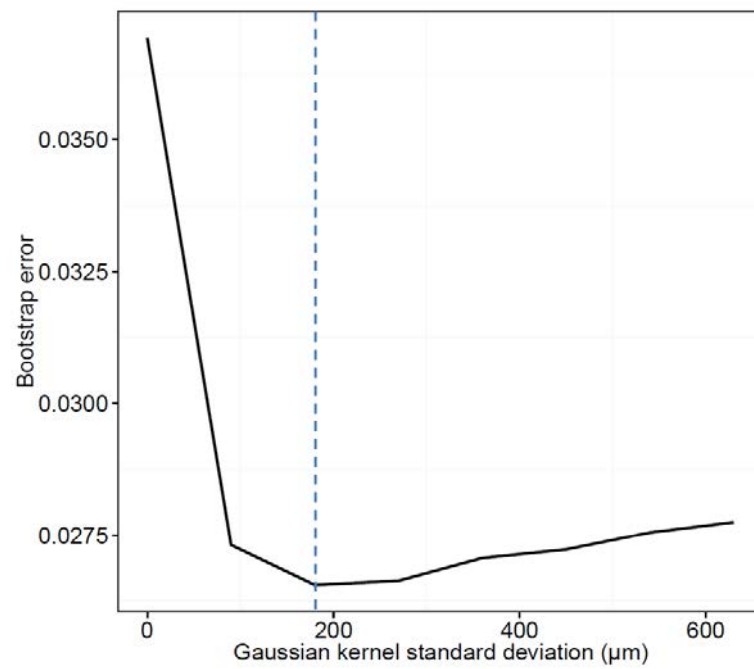


Figure 4.7: Gaussian kernel standard deviation selection through bootstrap error minimization. The error was calculated using 500 bootstrap samples, separately for $APP_{Swe,Ind-ADAM30}$ mice and $APP_{Swe,Ind-Cre-ADAM30}$ mice and then averaged over the groups.

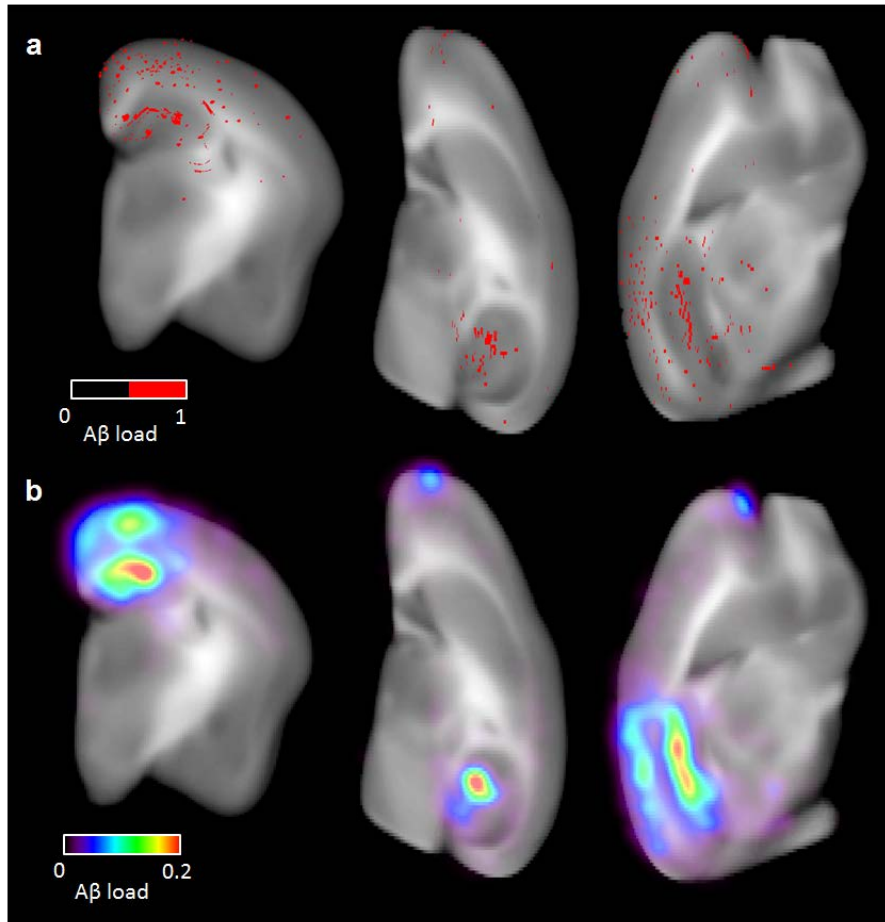


Figure 4.8: Heat map generation. (a) An $APP_{Swe,Ind}\text{-Cre-ADAM30}$ segmented $A\beta$ plaque volume and its associated heat map volume (b) superimposed with the anatomical template. From left to right: coronal, axial and sagittal views.

kernel smoothing and a binning operation. The standard deviation was determined using the bootstrap error as described in section 3.2.2. Figure 4.7 shows how the bootstrap error varies with increasing Gaussian kernel standard deviation. The minimum was detected at $180\ \mu\text{m}$. The $A\beta$ plaque segmented volumes have a voxel-size of $5 \times 5 \times 90\ \mu\text{m}^3$ and a single $A\beta$ plaque diameter can reach a few dozens of micrometers. Therefore, we chose a window size of $18 \times 18 \times 1$ which provided low-resolution volumes with an isotropic resolution of $90\ \mu\text{m}^3$. Figure 4.8 shows an $A\beta$ load heat map for an $APP_{Swe,Ind}\text{-Cre-ADAM30}$ mouse.

ROI	APP _{Swe,Ind} -ADAM30	APP _{Swe,Ind} -Cre-ADAM30
Cerebral cortex	0.51 \pm 0.46	0.27 \pm 0.09
Hippocampal region	2.63* \pm 0.58	2.08 \pm 0.42

Table 4.2: Comparative statistics between APP_{Swe,Ind}-ADAM30 and APP_{Swe,Ind}-Cre-ADAM30 using the atlas-based analysis. Data is shown as mean A β load \pm SD. * $p < 0.05$, APP_{Swe,Ind}-ADAM30 mice versus APP_{Swe,Ind}-Cre-ADAM30 mice (t-test).

4.4.3 ADAM30 effect on A β pathology

Ontology-based analysis

The MICE brain atlas was registered on the anatomical template following the protocol described in section 3.1.2. This allowed to globally measure the A β load on each heat map volume in two ROIs: the cerebral cortex and the hippocampal region where A β plaques are most frequently observed. The A β load was then compared between APP_{Swe,Ind}-Cre-ADAM30 mice and APP_{Swe,Ind}-ADAM30 mice in these two ROIs (Table 4.2). In APP_{Swe,Ind}-Cre-ADAM30 mice, the A β load was significantly reduced in the hippocampal region (Students t-test, $p < 0.05$) and a weak trend towards a reduction was detected in the cerebral cortex (Students t-test, $p = 0.14$).

Clusters detection and identification

A voxel-wise Student's t-test was computed to compare the A β load between group of individuals at each voxel of the brain and the resulting p-value map was thresholded at a level of $p < 0.05$. Correction for multiple comparisons was completed using cluster-based inference. Cluster-level correction for multiple comparison was preferred to the Bonferroni procedure or the FDR procedure because those later directly depend on the number of voxels in the image and, therefore, the result could be affected by the binning parameter.

A cluster-mass distribution under the null hypothesis was constructed by performing a 100 permutations on the individuals and recording the mass of the largest cluster from each permutation. Clusters with a higher mass than a threshold determined from the null-hypothesis distribution at $p < 0.05$ were considered as statistically significant (Figure 4.9a).

We did not detect any cluster of higher A β load in APP_{Swe,Ind}-Cre-ADAM30 mice compared to APP_{Swe,Ind}-ADAM30 mice. Two-clusters were found to be significant and indicated a lower A β load in APP_{Swe,Ind}-Cre-ADAM30 mice compared

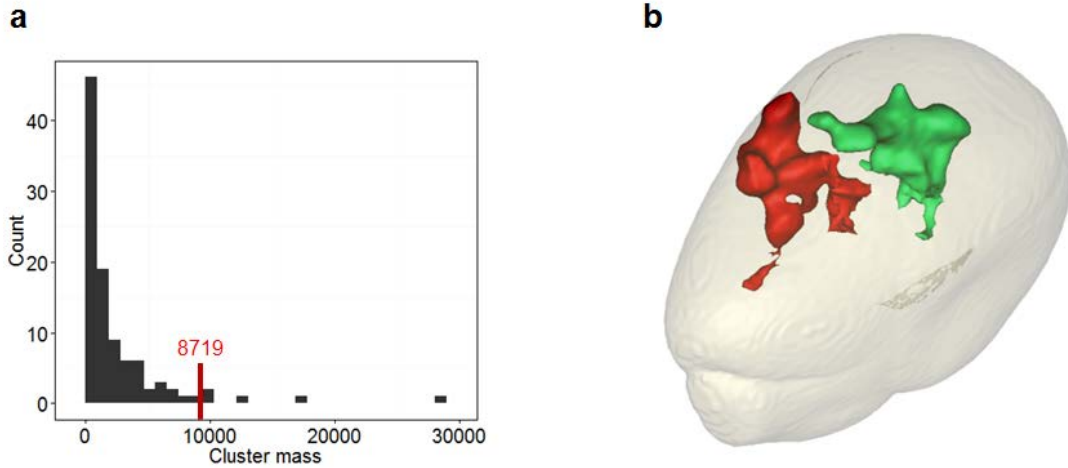


Figure 4.9: Heat map generation. (a) The cluster-mass distribution under the null hypothesis generated from random permutations. (b) 3D rendering of the 2 clusters of lower $A\beta$ load in $APP_{Swe,Ind}$ -Cre-ADAM30 mice compared to $APP_{Swe,Ind}$ -ADAM30.

Id	Localization	$APP_{Swe,Ind}$ -ADAM30	$APP_{Swe,Ind}$ -Cre-ADAM30
1	RSpC, CgC, LSN	3.80 ± 0.89	2.49 ± 0.30
2	Dentate gyrus	5.18 ± 1.05	3.37 ± 0.07

Table 4.3: Clusters descriptive statistics. Data is shown as mean $A\beta$ load \pm SD.

to $APP_{Swe,Ind}$ -ADAM30 mice which confirms the hypothesis that ADAM30 over-expression reduces the $A\beta$ load (Table 4.3).

The registered digital atlas could be used to automatically assign clusters into different regions of the brain (Figure 4.10). The first cluster was identified in the cerebral cortex and in the lateral septal nucleus (Figure 4.10a,b) while the second cluster was localized in the hippocampal region (Figure 4.10c-e). While the atlas registration can pinpoint major regions of interest, small registration errors can hinder to localize the cluster in small regions of the brain. A precise identification of the sub-regions that were involved in the cerebral cortex and the hippocampal region was carried-out manually by inspecting the cluster localization and referring to the Paxinos mouse brain atlas as an anatomical reference [99]. In the cerebral cortex, we could identify the cluster in the cingulate cortex areas 1 and 2 and the retrosplenial agranular cortex. In the hippocampal region we could identify the the dentate gyrus.

Interestingly, the cingulate and the retrosplenial areas of the cerebral cortex

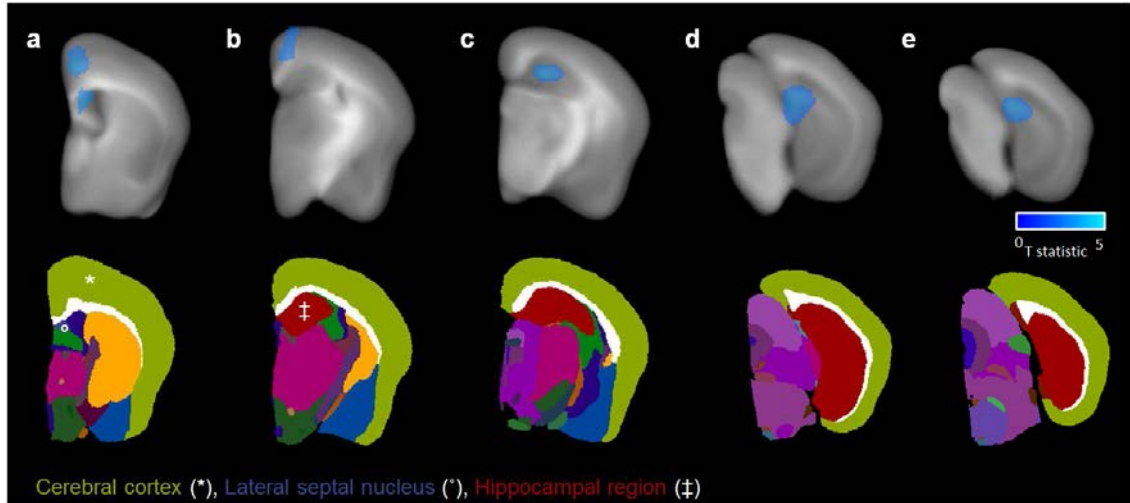


Figure 4.10: Clusters anatomical localization. $A\beta$ load is lower in $APP_{Swe,Ind}$ -Cre-ADAM30 mice in clusters localized in (a) the retro-splenial cortex, the lateral septal nucleus, (b) the cingulate cortex and (c-e) the dentate gyrus.

are primarily involved in cognitive and memory function and the dentate gyrus is responsible for spatial memory [100, 101]. In Alzheimer's disease, these areas are among the first ones to undergo functional alterations [102, 103] which indicates that the $A\beta$ lowering effect of ADAM30 involves regions that are key to the pathology of Alzheimer's disease. Furthermore, these regions are tightly connected. Indeed, axonal tracing studies have shown that the dentate gyrus projects to the lateral septal nucleus which itself projects to the cingulate cortex while the retrosplenial cortex and the cingulate cortex have reciprocal connections [104, 105]. Figure 4.11 shows that these connections are apparent in the Allen Brain connectivity atlas [105]. In $APP_{Swe,Ind}$ mice, the molecular layer of the dentate gyrus seems to be the first region that is affected by $A\beta$ plaque deposition [98]. As $A\beta$ pathology spreads along functional networks via axonal transport and seeding of $A\beta$ peptide oligomers [106], this raises an interesting question about how ADAM30 reduces $A\beta$ load. The $A\beta$ -lowering effect of ADAM30 over-expression could be explained by a local and independent effect in all the affected regions but it is also possible that ADAM30 have a unique local effect which would then result in a diminished spreading of the $A\beta$ pathology in functionally connected areas and an indirect long-range $A\beta$ -lowering effect. More investigations on ADAM30 mechanism of action will be needed to settle this question.

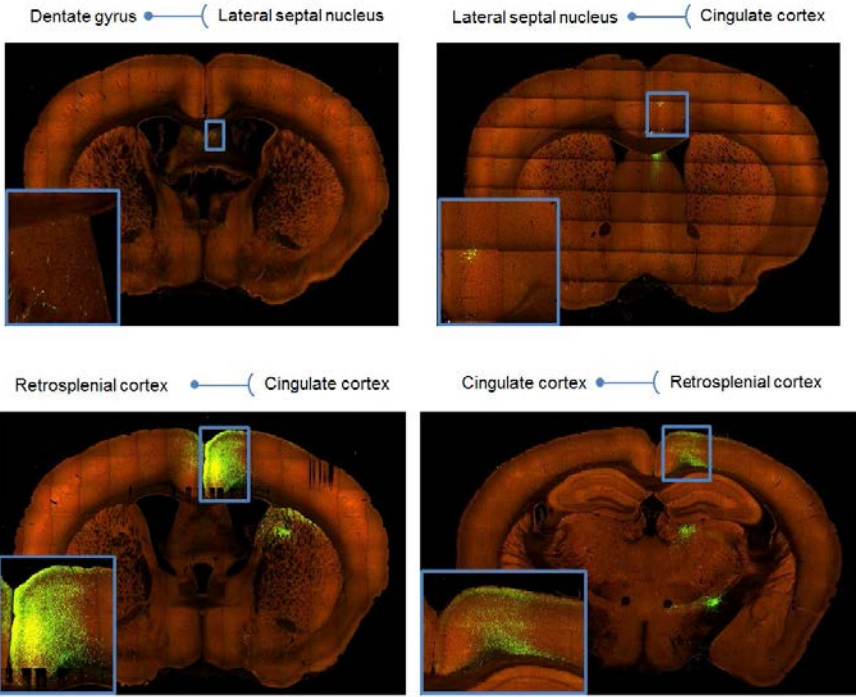


Figure 4.11: Axon-tracing between the dentate gyrus, lateral septal nucleus, retrosplenial cortex and cingulate cortex. Images show that axons stemming from a particular region are present in the green labeled regions. Images are taken from the Allen Mouse Brain Connectivity atlas (<http://connectivity.brain-map.org>).

Investigation of A β plaque size and number

After detecting clusters of significantly reduced A β load, we investigated if these differences were due to a difference in the number and/or the size of A β plaques between the groups. An A β plaque was defined as a group of voxels that are connected through all their 8 neighbors in the coronal plane. For each mouse, the number of A β plaque lying within the clusters were extracted as well as the surfaces of each A β plaque. Within clusters A β plaque number difference was tested with a Student's t-test. Within clusters A β plaque surface difference was assessed with a hierarchical linear model with mouse as a random factor and group as a fixed factor. As the A β plaques surface distribution seemed to follow a log-normal distribution, we used a Poisson generalized linear model.

Figure 4.12a shows that the A β plaque number is significantly reduced in the cortical cluster in APP_{Swe,Ind}-Cre-ADAM30 mice (48 % drop in the mean number of A β plaques, Student's t-test, $p < 0.001$) and that it remains similar in the hippocampal cluster for both groups (6% drop in the mean number of A β plaques in APP_{Swe,Ind}-Cre-ADAM30 mice, Student's t-test, $p = 0.3$). Inversely, A β plaques have a reduced surface in the hippocampal cluster in APP_{Swe,Ind}-Cre-ADAM30 mice (hierarchical linear model, $p = 0.004$) but we did not see any significant difference in the cortical cluster (hierarchical linear model, $p = 0.55$, Figure 4.12b). Figure 4.12c shows zooms of the cingulate cortex and the dentate gyrus of representative APP_{Swe,Ind}-ADAM30 and APP_{Swe,Ind}-Cre-ADAM30 mice. A β plaque number reduction in APP_{Swe,Ind}-Cre-ADAM30 mice is clearly apparent in the cingulate cortex but the few A β plaques observed in the APP_{Swe,Ind}-Cre-ADAM30 mouse are rather large. On the other hand, in the dentate gyrus, an almost continuous band of A β plaque is apparent in the APP_{Swe,Ind}-ADAM30 mouse while it seems thinner and more dislocated in the APP_{Swe,Ind}-Cre-ADAM30 mouse.

4.4.4 Discussion

In this study, voxel-wise analysis enabled to detect local A β lowering effects of ADAM30 within the cerebral cortex and the hippocampal region. These differences could be precisely located in the cingulate cortex, the retrosplenial cortex, the lateral spetal nucleus and the dentate gyrus. Notably, **the cortical cluster and the hippocampal cluster only span over, respectively, 1.8 % and 7.1 % of the cerebral cortex and the hippocampal region.** Therefore, the difficulty of the atlas-based analysis to detect changes between groups could

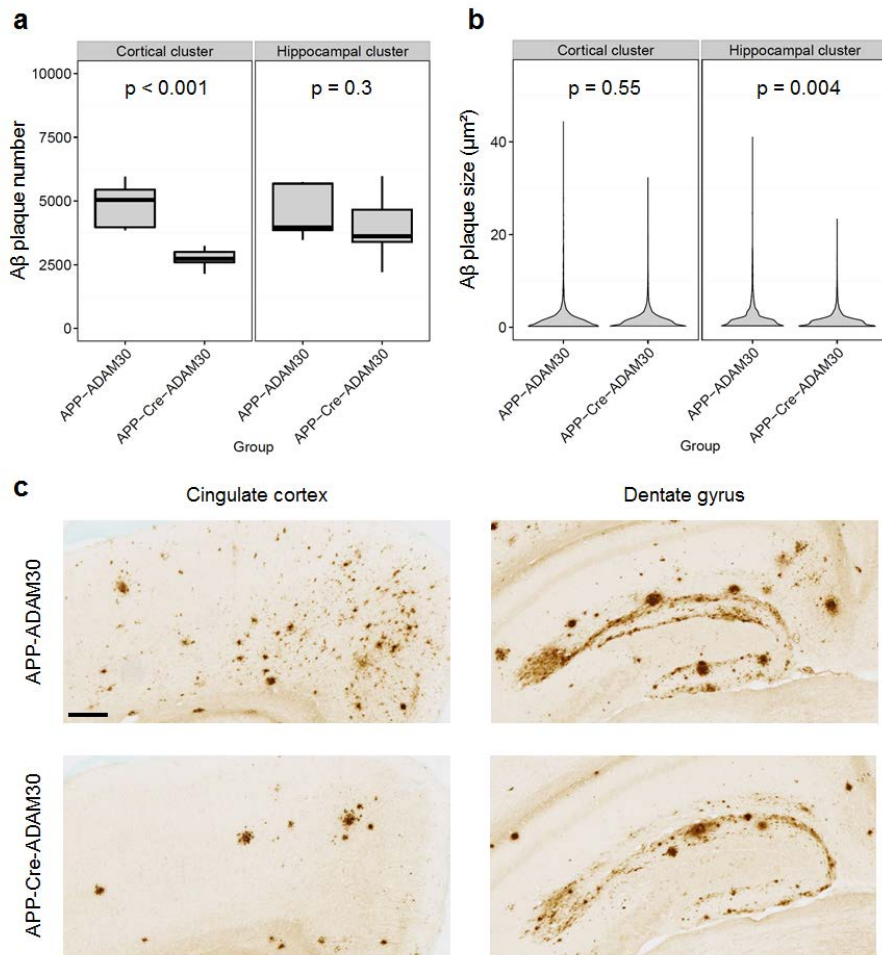


Figure 4.12: Comparisons of $A\beta$ plaque number and surface between $APP_{Swe,Ind}$ -ADAM30 and $APP_{Swe,Ind}$ -Cre-ADAM30 mice. (a) Boxplot with $A\beta$ plaque number within the cortical and the hippocampal cluster. (b) Violin plot showing the distribution of $A\beta$ plaques surface within the cortical and the hippocampal cluster. (c) Zooms in 6E10 stained-tissue section images in the cingulate cortex and the dentate gyrus for both groups (Scale bar: 200 μ m).

be explained by the fact that spatially restricted differences get more diffuse when performing measures over big regions of interest. Classically, quantification of the amount of a marker in optical microscopy studies relies on the delineation of regions of interest and measurement of a global marker quantity. This hampers the detection of spatially restricted changes within regions of interest. On the other hand, if changes between groups are distributed over entire regions, the region-based analysis could be more powerful than the voxel-wise approach. Both approaches are advantageous in different cases which suggest that using them in combination could be the best way to analyze differences between groups.

While clusters were detected at low spatial resolution, information from high-resolution imaging could be used to further interpret the effect of ADAM30 within the clusters. The lower number of A β plaques in the cingulate and retrosplenial cortices of APP_{Swe,Ind}-Cre-ADAM30 mice indicates that ADAM30 can prevent the formation of new A β plaques. Nonetheless, A β plaques have similar sizes in both groups which indicates that once seeded, A β plaque growth is not altered by ADAM30 over-expression. In the dentate gyrus, the mean A β plaque surface is diminished by ADAM30 over-expression. The lower A β plaque surface indicates that ADAM30 over-expression could slow the A β plaque growth in the dentate gyrus. However, A β plaques are very clustered in the dentate gyrus which makes it hard to study them individually. Contrary to cells which have their membrane separating them from neighboring cells, A β plaques are pathological aggregates without a defined structure. Several A β plaques in close proximity can grow until they form a single structure. Thus, studying the A β plaque size and number in the dentate gyrus is inherently difficult and a definitive conclusion about the effect of ADAM30 over-expression on individual A β plaques formation and growth would require additional experiments.

Chapter 5

Towards multimodal and multiscale analysis

In the previous chapter, quantitative 3D histopathology analysis was illustrated on widely studied mouse models of Alzheimer's disease to characterize $A\beta$ load spatial distribution and infer differences between groups of animals at the whole-brain level. Several perspectives arise at this point to extend the scope of 3D histopathology applications (Figure 5.1).

First, 3D histopathology can be used for ***in vivo* imaging validation purpose**. Recently, a number of PET radiotracers and MRI contrast agents have been developed to visualize $A\beta$ plaques *in vivo*. Three of them have been approved for clinical use in Europe to assist clinicians for the diagnosis of Alzheimer's disease when patients present cognitive decline. A key step during the development of *in vivo* imaging contrast agents is to validate the specificity and sensibility of the signal measured *in vivo*. As histology is the gold standard to highlight tissue markers, it is commonly used as a ground-truth during preclinical development of imaging contrast agents in order to ensure that the signal detected *in vivo* corresponds to tissue pathology of interest. However, as histological processing relies on tissue sectioning, spatial correlation of histopathological 2D information with *in vivo* 3D imaging modalities such as MRI and PET is arduous. This task is usually performed by manually registering 2D section images to 3D images. In practice, manual 2D to 3D image registration is very tedious and ambiguous. In this context, 3D histopathology can substantially ease the validation of *in vivo* imaging modalities. Indeed, 3D reconstruction of histopathology images allows to recover the geometry of the brain before sectioning. Therefore registering 3D histopathology images to their corresponding *in vivo* images is much more straightforward than when using 2D histology.

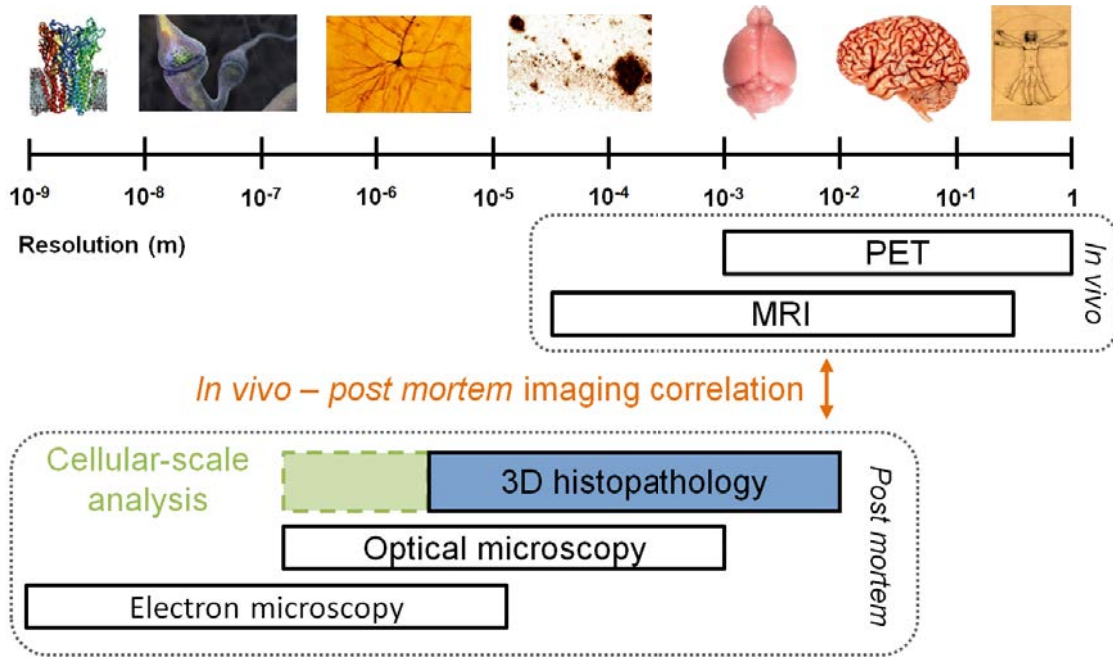


Figure 5.1: Perspectives for 3D histopathology.

Furthermore, if the *in vivo* imaging modality provides a quantitative information such as, for instance in the case of PET imaging, it could be possible to perform a correlation analysis between the signal from *in vivo* images and histology-derived heat maps in order to quantitatively assess the agreement between the two. The first section of this chapter will illustrate how 3D histopathology can be matched with *in vivo* MRI scans and how this can bring new information on the interpretation of the signal measured *in vivo*.

Another perspective is to extend 3D histopathology to **cellular markers analysis**. This raises two main challenges. First, cellular-level analysis requires sub-microscopic imaging which poses computational issues. So far in this work, $A\beta$ plaques could be reliably analyzed on images with a resolution in the range of a few μm . At a resolution of $0.44 \mu\text{m}$, which is reasonable to visualize cellular markers, a whole-brain 3D histology image corresponds to a file size of about 100 GB. Processing such a dataset requires to adapt 3D reconstruction and analysis strategies described in the previous chapters. Another challenge concerns object-level analysis of cells. So far, histopathological markers were mostly studied in term of staining occupation ratio. This occludes **object-level information** such as cell counts, sizes and shapes. Potentially, object-level analysis of cells in the whole-brain could participate in better understanding cellular disturbances in Alzheimer’s disease at a system-level. However, this implies that cells are segmented as individual objects.

Thus, a crucial step towards object-level analysis would be to enable robust individual cell segmentation in regions where cells are clustered together. The second section of this chapter will report preliminary results on the 2 aforementioned challenges. First, we will propose an adapted strategy to perform 3D histopathology with sub-microscopic resolution histology and we will apply this approach to investigate spatial relationships between neuroinflammatory cellular markers and $A\beta$ deposition. Finally, a novel approach for cell nuclei segmentation will be described and preliminary results will be shown for the individualization of clustered brain cells.

5.1 Matching quantitative 3D histopathology to *in vivo* MRI

As mentioned in section 4.3.2, study 2 included two *in vivo* imaging sessions with gadolinium contrast-enhanced MRI. This original MRI protocol was designed by Marc Dhenain’s group from MIRCen in order to visualize amyloid plaques as hypo-intense spots *in vivo* in mouse models of Alzheimer’s disease [107]. It relies on bilateral intracerebroventricular injection of gadolinium, a paramagnetic contrast agent widely used in clinical imaging. Compared to histology, this ***in vivo* imaging approach could be used to follow the effect of an anti- $A\beta$ therapy longitudinally as well as improve statistical power via repeating measurements in time on the same individuals.** Here, we employed 3D registration to match quantitative 3D histopathological information with *in vivo* MRI scans acquired prior to euthanasia. Because needles were inserted in the dorsal part of the cortex to inject the contrast agent in the cerebral ventricles, the imaging procedure provokes local bleeding. After euthanasia, areas of blood leakage to the brain parenchyma were stained on tissue sections by performing serial anti-IgG IHC staining. Thus, a first goal was to assess whether histology-derived information about blood-brain barrier disruptions could be matched with needle tracks on the *in vivo* MRI scan. A second goal was to check whether *in vivo* MRI hypo-intense signals were consistent with histology-derived $A\beta$ load patterns to validate the *in vivo* imaging protocol.

Heat maps were considered as the most appropriate form of 3D histopathology information to be registered with *in vivo* imaging. This is because they are quantitative and continuous so that, when matched with *in vivo* imaging, for each location of the *in vivo* image, the ground-truth marker quantity can be easily obtained without problems regarding the dissimilar resolutions between histology and MRI. Besides,

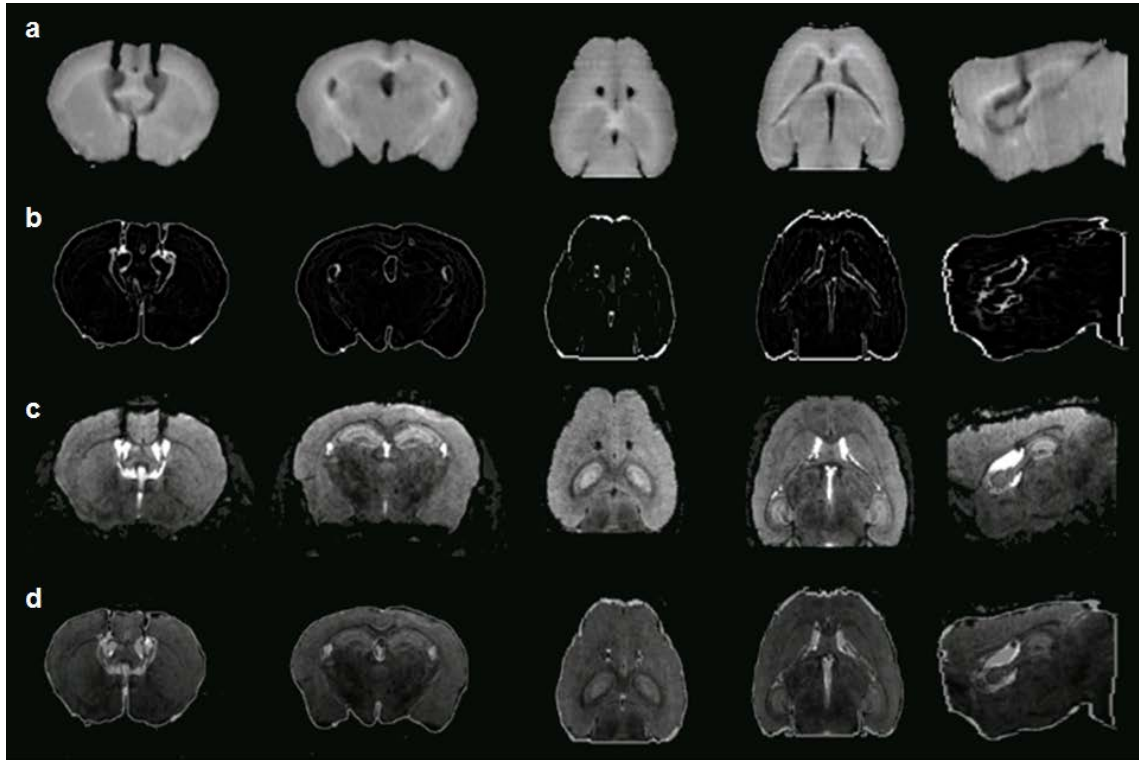


Figure 5.2: Registration of a block-face photography volume with *in vivo* MRI. From top to bottom: (a) a block-face photographic volume that have been registered in 3D with its corresponding *in vivo* MRI; (b) contours from the registered block-face photographic volume extracted with a Deriche filter; (c) *in vivo* MRI scan; (d) superimposition of *in vivo* MRI with contours from the registered block-face photographic volume. From left to right: coronal view at the level of gadolinium injection sites; coronal view at the level of the dorsal hippocampal region; dorsal axial view at the level of gadolinium injection sites; ventral axial view; sagittal view.

heat map resolution is typically much lower than this of the original reconstructed histology volume and therefore, small registration errors would not significantly alter the interpretation of the results. 3D histopathology-derived heat maps were matched to *in vivo* MRI in two steps. First, for each mouse, a transformation was computed between the block-face photography volume and the MRI scan by the successive estimation of rigid, affine and non-linear transformations using the same protocol as in section 3.1.2. Then, these transformations were applied to each heat map to match the corresponding MRI scan. Registration quality was visually validated by superimposing contours of registered block-face photography volumes on *in vivo* MRI volumes (Figure 5.2). Interestingly, the registration worked well even without pre-processing the MRI scan to remove the skull and muscles surrounding the brain.

Staining from IgG IHC and A β IHC was segmented using the BioVision algorithm and brain-wide heat maps were generated by successively filtering the segmented volumes with a Gaussian kernel and by binning the smoothed volume which provided heat maps with an isotropic resolution of $125 \times 125 \times 125 \mu\text{m}^3$. Finally, heat maps for blood-brain-barrier leakage and A β deposition were warped on their corresponding MRI scan (Figure 5.3a-d). Massive IgG leakage was observed on anti-IgG heat maps and colocalized with injection sites spotted on MRI (Figure 5.3a). In addition, one APP/PS1 mouse was found with brain-wide blood-brain barrier disruptions (Figure 5.3b) which were not seen on MRI. No A β deposition was detected in MRI and in A β load heat maps of PS1 mice (Figure 5.3e). In contrast, hypo-intense spots were observed on MRI in the cerebral cortex of APP/PS1 mice with a distribution corresponding to that of A β load heat maps (Figure 5.3f). This confirms previous studies showing that A β aggregates can be detected by contrast-enhanced MRI in the cerebral cortex [107]. However, in the thalamus, where A β deposition was important on IHC, the MRI hypo-intense signal was very diffuse and did not resemble to the hypo-intense spots of the cerebral cortex. This discrepancy could be explained by the fact that MRI is not actually sensitive to A β deposits, but rather to the iron content of A β plaques. In this case, the discrepancy between regions could be explained by various levels of iron in A β deposits depending on the region. Furthermore, the iron content of the thalamus has been shown to be increased in Alzheimer’s disease which could explain the diffuse hypo-intense pattern in this region [108]. An interesting perspective would be to highlight areas of high iron content with Pearl’s histology and to check whether the iron content pattern matches the MRI hypo-intense signals better than the A β load pattern. Here,

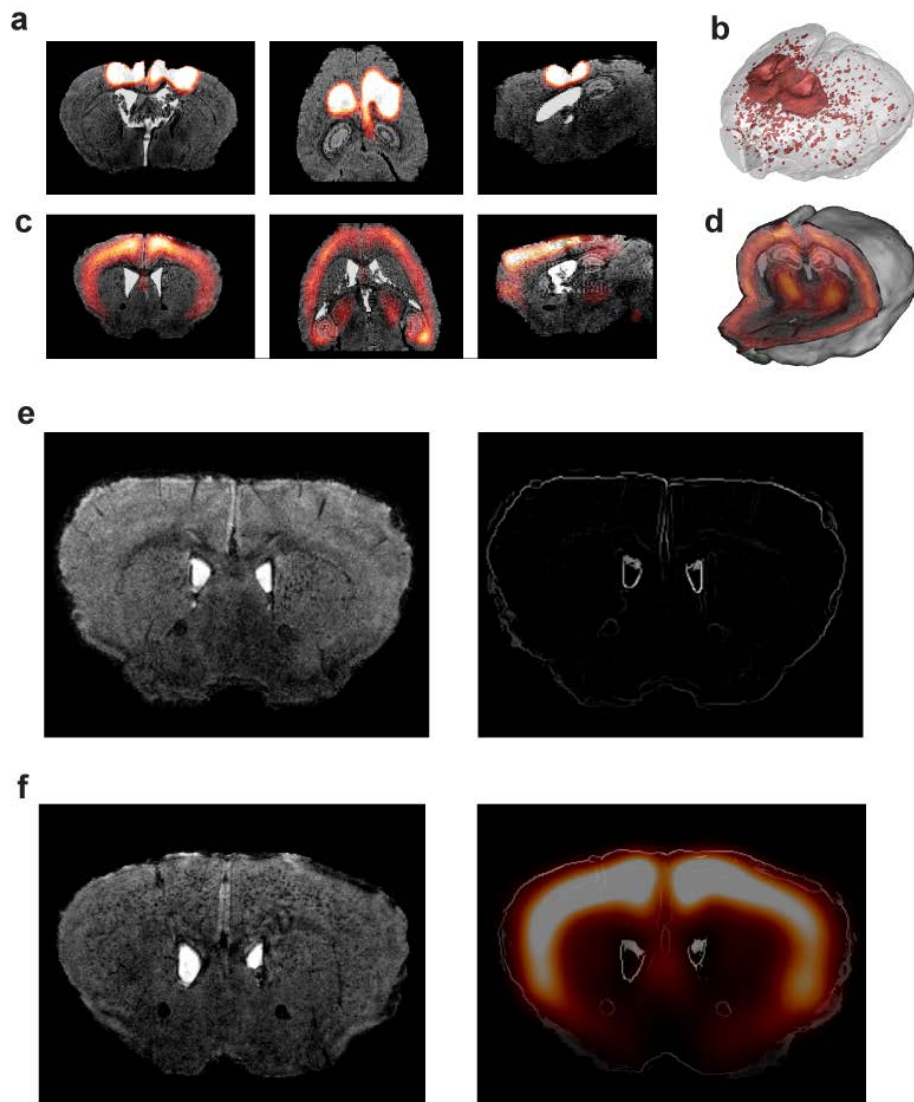


Figure 5.3: *In vivo* – *post mortem* imaging comparison. (a) Blood-brain-barrier disruption heat map in coronal (top), axial (middle) and sagittal (bottom) views. (b) 3D rendering of blood-brain-barrier disruptions detected with 3D histopathology in one APP/PS1-DM4 mouse presenting this particular phenotype. (c) A β deposition heat map in coronal (top), axial (middle) and sagittal (bottom) views. (d) 3D rendering of A β deposition heat map with *in vivo* MRI. (e) A PS1 mouse that does not display A β deposition neither on *in vivo* MRI (left) nor on A β deposition heat map (right) and (f) an APP/PS1 mouse displaying hypo-intense spots in the cerebral cortex (left) with a similar distribution to the A β deposition heat map (right). A β deposition heat maps have been superimposed with *in vivo* MRI contours to allow better visualization.

the concordance between *in vivo* contrast-enhanced MRI and histology-derived $A\beta$ deposition heat maps was assessed visually. Segmentation algorithms are currently under development in order to detect hypo-intense spots on *in vivo* MRI scans and to correlate these measures with $A\beta$ deposition using 3D heat maps as a reference.

5.2 3D whole-brain histopathology at the cellular-scale

5.2.1 Spatial correlation between cellular markers at the whole-brain level

One of the most fundamental question in neuroscience is to understand how different cell-types interact and to evaluate the impact of pathology on these interactions. Cells communicate via *paracrine signalling*, that is, they interact locally with their neighboring cells via releasing molecules in the extra-cellular compartment. Thus, functional relationship is correlated with spatial relationship. While histology cannot directly be used to assess functional relationships between cells, it is a very powerful tool to assess the spatial relationships between them. Here, we aimed to use 3D histopathology to **quantitatively assess the spatial relationship between several markers at the whole-brain level.**

Previously, in study 2, the $A\beta$ deposition and blood-brain barrier disruption were studied at the whole-brain level. In addition to these markers, three histological series were generated but were not analyzed yet. These sets consist of:

- Nissl stained series (Nissl staining highlights cells non-specifically),
- microglial stained series (Iba-1 IHC, microglia are the inflammatory cells of the brain and they are involved in Alzheimer’s disease in ways that are not fully understood, see section 1.2.2),
- phagocytic cells stained series (CD-68 IHC, this staining highlights cells which are actively involved in scavenging deleterious objects in the brain).

These three markers were considered for a correlation analysis. Besides, we also considered the $A\beta$ deposition stained series but the blood-brain barrier disruption marker series was left aside. Indeed, as the contrast agent injection in the brain ventricles clearly affected the spatial distribution of blood brain barrier disruption, it would not be relevant to correlate this marker with the remaining ones. Given the

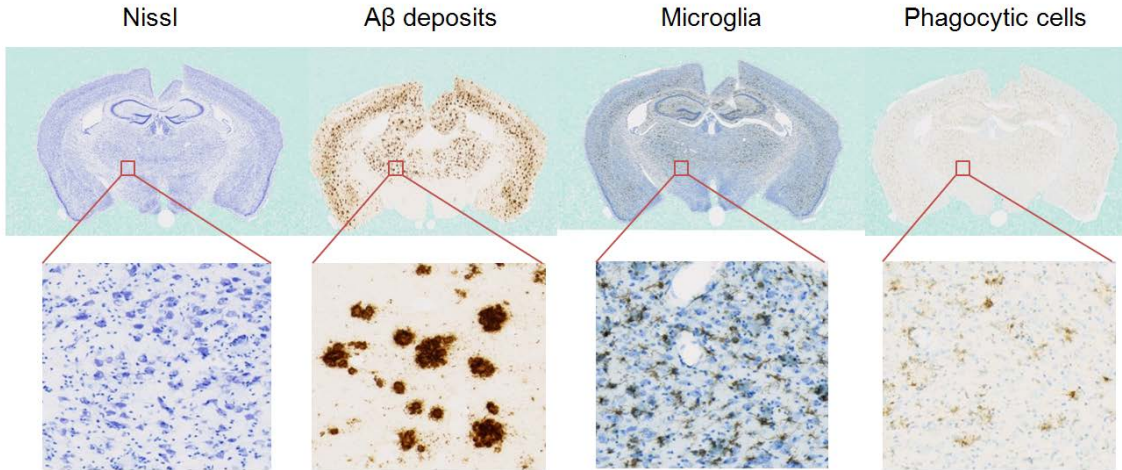


Figure 5.4: Histological coronal section images at a lateral resolution of $0.44 \mu\text{m}$. Left: Nissl staining in blue; middle-left: $A\beta$ deposits in brown (6E10 IHC); middle-right: microglia in black (Iba-1 IHC) and Nissl counterstaining in blue; right: phagocytic cells in brown (CD68 IHC) and light Nissl counterstaining in blue.

Mouse whole-brain images	XYZ resolution (μm^3)	Number of voxels	File size (GB)
<i>In vivo</i> MRI	$30 \times 30 \times 30$	$\approx 10^7$	≈ 0.02
Block-face photography	$30 \times 30 \times 125$	$\approx 10^7$	≈ 0.02
$A\beta$ plaque 3D histopathology	$5 \times 5 \times 125$	$\approx 10^8$	≈ 1
Cellular-scale 3D histopathology	$0.44 \times 0.44 \times 125$	$\approx 10^{10}$	≈ 100

Table 5.1: Image resolution and size for a mouse brain with different imaging modalities.

4 selected markers, our goal was to assess whether we could find pairs such that there is a strong statistical dependence between the amount of the 2 markers throughout the brain.

One control-treated APP/PS1 mouse was chosen to correlate the four markers. Each series of sections was digitized at a resolution of $0.44 \mu\text{m}$ with a Zeiss Axio ScanZ.1 whole-slide imaging microscope. Figure 5.4 displays a tissue section image for each marker. Some adaptations were needed to analyze this dataset in 3D. Previously, when analyzing the $A\beta$ load at a lateral resolution of $5 \mu\text{m}$, a typical whole-brain image contained about 10^8 voxels which corresponds to about 1GB. This dataset can be easily loaded and processed on a desktop computer. However, with a lateral resolution of $0.44 \mu\text{m}$, images of the same tissue sections correspond

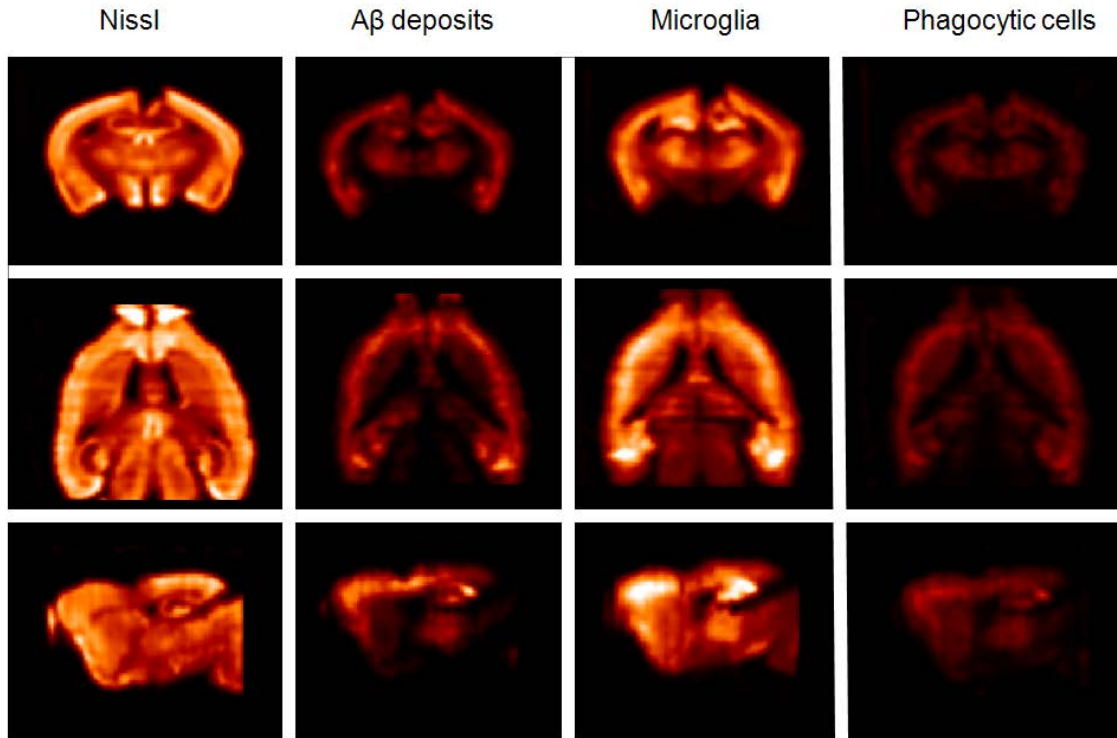


Figure 5.5: Pathological and cellular markers heat maps in multiple views. Top: coronal view; middle: axial view; bottom: sagittal view. From left to right: Nissl-staining heatmap, $A\beta$ IHC deposition heatmap, microglia IHC heatmap, phagocytic cells IHC heatmap.

to a dataset of about 100GB (Table 5.1). High-resolution histology images could be rapidly segmented using the BioVision algorithm by processing large chunks of whole-slide images in parallel on a cluster computer. To reconstruct the series in 3D, original color histology images and segmented images were first binned down to a lateral resolution of $125 \mu\text{m}$. The binned histology images were then registered to their corresponding block-face photography to provide coherent 3D volumes for each series. Estimated transformations between histology and block-face photography were then applied to the binned segmented images. Finally, the binned segmented histology volumes were smoothed with a Gaussian kernel. Figure 5.5 shows the resulting heat maps for each marker.

A total of about 150000 voxel values spanning the entire brain were extracted for each marker. As heat map volumes were all in the same spatial referential, we correlated voxel values between markers in order to assess their degree of spatial dependence (Figure 5.6). Interestingly, among all between-marker correlations, $A\beta$ deposits and phagocytic cells showed the strongest association (Spearman's $\rho =$

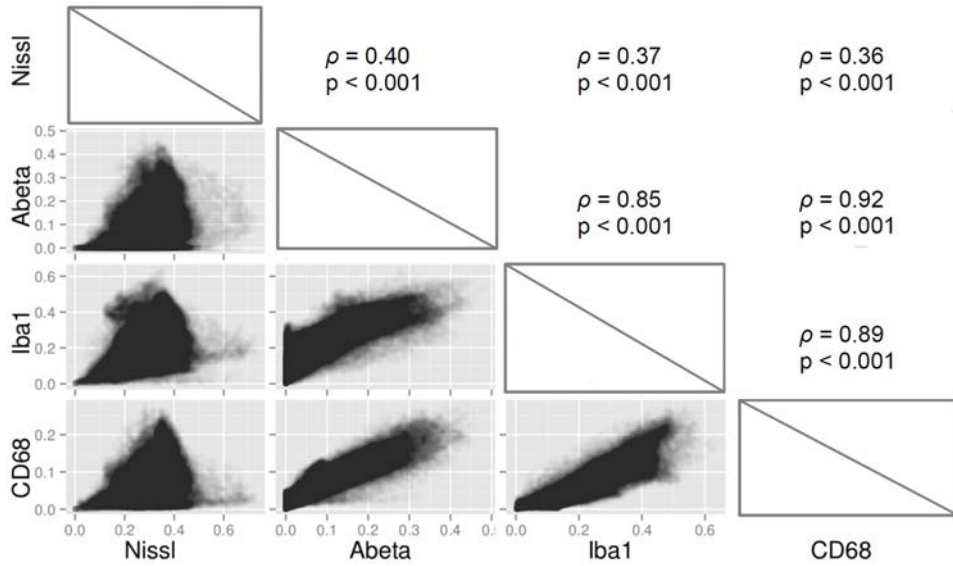


Figure 5.6: Multiple marker spatial correlation. Spearman’s rank correlations between markers are shown in the upper panels while corresponding scatter plots are shown in the lower panels. Scatter plots data points have 10% opacity to allow for better visualization.

0.92, $p < 0.001$). This indicates that $A\beta$ deposition is tightly and widely associated with cells presenting a phagocytic phenotype. Nissl staining only weakly correlated with the remaining markers (Spearman’s $\rho = 0.40$, $p < 0.001$ versus $A\beta$ deposition, Spearman’s $\rho = 0.37$, $p < 0.001$ versus microglial cells, Spearman’s $\rho = 0.36$, $p < 0.001$ versus phagocytic cells). Microglial cells strongly correlated with both $A\beta$ deposition (Spearman’s $\rho = 0.85$, $p < 0.001$) and phagocytic cells (Spearman’s $\rho = 0.89$, $p < 0.001$) which is consistent with the fact that microglial cells are involved in $A\beta$ plaque phagocytosis. The correlation between $A\beta$ deposition and neuroinflammatory markers has been well-documented by classical 2D histology investigations [52] and our results confirm that this interaction occurs at the whole-brain level.

Correlation analysis using the occupation ratios is a versatile approach to **screen for spatial interactions between markers**. However, the occupation ratio melts together a lot of information about the markers. First, the analysis is dependent on the heat map resolution. If spatial distributions for two markers globally correlate at a low-resolution, it is not guaranteed to hold at a finer scales. Also, the occupation ratio is blind to object-features. For instance, while our results show that $A\beta$ deposition is tightly correlated with phagocytic cells, the influence of $A\beta$ deposition on the number and/or size of these cells remains an open question. An-

alyzing object-level features at the level of the whole-brain promises to get much more insightful understanding of the interactions between cell-types and between cells and pathological markers. The next section will raise the issue of individual cell segmentation which is a prerequisite for object-level analysis and a novel method will be proposed to tackle this difficult problem.

5.2.2 A hierarchical Gaussian Mixture Model (GMM) approach for touching cells segmentation

In most of this work, quantification of histopathological markers was expressed as the relative quantity of positive staining. BioVision and Weighted Random Forests classification algorithms were used to segment histology images and detect regions of positive staining prior to quantification. While this approach may be valid for neuropathological markers, it is not sufficient to grasp the variety of phenomena that can affect cells in pathological conditions. Positive staining segmentation cannot distinguish individual cells because brain cells are often touching each other. Therefore, this approach cannot bring information about cell abnormalities such as changes in morphology, size or number. **A robust and automatic method to segment individual cells is essential in order to study those abnormalities at the level of the whole-brain in mouse models of neurodegenerative diseases.**

Individual cell segmentation is a very active field of research and a number of methods have been proposed. Most widely used techniques rely on mathematical morphology [109], the watershed algorithm [110], concavity detection [111] and the graph-cut algorithm [112]. For a recent and comprehensive review on individual cell segmentation, we refer to Irshad *et al.* [21]. Unfortunately, despite numerous publications on the subject, only few algorithms have been made available to the community. Recently, a publication comparing available methods for cell segmentation was entitled “Current automated 3D cell detection methods are not a suitable replacement for manual stereologic cell counting” which shows how difficult is this task and calls for novel approaches in this field [113]. Work is currently ongoing in our group to compare various existing methods and develop algorithms that could potentially scale to the analysis of brain whole-slide images. Here, we propose a novel method to separate touching cells based on a **hierarchical GMM clustering approach**. It relies on the assumption that the intensity values for a cell can be modeled with a bi-variate Gaussian density. Thus, it is primarily intended for cells

that are approximately ovoid and which staining intensity is approximately radial. These properties are often encountered in histology (for instance with Nissl-stained cells or NeuN IHC-stained neurons).

The advantage of using GMM is that it provides a parametric probabilistic framework which enables to evaluate the model in regard to the cell segmentation task and to adapt the model parameters to improve the segmentation. GMM was already mentioned in this work for density estimation purpose in the BioVision algorithm (section 1.1.3). Besides density estimation, GMM is a widely adopted tool for clustering because it is very efficient at detecting regions of high-density separated by regions of lower density. A parallel can be made with histology images where cells appear as intensely stained regions separated by less stained regions. If cells in an image are modeled with Gaussian densities, each pixel in the image can be associated to a particular component of the mixture yielding a segmentation with individual cells. However, the number of components has to be specified in advance in the model yet this is precisely what we want to infer. If cell staining intensity was uni-modal, a simple search for staining intensity peaks would allow to detect the number of components in the mixture. In practice, staining in-homogeneities and noise are generating spurious peaks leading to an overestimation of the number of cells. To address this issue, we propose a hierarchical approach which consists in, first, creating a **low-scale representation** of the image by convolving it with a large Gaussian kernel and then fitting a GMM on this low-scale representation using intensity peaks as initial guesses for cell localization. It can be expected that peak detection at a coarse-level will result in an underestimation of the number of cells. Thus, this process is repeated at increasingly sharper scales and, at each scale, the mixture components are locally evaluated to select the Gaussian components that best represent individual cells. The **Hellinger distance**, which reflects the overlap between 2 Gaussian distributions, is used as a criterion to select the components. This allows to discard spurious cell candidates by restricting the amount of overlap between components. The next sub-sections will describe the methodology into more details and present preliminary results for the segmentation of cells on simulated images as well as on real images of Nissl-stained cells and NeuN IHC-stained neurons.

Preprocessing

A few pre-processing operations are required before GMM can be used to segment cells on histology images. Histology color images are first converted to grey-scale

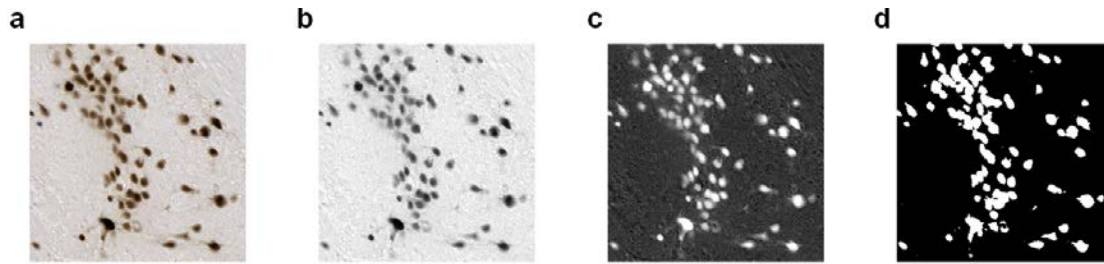


Figure 5.7: Preprocessing steps. (a) Original NeuN IHC-stained tissue section image. (b) Red channel. (c) Inverted red channel. (d) Mask of the NeuN IHC staining.

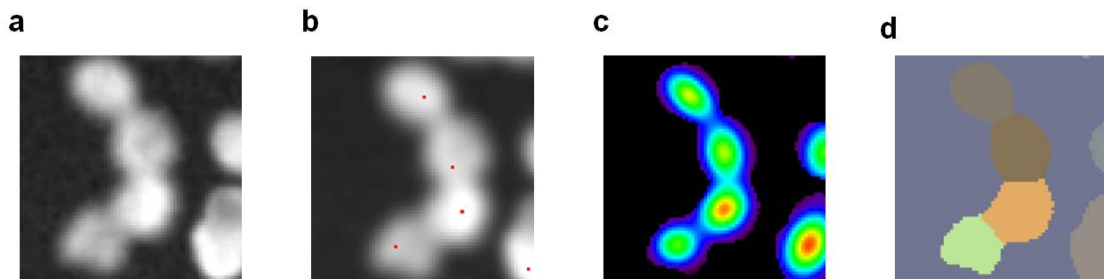


Figure 5.8: Segmentation of touching cells with Gaussian Mixture Models (GMM) clustering. (a) Original image with 4 touching cells in the center (simulated dataset downloaded from the Broad Bioimage Benchmark Collection: <http://www.broadinstitute.org/bbbc>) [114]. (b) Smoothed image after Gaussian kernel filtering with a standard deviation of 2 pixels. Maxima are shown in red. (c) Mixture components after 3 iterations of the Expectation-Minimization (EM) algorithm. (d) Clustering result with each cell shown in a different colour.

images by extracting the channel which offers the best contrast between the staining and the background (Figure 5.7a,b) and the grey-scale image is inverted so that the staining appears as light over a dark background (Figure 5.7c). Additionally, a mask of the staining is required to restrict the search for cells only in areas of the image that are considered as positive for the cell staining. The mask can be generated via any image segmentation method such as k-means, BioVision or Weighted Random Forests (Figure 5.7d).

GMM clustering

At each iteration of the hierarchical procedure, the image is first smoothed with a Gaussian kernel and local maxima are detected among the pixels that correspond to stained areas on the mask (Figure 5.8a,b). The image $I(\mathbf{x})$ is then modeled with

the following density:

$$f(\mathbf{x}) = \sum_{j=1}^s \pi_j \rho_{\boldsymbol{\mu}_j, \Sigma_j}(\mathbf{x}), \quad (5.1)$$

where π_j is the mixing coefficient of component j such that $\pi_j > 0 \forall j$ and $\sum_{j=1}^s \pi_j = 1$, s is the number of detected peaks and ρ is the density of the bi-variate normal distribution with mean vector $\boldsymbol{\mu}_j$ and co-variance matrix Σ_j . The mean vector corresponds to the coordinates of the cell gravity center and the mixing coefficient and co-variance matrix are linked to the cell-size and -shape (Figure 5.8c).

Maximum likelihood parameters are estimated using the EM algorithm. First, the EM algorithm is fed with guesses for each parameter: the mean vectors are initialized with the localization of the detected peaks, the co-variance matrices are initialized with equal variances in each direction with values broadly corresponding to the radius of a cell and null co-covariance and the mixing coefficients are initialized at $1/s$. If we suppose the existence of c_i , an unobserved label for each pixel \mathbf{x}_i which value corresponds to the membership of the pixel to a particular component, we can calculate:

$$P(c_i = j | \mathbf{x}_i) = \frac{\pi_j \rho_{\boldsymbol{\mu}_j, \Sigma_j}(\mathbf{x}_i)}{\sum_{m=1}^s \pi_m \rho_{\boldsymbol{\mu}_m, \Sigma_m}(\mathbf{x}_i)} \quad (5.2)$$

for each possible $j \in [1 - s]$. Then, we can update the model by calculating the mixing coefficient for each component:

$$\pi_j = \frac{\sum_{i=1}^n P(c_i = j | \mathbf{x}_i) I(\mathbf{x}_i)}{\sum_{i=1}^n I(\mathbf{x}_i)}, \quad (5.3)$$

as well as the weighted mean vectors and co-variance matrices:

$$\boldsymbol{\mu}_j = \sum_{i=1}^n \gamma_{i,j} \mathbf{x}_i, \quad (5.4)$$

$$\Sigma_j = \sum_{i=1}^n \gamma_{i,j} (\mathbf{x}_i - \boldsymbol{\mu}_j)(\mathbf{x}_i - \boldsymbol{\mu}_j)^T, \quad (5.5)$$

where $\gamma_{i,j}$ is the contribution of pixel \mathbf{x}_i to the component j :

$$\gamma_{i,j} = \frac{P(c_i = j | \mathbf{x}_i) I(\mathbf{x}_i)}{\pi_j \sum_{i=1}^n I(\mathbf{x}_i)}. \quad (5.6)$$

The parameters are guaranteed to converge after several iterations of the EM algorithm [115]. Finally, a segmentation can be obtained by assigning to each pixel the

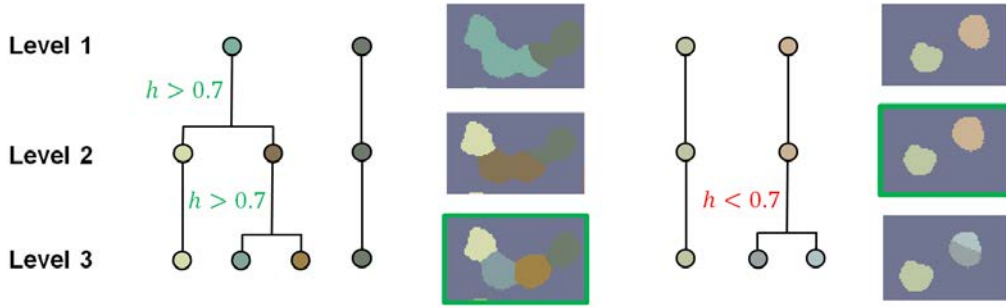


Figure 5.9: Examples of 3-level hierarchical component selection. Components are allowed to split if the Hellinger distance between the daughter components is greater to a predefined threshold of 0.7. The segmentation corresponding to selected components is displayed with a green frame. The 3 levels correspond to Gaussian kernels with a standard deviation of, respectively, 8, 4 and 2 pixels.

value corresponding to $\arg \max_{j \in [1-s]} P(c_i = j | \mathbf{x}_i)$ (Figure 5.8d).

Component number selection

We considered a top-down approach, starting from a simple model with few components and refining, if needed, the model with additional components (Figure 5.9). At the first level, the image is smoothed with a Gaussian kernel that is sufficiently large to remove all spurious peaks. At finer scales, newly generated components are linked to their parent component resulting in tree-shaped lineages. A component at scale $i + 1$ is considered to be the daughter of a component at scale i if its mean vector falls within the cluster of the parent component. At each split of the tree, pairs of daughter components are evaluated using the Hellinger distance:

$$h(p, q) = \sqrt{1 - e^{-d(p, q)}}, \quad (5.7)$$

with

$$d(p, q) = \frac{1}{8}(\boldsymbol{\mu}_p - \boldsymbol{\mu}_q)^T \bar{\Sigma}^{-1}(\boldsymbol{\mu}_p - \boldsymbol{\mu}_q) + \frac{1}{2} \log \left(\frac{|\Sigma_p + \Sigma_q|}{\sqrt{|\Sigma_p| |\Sigma_q|}} \right), \quad (5.8)$$

where $\boldsymbol{\mu}_p$, Σ_p and $|\Sigma_p|$ are respectively, the mean vector, co-variance matrix and the determinant of the co-variance matrix from component p and $\bar{\Sigma}$ refers to the mean of the two co-variance matrices.

The Hellinger distance measures how much 2 daughter components overlap. It is a symmetric distance and satisfies the property: $0 \leq h(p, q) \leq 1$. Daughter components are accepted in the final model only if the Hellinger distance between them

is greater than some predefined threshold. In the case where more than 2 daughters are found for one parent, pairwise distances are calculated and the daughters are included altogether if the minimum distance between pairs is greater than the threshold. The advantage of controlling the distance between distributions is that it is independent of the size of the cells to be detected. The threshold can be defined experimentally by the user. In addition, 2 mild criteria were added to remove spurious cells that could escape the distance criterion: detected cells should have at least some minimal size and their shape should not be too elongated. The cell-size is simply the number of pixels in the cluster corresponding to the component being evaluated and the elongation is measured using the ratio between the first and the second eigenvalue of the component. Values for these criteria should be loose enough to only remove clear outliers.

Results

Three types of images were segmented to test the proposed approach:

- Simulated microscopy cell images downloaded from the Broad Bioimage Benchmark Collection (<http://www.broadinstitute.org/bbbc>). This dataset consists of images resembling to fluorescent microscopy images of stained nuclei (Figure 5.10)
- 1000×1000 patches extracted from NeuN IHC stained tissue sections whole-slide images (Figure 5.11) .
- 1000×1000 patches extracted from Nissl-stained tissue sections whole-slide images (Figure 5.12).

Although these images look very different, using the same Hellinger distance threshold for all three datasets seemed to provide reproducible results. Throughout the experiments, three levels were considered to limit computational cost, the Hellinger distance threshold was set at 0.7 and the eigenvalues ratio was set at 10. The size of the Gaussian kernels and the minimum cell-size were chosen separately for each marker. On the simulation dataset, the hierarchical approach (Figure 5.10f) seemed to give better results than several watershed-based methods implemented in *image/fiji* (Figure 5.10b-d). As ground-truth segmentations are available for the simulation dataset, work is currently ongoing to quantitatively compare different approaches. Also, it would be useful to benchmark more diverse methods to get a better view of the respective strengths and weaknesses of available methods.

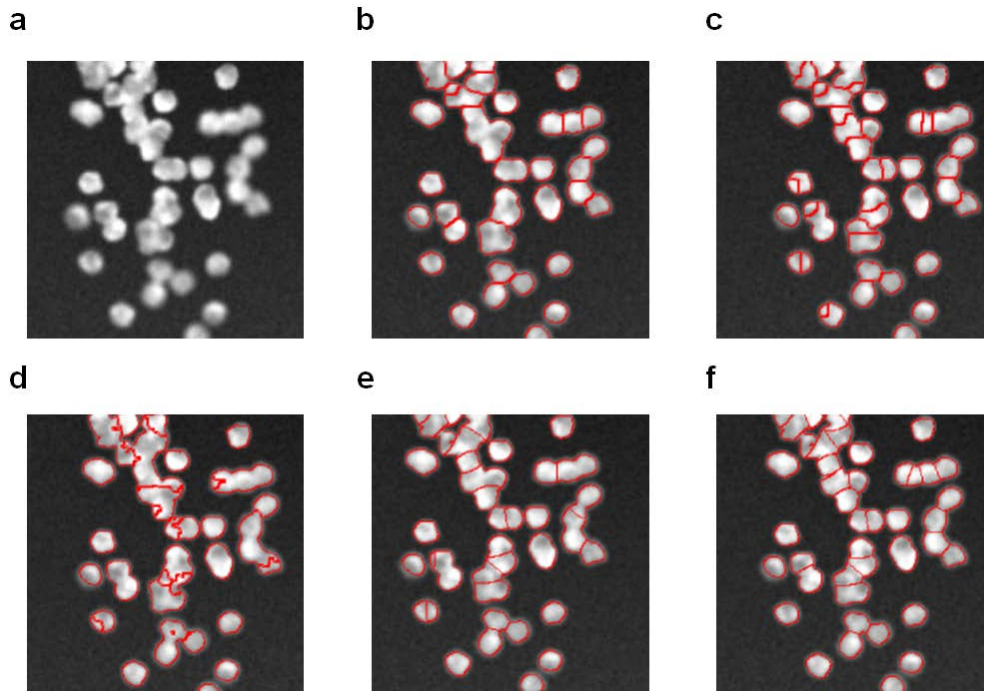


Figure 5.10: Comparison of cell boundaries detected via several methods. (a) Original image. (b) Watershed on distance map [110]. (c) Watershed on smoothed grey-scale image [116]. (d) Marker-controlled watershed. (e) Best single-scale GMM. (f) Hierarchical GMM with 3 levels (Gaussian smoothing with standard deviations of 8, 4 and 2 pixels), a minimum Hellinger distance of 0.7, a minimum cell size of 50 pixels and a maximum eigenvalues ratio of 10.

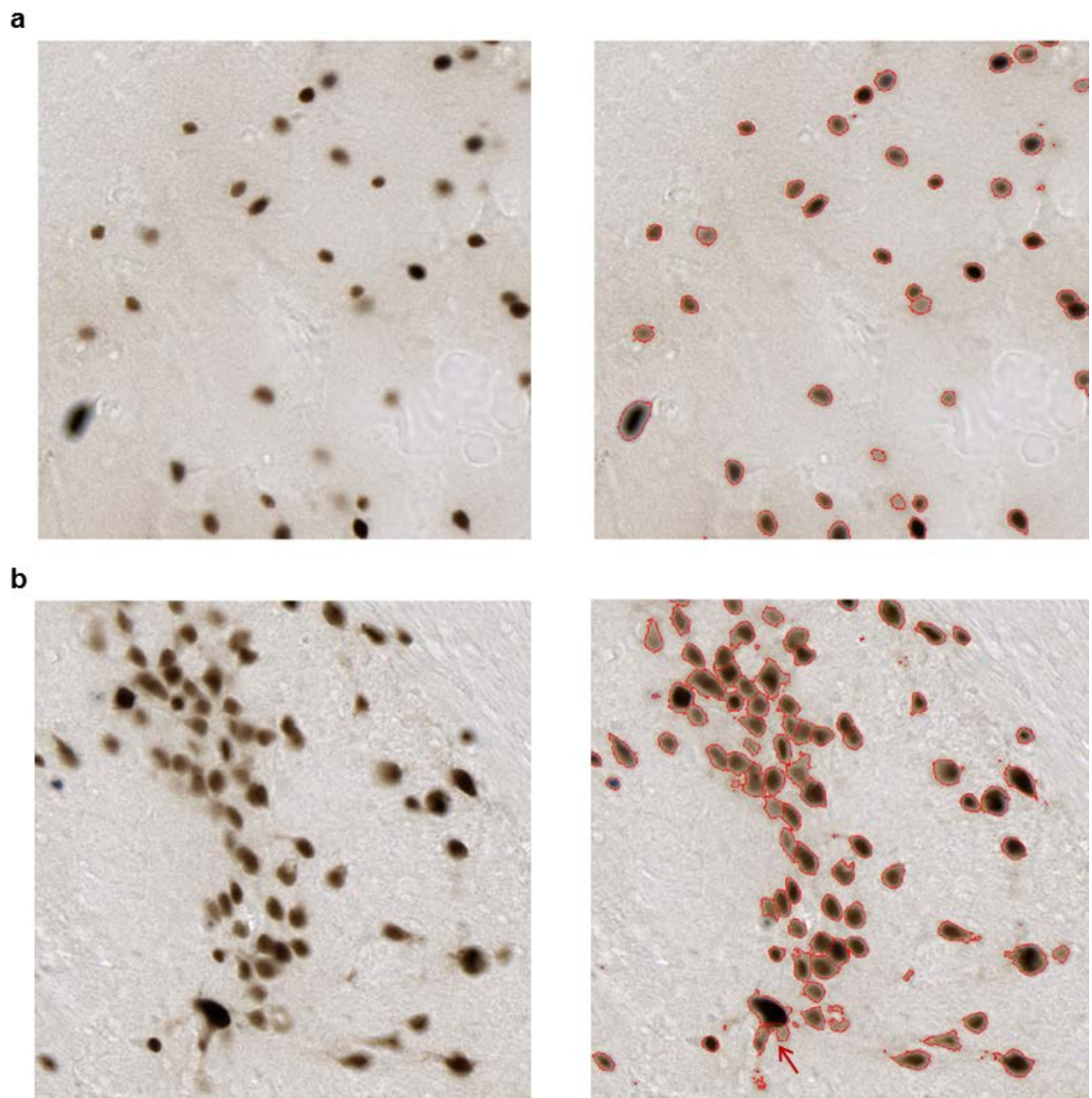


Figure 5.11: Neuron segmentation for NeuN IHC stained images with a 3-levels hierarchical GMM (Gaussian smoothing with standard deviations of 8, 4 and 2 pixels), a minimum Hellinger distance of 0.7, a minimum cell size of 500 pixels and a maximum eigenvalues ratio of 10. (a) Sparsely distributed neurons. (b) Moderately clustered neurons. The red arrow indicates an over-segmented cell.

Segmentation of NeuN IHC stained neurons is illustrated on Figure 5.11. In the case where cells are sparsely distributed, the proposed approach did not over-segment cells which is an issue often reported with watershed-based methods (Figure 5.11a). In a case of moderately clustered neurons, hierarchical GMM segmentation provided a good partition of the touching cells except for one cell which shape was not adequately modeled with a Gaussian distribution (Figure 5.11b).

More challenging cases are shown in Figure 5.12 with Nissl-stained tissue sections images. In these cases, cells are very clustered and their shapes and sizes are highly heterogeneous. Hierarchical GMM segmentation provided overall good results even when cell sizes varied a lot on the same image (Figure 5.12a). Figure 5.12b shows an interesting case. A part of the dentate gyrus is apparent on the upper left part of the image. In this region, cells are so dense that the segmentation task is very ambiguous, even for an expert. In this case, hierarchical GMM yielded a segmentation that seems to make sense but it is difficult to evaluate whether it is actually correct.

Future work could be undertaken to image very dense regions at even higher resolution and/or with multiple focal planes. This could help to resolve individual cells in very dense regions of the brain but it would also significantly add to the computational burden. In addition, work is currently ongoing in our group to (1) create ground-truth annotations for common cellular markers in order to quantitatively compare available approaches and to (2) develop parallel computing methods to scale the segmentation to whole-slide images.

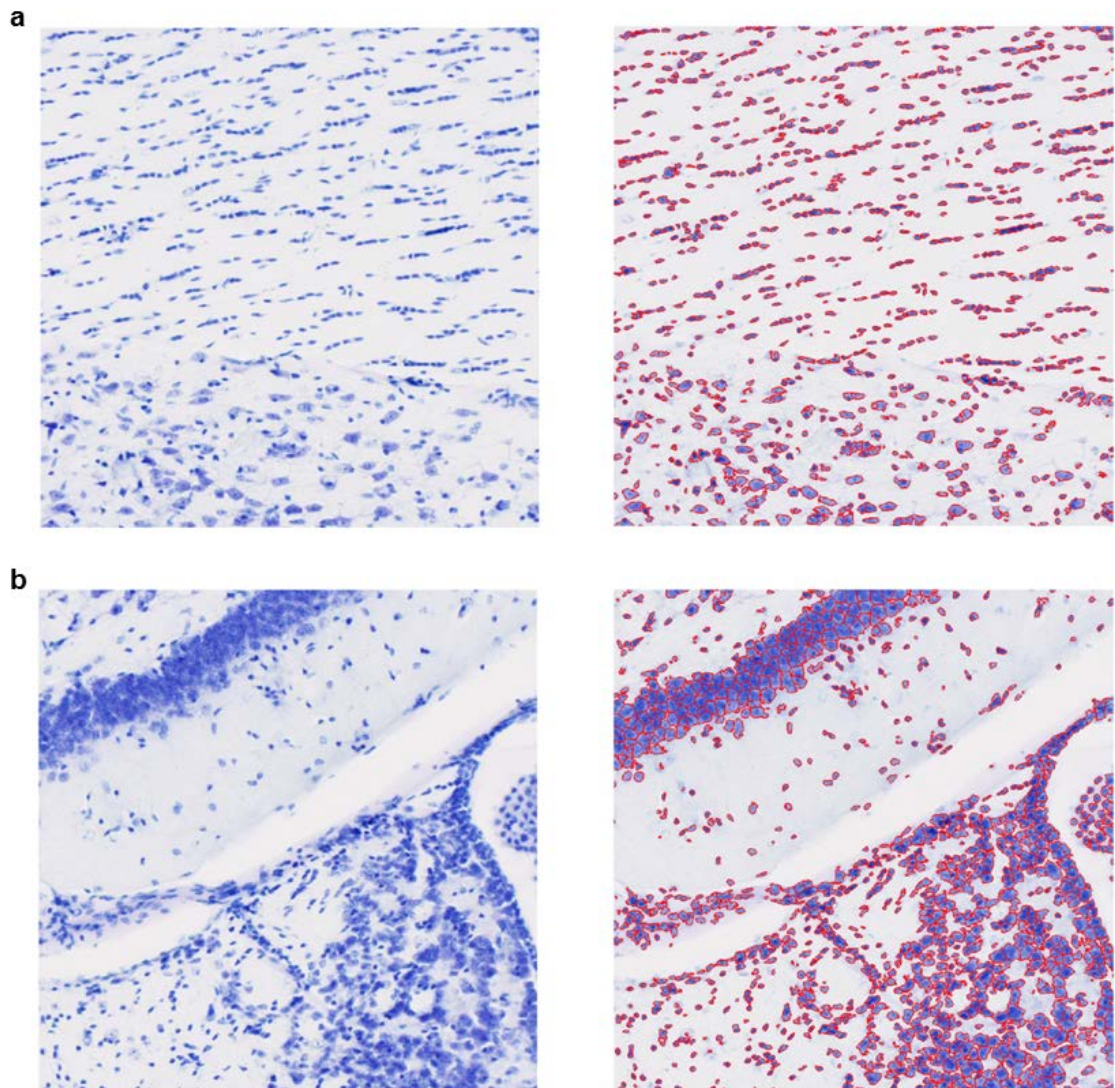


Figure 5.12: Cell segmentation in Nissl-stained images with a 3-levels hierarchical GMM (Gaussian smoothing with standard deviations of 4, 3 and 2 pixels), a minimum Hellinger distance of 0.7, a minimum cell size of 500 pixels and a maximum eigenvalues ratio of 10.

Discussion and conclusion

The methodological aspects of this work focused on 2 main objectives: **high-throughput production of 3D quantitative histopathology images** and **exploratory analysis of these images to generate new biological hypotheses**. **The proposed approach was then applied on a large-scale in preclinical studies with mouse models of A β plaque deposition**. Figure 5.13 summarizes the main steps involved in the production and analysis of 3D quantitative histopathology in mice as well as biology applications.

To process series of 2D section images into 3D quantitative histopathology images, a range of techniques was combined and integrated into a single image processing pipeline that will be made available to the neuroscience community through the BrainVISA website (www.brainvisa.info). The cornerstone of 3D histopathology reconstruction is the **block-face photography** volume. It constitutes a reference to generate spatially coherent histology volumes that respects the 3D geometry of the brain. The methodology relating to 3D histology image reconstruction have been largely covered in previous studies including several from our laboratory. **Previously, 3D tissue section reconstruction was applied in autoradiography studies focusing on brain glucose metabolism**. With autoradiography imaging, the parameter of interest is **continuous, quantitative and spatially smooth**. In this case, techniques developed in the context of clinical neuroimaging such as atlas-based analysis and voxel-based analysis can be directly carried-out to infer metabolic differences between groups of animals. With histological staining, a very wide range of markers can be studied. However, contrarily to autoradiography, **3D reconstructed histopathology volumes are color images which do not directly inform us on the amount of the marker being investigated**. Therefore a first contribution towards 3D brain-wide quantitative histopathology was to **extract quantitative information from high-resolution histology color images**.

Numerous techniques can be employed to segment histopathological markers with

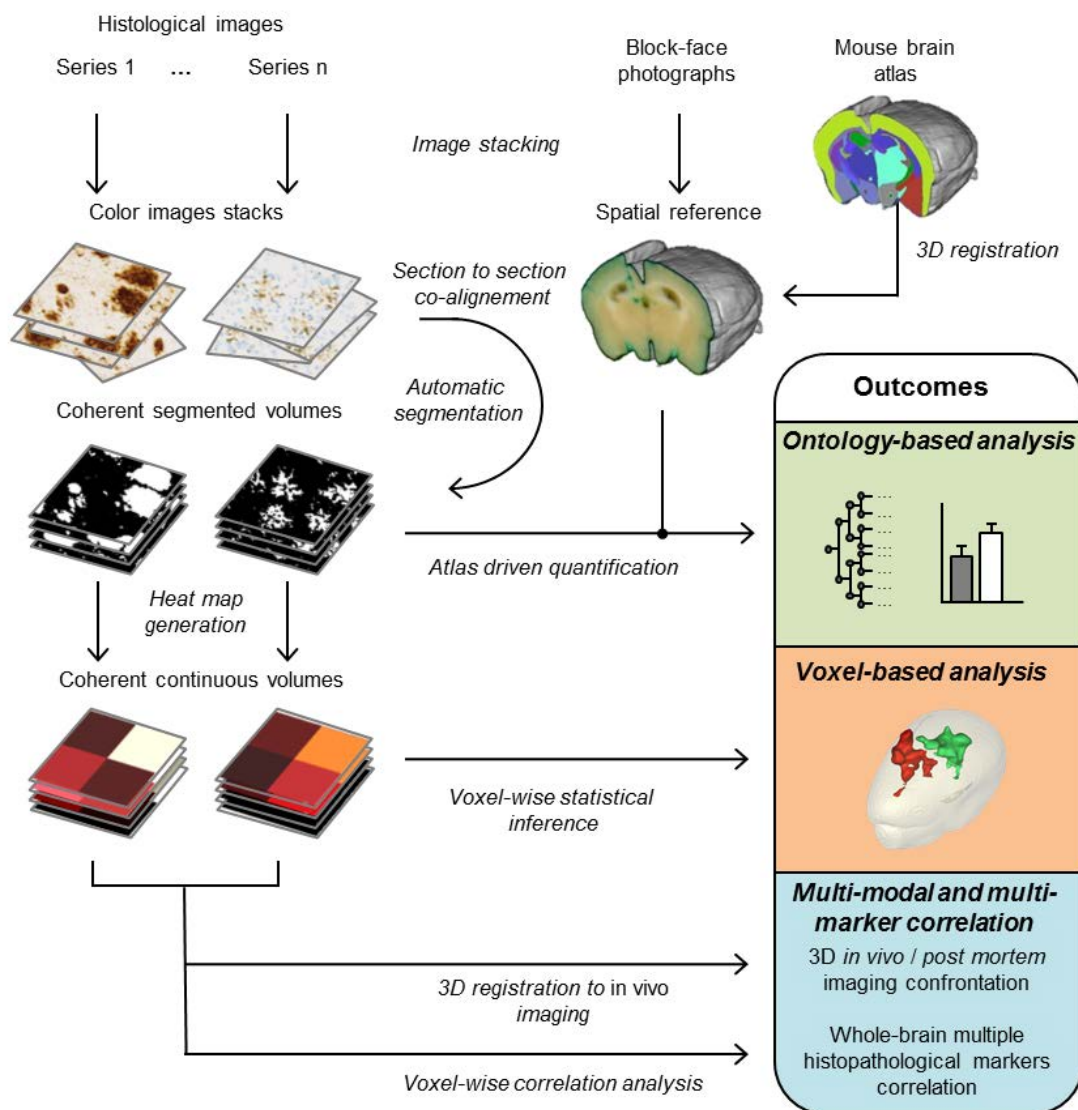


Figure 5.13: Summary of 3D quantitative histopathology methodology and applications.

various level of accuracy, computational cost and human involvement. The simpler methods rely on image intensity thresholding which is fast but suffers from imprecision. Here, we mostly focused on **supervised machine learning classification**. While being computationally more demanding, supervised machine learning greatly improves segmentation accuracy. Two supervised segmentation approaches were used throughout this work: **BioVision** and **WRF**. The first one provides good results in short times when the marker of interest has specific color properties. In more challenging cases such as in the presence of non-specific staining or artifacts, BioVision may fail due to the overlap between the staining color and noise. In such instances, a solution is to add richer, high-dimensional, features such as texture information. WRF was proposed as a fast and accurate way to classify images with high-dimensional color-texture features. As features get more complex, costs are increasing for features extraction computing time and memory usage. On the other hand, the increase in accuracy results in important gains in terms of human involvement for quality control and post-processing. Eventually, the choice between BioVision and WRF can be made on a case-by-case basis by considering the **trade-off between accuracy, computational cost and human involvement**.

Two very different and complementary approaches were described to analyze whole-brain histopathology images: the ontology-based analysis and the voxel-wise analysis. **Ontology-based analysis** is particularly useful to thoroughly phenotype animal models and to evaluate experimental perturbations that have global regional effects. This approach is related to the widely adopted region-based analysis for quantifying histopathological markers on 2D section images. In the case of 2D section images, ROI delineation has to be done manually by an operator which is both time-consuming and operator-dependent and could therefore lead to non-reproducible results. An important improvement brought by 3D reconstruction is that **brain atlases can be registered on 3D histopathology images to automatically define ROIs**. The atlas-based approach can be extended with a brain ontology which provides a standardized anatomical framework. Another advantage of 3D whole-brain quantification is that it enables to **decrease sampling errors** which can be particularly beneficial in regions where biomarkers are heterogeneously distributed. Recently, a meta-analysis has raised concerns about reproducibility in neuroscience which can be partly explained by low sample sizes [117]. On the other hand, ethical issues constrain the use of animal models. In this context, ontology-based analysis could participate in refining and standardizing the analysis of preclinical studies via: (1) **automated delineation of ROIs to limit**

inter- and intra-operator variability; (2) ontology-based analysis to adapt the ROIs to the scale of phenomena to be captured; (3) exhaustive 3D information to precisely estimate biomarker levels even if they present heterogeneous spatial distributions.

Voxel-wise analysis is a state-of-the art exploratory analysis approach for *in vivo* imaging modalities and *post mortem* 3D autoradiography. **This work is, to our knowledge, the first to propose voxel-wise analysis of 3D whole-brain histopathological data.** This has been permitted by the introduction of **brain-wide quantitative heat maps.** The principle of heat maps is to **transform the high-resolution binary image of the marker being investigated into a continuous-scale, spatially smooth, low-resolution image which represent the local amount of the marker.** Several methods for heat map generation were compared and validated with simulation experiments that modelled $A\beta$ plaque deposition. Voxel-wise analysis of 3D histopathology images opens new avenues for exploratory studies in preclinical neuroscience. It combines the advantages of histopathology to highlight a very wide range of markers with high specificity and spatial resolution and the advantages of voxel-wise analysis to detect clusters of significant changes between experimental groups. An advantage of this combination is **the ability to navigate back and forth between scales.** Indeed, while the proposed approach requires to reduce image resolution to perform voxel-wise analysis, once local differences are inferred at low-resolution, detected clusters can be matched back onto high-resolution images to better understand the microscopic driving forces that explain differences witnessed at low-resolution.

Along this work, 3D histopathology was applied in three collaborative preclinical studies. Several dozens of animals were included in these studies and overall, several tens of thousands of sections images were processed which shows that **3D histopathology is scalable to large-scale biology studies.** In a first study, the ontology-based analysis approach was useful to characterize $A\beta$ deposition in APP/PS1dE9 mice and highlighted brain regions that are significantly affected yet are rarely studied in Alzheimer’s disease. In a second study involving APP/PS1 mice, ontology-based analysis allowed to demonstrate a broad $A\beta$ lowering effect of 13C3a, an innovative immunotherapy currently in clinical trial for Alzheimer’s disease. Finally, 3D histopathology enabled to assess the effect of ADAM30, a gene that has been recently linked with Alzheimer’s disease, on the $A\beta$ load in APP_{Swe,Ind} mice. In this study, the voxel-wise approach was particularly helpful to detect small clusters of reduced $A\beta$ deposition. Because of the restricted spatial extension of the

clusters in the cerebral cortex and hippocampal region, these changes would have been hardly detectable with a region-based approach.

Compared to conventional protocols, however, **whole-brain quantification comes at a cost** in terms of IHC reagents consumption as well as in tissue processing and image acquisition times. Also, for a number of experiments, biologists have strong *a priori* on the localization of histopathological marker changes between groups. In these cases, a conventional region-based analysis on a few tissue sections can be sufficient to detect the presumed effect at a lower cost than with 3D histopathology. Therefore, **in essence, 3D histopathology is best adapted for exploratory studies**, when *a priori* knowledge about biomarker spatial distribution is low or when studying experimental perturbations with unknown localization. In those cases, 3D histopathology can detect local effects or subtle changes between groups that could have been missed by a conventional approach.

As discussed in the last chapter, a number of perspectives arise for 3D histopathology. New applications can be envisioned for the **validation of *in vivo* imaging modalities**. Provided that the *in vivo* imaging signal is quantitative, **3D histopathology could quantitatively assess how sensitive and how specific is the signal detected *in vivo***. Another perspective concerns the **analysis of cellular markers at the scale of the whole brain**. The major challenge will be to extract quantitative information from the tremendous amount of data that lies within high-resolution whole-slide images. Currently, individual cell segmentation is a bottleneck because whole-slide images of brain cells are highly crowded and individual cells are difficultly discernible. **In this work, a novel method for clustered brain cells segmentation was proposed** but major developments are still needed to benchmark existing methods and to scale the analysis to very large datasets. The potential applications of cellular markers analysis are huge. In this work, **a first application was shown to characterize the spatial relationships between several cellular and pathological markers in an APP/PS1 mouse**. However, this approach did not consider object-level features such as cell-size or shape. Computing cellular features at the level of the whole-brain will provide the opportunity to get deeper insight into neuroanatomy and to improve our knowledge of cellular mechanisms involved in disease states. For example, neuronal death is currently assessed indirectly by measuring brain tissue volume losses on anatomical MRI. In this context, 3D histopathology could help to understand how macroscopic changes observed *in vivo* on MRI relates to neuronal death at the microscopic scale. Besides neuronal death, a range of morphological changes affect brain cells during

Alzheimer's disease. For instance microglial cells undergo morphological changes that are not well understood at the system-level. An interesting perspective would be to understand relationships between the $A\beta$ plaques and neighboring microglial cells. These challenges are currently being investigated in the laboratory and several new collaborations have been initiated to apply 3D quantitative histopathology in preclinical studies focusing on cellular markers.

Appendix A

3D Histopathology Analysis Pipeline (3D-HAPi)

3D Histology Analysis Pipeline (3D-HAPi) is an image analysis pipeline dedicated to the brain-wide quantification of histopathological markers. It is part of BrainVISA which is a modular and customizable software platform built to host heterogeneous tools dedicated to neuroimaging research. BrainVISA is developed by french government founded research organizations (CEA, INSERM, INRIA, CNRS). It is a free and open-source software and can be downloaded from: <http://brainvisa.info>. BrainVISA pipelines are written in Python and consists of a succession of elementary image processing tools which are written in C++ and included in the *Aims* image processing library. A large panel of pipelines for clinical and preclinical imaging analysis are already available in BrainVISA. In 2008, our group has released BrainRAT which is a set of tools to reconstruct and analyze autoradiography images in 3D. A new release will be made soon with the latest tools for 3D reconstruction of histology section images, segmentation of histopathological markers and ontology-based analysis. These tools can be used separately or via 3D-HAPi which combines them together to provide a fully integrated tool for 3D whole-brain ontology-based analysis. This pipeline combines algorithms that have been developed by several members of the team along the last few years. 3D-HAPi will be released along with a detailed documentation and a test dataset. It consists of four modules (Figure A.1):

- **MODULE 1 - Photography: 3D reconstruction.** This module creates a spatial reference volume image using 2D block-face photographs of the brain tissue acquired during the cutting process with a dedicated photographic setup.

- **MODULE 2 - Histology: multiple 3D reconstruction.** This module stacks 2D tissue images digitized with bright-field imaging devices (flatbed high resolution scanner or virtual microscopy scanner, etc.); registers each section image with the spatial reference and segments histopathological markers using BioVision algorithm.
- **MODULE 3 - Digital atlas: 3D registration.** This module can be used to register a 3D digital atlas with the spatial reference to allow automated region of interest (ROI) analysis of histology volumes.
- **MODULE 4: Quantification: multiple 3D hierarchical analysis.** This last module outputs descriptive statistics for each region included in the brain ontology. The output file is a Comma Separated Value (CSV) text that is formatted so as to be easily handled in R.

Each of the module contains a number of steps which parameters can be easily modified by the user if the default parameters do not provide satisfactory results. At each step of the process, intermediate images can be opened in the Anatomist visualization software for quality control.

In the future, 3D-HAPi could be upgraded with new algorithms for image segmentation as well as with the recent developments for voxel-wise analysis of histopathological markers.

APPENDIX A: 3D HISTOPATHOLOGY ANALYSIS PIPELINE (3D-HAP_i)

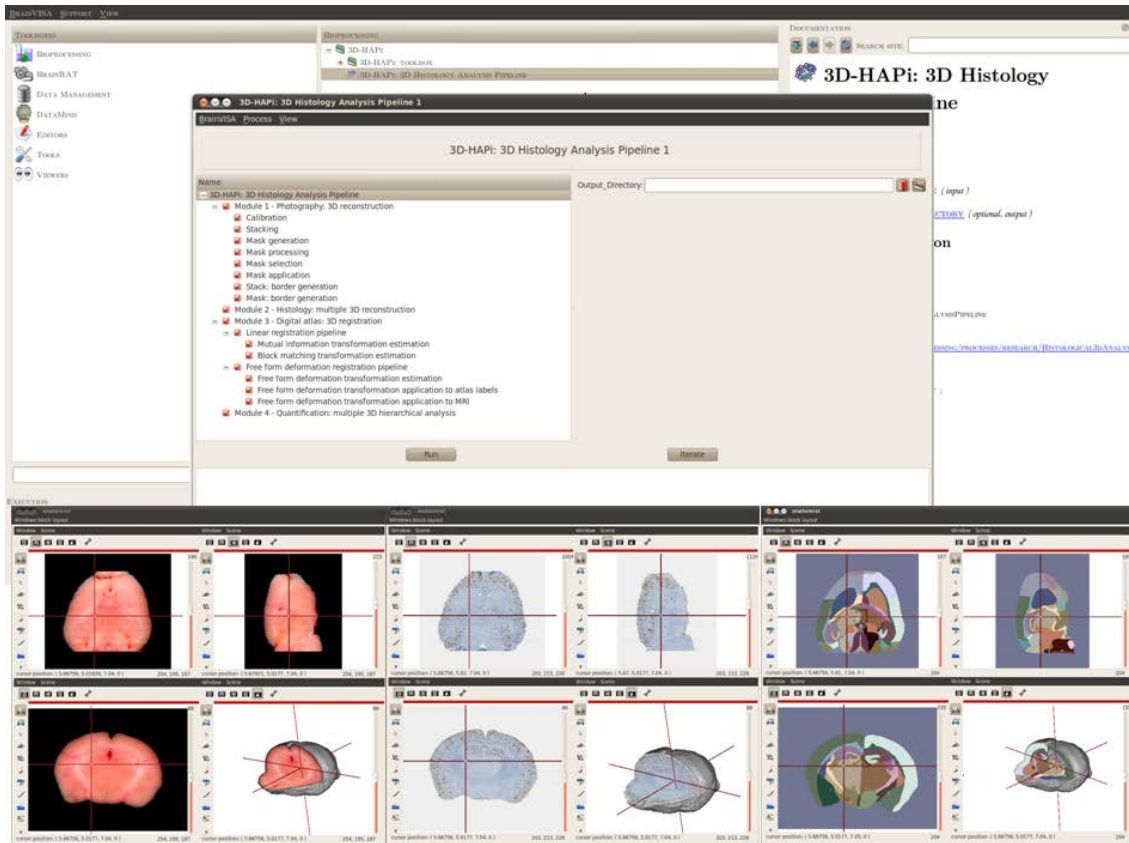


Figure A.1: Screen capture of BrainVISA with 3D-HAP_i and Anatomist. The four main modules of the pipeline are shown as well as the elementary processes that constitutes each module. Image visualization with Anatomist is shown on the bottom with, from left to right, a block-face photography volume, an A β plaque 3D immunohistochemistry volume and a registered MICE brain atlas. All these images were generated along the pipeline with the test dataset.

Appendix B

Experimental procedures summary

	Study 1	Study 2			Study 3	
Transgenic mouse strains	APP/PS1dE9	APP/PS1	PS1		APP ^{Swe,Ind⁻} ADAM30	APP ^{Swe,Ind⁻} Cre-ADAM30
Treatment	None	13C3a	DM4	None	None	
<i>In vivo</i> imaging	None	Gadolinium-staining MRI			None	
Age at euthanasia (monthes)	13.5	8			??	
Number of animals	7	8	3	4	5	10
Block-face photography volume resolution	$27 \times 27 \times 80 \mu\text{m}^3$	$33 \times 33 \times 125 \mu\text{m}^3$			8	
Histology series	4 series of 20- μm -thick sections: - Series 1: Nissl staining - Series 2: BAM10 IHC - Remaining series: kept for future analysis.	5 series of 25- μm -thick sections: - Series 1: Nissl staining - Series 2: 6E10 IHC - Series 3: anti-CD68 IHC - Series 4: anti-IgG IHC - Series 5: anti-Iba1 IHC			3 series of 30- μm -thick sections: - Series 1: Nissl staining - Series 2: 6E10 IHC - Series 3: kept for future analysis.	
Histology resolution	- Nissl series: 21 μm - BAM10 series: 5 μm	- Nissl series: 21 μm - 6E10 series: 5 μm - Nissl, 6E10, anti-CD68, anti-Iba1 series for one APP/PS1-DM4 mouse: 0.44 μm .			- Nissl series: 21 μm - 6E10 series: 5 μm	
Applications	Mouse model characterization	- Ontology-based immunotherapy evaluation - 2D versus 3D analysis comparison - Validation of amyloid plaque <i>in vivo</i> imaging - Cellular and pathological markers brainwide correlation			Voxel-based and ontology-based analysis of ADAM30 effect on A β load.	

APPENDIX B: EXPERIMENTAL PROCEDURES SUMMARY

Appendix C

Publications

Journal articles

M.E. Vanderberghe, *et al.* “Extending voxel-based statistical analysis approach to 3D *post mortem* high-resolution imaging,” in preparation.

M.D. Santin, **M.E. Vanderberghe**, A.S. Hérard, L. Pradier, C. Cohen, T. Debeir, T. Delzescaux, T. Rooney, M. Dhenain, “*In vivo* detection of amyloid plaques by gadolinium-stained MRI can be used to demonstrate the efficacy of an anti-A β antibody in transgenic mice.,” submitted.

F. Letronne, G. Laumet, A.M. Ayrat, J. Chapuis, F. Demiautte, M. Laga, **M.E. Vanderberghe**, N. Malmanche, F. Leroux, Y. Sottejeau, L. Chami, P. Dourlen, C. Bauer, L. Huot, M. Dhenain, E. Werkmeister, F. Hansmannel, J. Dumont, A. Bretteville, C. Delay, B. Dermaut, B. Deprez, A.S. Hérard, N. Souedet, F. Pasquier, C. Berr, J.J. Hauw, Y. Lemoine, L. Buée, D. Mann, R. Déprez, P. Amouyel, F. Checler, D. Hot, T. Delzescaux, K. Gevaert, J.C. Lambert, “Unrevealed APP metabolism: ADAM30 decreases amyloidogenic and non-amyloidogenic pathways through CTSD lysosomal activation.,” submitted.

M.E. Vandenberghe, A.S. Hérard, N. Souedet, E. Sadouni, M.D. Santin, D. Briet, D. Carré, J. Schulz, P. Hantraye, P.E. Chabrier, M. Auguet, T. Rooney, T. Debeir, V. Blanchard, L. Pradier, M. Dhenain, T. Delzescaux, “High-throughput 3D whole-brain quantitative histopathology in rodents.,” *Scientific Reports*, in revision.

International conferences

Y. Balbastre, **M.E. Vandenberghe**, J. Flament, A.S. Hérard, P. Gipchtein, S. Williams, N. Souedet, M. Guillermier, A. Bugi, A. Perrier, R. Aron-Badin, P. Hantraye, J.F. Mangin, T. Delzescaux, “An original approach for personalized parcellation of macaque MR brain images: application to caudate volume estimation in a model of Huntington’s disease.” In *Society for Neuroscience Annual Meeting (SFN)*, Chicago, 2015.

Y. Balbastre, **M.E. Vandenberghe**, A.S. Hérard, P. Gipchtein, C. Jan, A.L. Perrier, P. Hantraye, R. Aron-Badin, J.F. Mangin, T. Delzescaux, “A Quantitative Approach to Characterize MR Contrasts with Histology.” In *MICCAI Workshop on Brain Lesions (MICCAI Brainles)*, Munich, 2015.

M.E. Vandenberghe, Y. Balbastre, N. Souedet, A.S. Hérard, M. Dhenain, F. Frouin, T. Delzescaux, “Robust Supervised Segmentation of Neuropathology Whole-Slide Microscopy Images.” In *Engineering in Medicine and Biology Society (EMBC)*, Milano, 2015 (oral presentation).

M. Dhenain, S. Sawiak, **M.E. Vandenberghe**, A.S. Herard, T. Debeir, T. Rooney, M.D. Santin, T. Delzescaux, “Automatic segmentation of amyloid plaques on *in vivo* MRI after gadolinium-staining.” In *Alzheimer’s and Parkinson’s Diseases Congress (AD/PD)*, Nice, 2015.

J. Le Douce, E. Faivre, A.S. Hérard, M. Guérif, **M.E. Vandenberghe**, Y. Balbastre, T. Delzescaux, X. Toussay, B. Cauli, G. Bonvento, “Energy metabolism dysfunction in Alzheimer’s disease: role of astrocytes.” In *Gordon Research Conference (GRC)*, Ventura, 2015.

M.E. Vandenberghe, A.S. Hérard, Y. Balbastre, N. Souedet, F. Frouin, T. Delzescaux, “3D quantitative histopathology in the mouse brain: from mesoscopic to microscopic scale.” In *European Congress on Digital Pathology (EDCP)*, Paris, 2014 (oral and poster presentation).

Y. Balbastre, N. Souedet, D. Rivière, Y. Cointepas, **M.E. Vandenberghe**, A.S. Hérard, T. Delzescaux, “Parallel computing in image analysis using BrainVISA software: application to histopathological staining segmentation in whole slide images.”

APPENDIX C: PUBLICATIONS

In *European Congress on Digital Pathology (EDCP)*, Paris, 2014.

M.E. Vandenberghe, A.S. Hérard, N. Souedet, P. Hantraye, M. Dhenain, T. Delzescaux, “Automated quantification of amyloid load using an atlas-based analysis in a mouse model of Alzheimer’s disease,” *Alzheimer’s Association International Conference (AAIC)*, Boston, 2013 (poster presentation).

APPENDIX C: PUBLICATIONS

Bibliography

- [1] A. H. Coons, H. J. Creech, and R. N. Jones, “Immunological Properties of an Antibody Containing a Fluorescent Group.,” *Experimental Biology and Medicine*, vol. 47, pp. 200–202, June 1941.
- [2] A. R. Leitch, T. Schwarzacher, D. Jackson, and I. J. Leitch, “In situ hybridization: a practical guide.,” 1994.
- [3] C. J. F. Van Noorden and G. N. Jonges, “Analysis of enzyme reactions in situ,” *The Histochemical Journal*, vol. 27, pp. 101–118, Feb. 1995.
- [4] W. P. Faulk and G. M. Taylor, “An immunocolloid method for the electron microscope.,” *Immunochemistry*, vol. 8, pp. 1081–3, Nov. 1971.
- [5] EMA, “Guideline on Repeated Dose Toxicity,” 2007.
- [6] M. Angelo, S. C. Bendall, R. Finck, M. B. Hale, C. Hitzman, A. D. Borowsky, R. M. Levenson, J. B. Lowe, S. D. Liu, S. Zhao, Y. Natkunam, and G. P. Nolan, “Multiplexed ion beam imaging of human breast tumors,” *Nature Medicine*, vol. 20, pp. 436–442, Mar. 2014.
- [7] X. Michalet, F. F. Pinaud, L. A. Bentolila, J. M. Tsay, S. Doose, J. J. Li, G. Sundaresan, A. M. Wu, S. S. Gambhir, and S. Weiss, “Quantum dots for live cells, in vivo imaging, and diagnostics.,” *Science (New York, N.Y.)*, vol. 307, pp. 538–44, Jan. 2005.
- [8] C. Giesen, H. A. O. Wang, D. Schapiro, N. Zivanovic, A. Jacobs, B. Hattendorf, P. J. Schüffler, D. Grolimund, J. M. Buhmann, S. Brandt, Z. Varga, P. J. Wild, D. Günther, and B. Bodenmiller, “Highly multiplexed imaging of tumor tissues with subcellular resolution by mass cytometry.,” *Nature methods*, vol. 11, pp. 417–22, Apr. 2014.
- [9] H.-U. Dodt, U. Leischner, A. Schierloh, N. Jährling, C. P. Mauch, K. Deininger, J. M. Deussing, M. Eder, W. Zieglgänsberger, and K. Becker, “Ultramicroscopy: three-dimensional visualization of neuronal networks in the whole mouse brain.,” *Nature methods*, vol. 4, pp. 331–6, Apr. 2007.
- [10] K. Chung, J. Wallace, S.-Y. Kim, S. Kalyanasundaram, A. S. Andalman, T. J. Davidson, J. J. Mirzabekov, K. A. Zalocusky, J. Mattis, A. K. Denisin, S. Pak, H. Bernstein, C. Ramakrishnan, L. Grosenick, V. Gradinaru, and

BIBLIOGRAPHY

- K. Deisseroth, “Structural and molecular interrogation of intact biological systems.,” *Nature*, vol. 497, pp. 332–7, May 2013.
- [11] M.-T. Ke, S. Fujimoto, and T. Imai, “SeeDB: a simple and morphology-preserving optical clearing agent for neuronal circuit reconstruction.,” *Nature neuroscience*, vol. 16, no. 8, pp. 1154–61, 2013.
- [12] E. a. Susaki, K. Tainaka, D. Perrin, F. Kishino, T. Tawara, T. M. Watanabe, C. Yokoyama, H. Onoe, M. Eguchi, S. Yamaguchi, T. Abe, H. Kiyonari, Y. Shimizu, A. Miyawaki, H. Yokota, and H. R. Ueda, “Whole-brain imaging with single-cell resolution using chemical cocktails and computational analysis,” *Cell*, vol. 157, no. 3, pp. 726–739, 2014.
- [13] K. Ando, Q. Laborde, A. Lazar, D. Godefroy, I. Youssef, M. Amar, A. Pooler, M.-C. Potier, B. Delatour, and C. Duyckaerts, “Inside Alzheimer brain with CLARITY: senile plaques, neurofibrillary tangles and axons in 3-D.,” *Acta neuropathologica*, vol. 128, pp. 457–9, Sept. 2014.
- [14] B. G. Wilhelm, S. Mandad, S. Truckenbrodt, K. Kröhnert, C. Schäfer, B. Rammner, S. J. Koo, G. A. Claß en, M. Krauss, V. Haucke, H. Urlaub, and S. O. Rizzoli, “Composition of isolated synaptic boutons reveals the amounts of vesicle trafficking proteins.,” *Science (New York, N.Y.)*, vol. 344, pp. 1023–8, May 2014.
- [15] S. Mikula, J. Binding, and W. Denk, “Staining and embedding the whole mouse brain for electron microscopy.,” *Nature methods*, vol. 9, pp. 1198–201, Dec. 2012.
- [16] K. J. Hayworth, C. S. Xu, Z. Lu, G. W. Knott, R. D. Fetter, J. C. Tapia, J. W. Lichtman, and H. F. Hess, “Ultrastructurally smooth thick partitioning and volume stitching for large-scale connectomics.,” *Nature methods*, vol. 12, pp. 319–22, Feb. 2015.
- [17] W. Denk, J. H. Strickler, and W. W. Webb, “Two-photon laser scanning fluorescence microscopy.,” *Science (New York, N.Y.)*, vol. 248, pp. 73–6, Apr. 1990.
- [18] T. A. Klar and S. W. Hell, “Subdiffraction resolution in far-field fluorescence microscopy.,” *Optics letters*, vol. 24, pp. 954–6, July 1999.
- [19] M. J. Rust, M. Bates, and X. Zhuang, “Sub-diffraction-limit imaging by stochastic optical reconstruction microscopy (STORM).,” *Nature methods*, vol. 3, pp. 793–5, Oct. 2006.
- [20] R. A. A. Campbell, R. W. Eifert, and G. C. Turner, “OpenStage: a low-cost motorized microscope stage with sub-micron positioning accuracy.,” *PloS one*, vol. 9, p. e88977, Jan. 2014.

BIBLIOGRAPHY

- [21] H. Irshad, A. Veillard, L. Roux, and D. Racoceanu, “Methods for nuclei detection, segmentation, and classification in digital histopathology: a review-current status and future potential.,” *IEEE reviews in biomedical engineering*, vol. 7, pp. 97–114, Jan. 2014.
- [22] H. Braak and E. Braak, “Neuropathological stageing of Alzheimer-related changes.,” *Acta neuropathologica*, vol. 82, pp. 239–59, Jan. 1991.
- [23] M. J. West, L. Slomianka, and H. J. Gundersen, “Unbiased stereological estimation of the total number of neurons in the subdivisions of the rat hippocampus using the optical fractionator.,” *The Anatomical record*, vol. 231, pp. 482–97, Dec. 1991.
- [24] H. D. Samaroo, A. C. Opsahl, J. Schreiber, S. M. O’Neill, M. Marconi, J. Qian, S. Carvajal-Gonzalez, B. Tate, A. J. Milici, K. R. Bales, and D. T. Stephenson, “High throughput object-based image analysis of β -amyloid plaques in human and transgenic mouse brain,” *Journal of Neuroscience Methods*, vol. 204, pp. 179–188, Feb. 2012.
- [25] A. Feki, O. Teboul, A. Dubois, B. Bozon, A. Faure, P. Hantraye, M. Dhenain, B. Delatour, and T. Delzescaux, “Fully automated and adaptive detection of amyloid plaques in stained brain sections of Alzheimer transgenic mice.,” *Medical image computing and computer-assisted intervention : MICCAI ... International Conference on Medical Image Computing and Computer-Assisted Intervention*, 2007.
- [26] C. Chubb, Y. Inagaki, P. Sheu, B. Cummings, A. Wasserman, E. Head, and C. Cotman, “BioVision: an application for the automated image analysis of histological sections.,” *Neurobiology of aging*, vol. 27, pp. 1462–76, Oct. 2006.
- [27] S. Geman and D. Geman, “Stochastic Relaxation, Gibbs Distributions, and the Bayesian Restoration of Images,” *IEEE Transactions on Pattern Analysis and Machine Intelligence*, vol. PAMI-6, pp. 721–741, Nov. 1984.
- [28] C. P. Ferri, M. Prince, C. Brayne, H. Brodaty, L. Fratiglioni, M. Ganguli, K. Hall, K. Hasegawa, H. Hendrie, Y. Huang, A. Jorm, C. Mathers, P. R. Menezes, E. Rimmer, and M. Sczufca, “Global prevalence of dementia: a Delphi consensus study.,” *Lancet*, vol. 366, pp. 2112–7, Dec. 2005.
- [29] C. P. Ferri, R. Sousa, E. Albanese, W. S. Ribeiro, and M. Honyashiki, “World Alzheimer Report 2009 - Executive Summary. Edited by Prince M,” *Alzheimer’s Disease International*, pp. 1–22, 2009.
- [30] Y. Stern, “Cognitive reserve in ageing and Alzheimer’s disease.,” *The Lancet. Neurology*, vol. 11, pp. 1006–12, Nov. 2012.
- [31] N. D. Barnard, A. I. Bush, A. Ceccarelli, J. Cooper, C. A. de Jager, K. I. Erickson, G. Fraser, S. Kesler, S. M. Levin, B. Lucey, M. C. Morris, and

BIBLIOGRAPHY

- R. Squitti, "Dietary and lifestyle guidelines for the prevention of Alzheimer's disease.," *Neurobiology of aging*, vol. 35 Suppl 2, pp. S74–8, Sept. 2014.
- [32] T. J. van der Cammen, C. J. Verschoor, C. P. van Loon, F. van Harskamp, I. de Koning, W. J. Schudel, A. J. Slooter, C. Van Broeckhoven, and C. M. van Duijn, "Risk of left ventricular dysfunction in patients with probable Alzheimer's disease with APOE*4 allele.," *Journal of the American Geriatrics Society*, vol. 46, pp. 962–7, Aug. 1998.
- [33] P. M. Doraiswamy, J. Leon, J. L. Cummings, D. Marin, and P. J. Neumann, "Prevalence and Impact of Medical Comorbidity in Alzheimer's Disease," *The Journals of Gerontology Series A: Biological Sciences and Medical Sciences*, vol. 57, pp. M173–M177, Mar. 2002.
- [34] O. Zanetti, S. B. Solerte, and F. Cantoni, "Life expectancy in Alzheimer's disease (AD).," *Archives of gerontology and geriatrics*, vol. 49 Suppl 1, pp. 237–43, Jan. 2009.
- [35] Y. Zhao, T.-C. Kuo, S. Weir, M. S. Kramer, and A. S. Ash, "Healthcare costs and utilization for Medicare beneficiaries with Alzheimer's.," *BMC health services research*, vol. 8, p. 108, Jan. 2008.
- [36] C. R. Jack, D. S. Knopman, W. J. Jagust, R. C. Petersen, M. W. Weiner, P. S. Aisen, L. M. Shaw, P. Vemuri, H. J. Wiste, S. D. Weigand, T. G. Lesnick, V. S. Pankratz, M. C. Donohue, and J. Q. Trojanowski, "Tracking pathophysiological processes in Alzheimer's disease: An updated hypothetical model of dynamic biomarkers," *The Lancet Neurology*, vol. 12, no. 2, pp. 207–216, 2013.
- [37] B. P. Imbimbo, V. Solfrizzi, and F. Panza, "Are NSAIDs useful to treat Alzheimer's disease or mild cognitive impairment?," *Frontiers in aging neuroscience*, vol. 2, Jan. 2010.
- [38] J. Hardy, "Has the amyloid cascade hypothesis for Alzheimer's disease been proved?," *Current Alzheimer research*, vol. 3, pp. 71–3, Mar. 2006.
- [39] I. Benilova, E. Karran, and B. De Strooper, "The toxic A β oligomer and Alzheimer's disease: an emperor in need of clothes.," *Nature neuroscience*, vol. 15, pp. 349–57, Mar. 2012.
- [40] H. Dong, M. V. Martin, S. Chambers, and J. G. Csernansky, "Spatial relationship between synapse loss and beta-amyloid deposition in Tg2576 mice.," *The Journal of comparative neurology*, vol. 500, pp. 311–21, Jan. 2007.
- [41] D. Tampellini and G. K. Gouras, "Synapses, synaptic activity and intraneuronal abeta in Alzheimer's disease.," *Frontiers in aging neuroscience*, vol. 2, no. May, pp. 1–5, 2010.

BIBLIOGRAPHY

- [42] J. Murrell, M. Farlow, B. Ghetti, and M. D. Benson, "A mutation in the amyloid precursor protein associated with hereditary Alzheimer's disease.," *Science (New York, N.Y.)*, vol. 254, pp. 97–9, Oct. 1991.
- [43] E. Levy-Lahad, W. Wasco, P. Poorkaj, D. M. Romano, J. Oshima, W. H. Pettingell, C. E. Yu, P. D. Jondro, S. D. Schmidt, and K. Wang, "Candidate gene for the chromosome 1 familial Alzheimer's disease locus.," *Science (New York, N.Y.)*, vol. 269, pp. 973–7, Aug. 1995.
- [44] G. D. Schellenberg, T. D. Bird, E. M. Wijsman, H. T. Orr, L. Anderson, E. Nemens, J. A. White, L. Bonnycastle, J. L. Weber, and M. E. Alonso, "Genetic linkage evidence for a familial Alzheimer's disease locus on chromosome 14.," *Science (New York, N.Y.)*, vol. 258, pp. 668–71, Oct. 1992.
- [45] H. Hampel, "Amyloid- β and cognition in aging and Alzheimer's disease: molecular and neurophysiological mechanisms.," *Journal of Alzheimer's disease : JAD*, vol. 33 Suppl 1, pp. S79–86, Jan. 2013.
- [46] R. C. Petersen, P. Aisen, B. F. Boeve, Y. E. Geda, R. J. Ivnik, D. S. Knopman, M. Mielke, V. S. Pankratz, R. Roberts, W. A. Rocca, S. Weigand, M. Weiner, H. Wiste, and C. R. Jack, "Mild cognitive impairment due to Alzheimer disease in the community.," *Annals of neurology*, vol. 74, pp. 199–208, Aug. 2013.
- [47] R. S. Doody, R. G. Thomas, M. Farlow, T. Iwatsubo, B. Vellas, S. Joffe, K. Kieburtz, R. Raman, X. Sun, P. S. Aisen, E. Siemers, H. Liu-Seifert, and R. Mohs, "Phase 3 trials of solanezumab for mild-to-moderate Alzheimer's disease.," *The New England journal of medicine*, vol. 370, pp. 311–21, Jan. 2014.
- [48] R. J. Bateman, C. Xiong, T. L. S. Benzinger, A. M. Fagan, A. Goate, N. C. Fox, D. S. Marcus, N. J. Cairns, X. Xie, T. M. Blazey, D. M. Holtzman, A. Santacruz, V. Buckles, A. Oliver, K. Moulder, P. S. Aisen, B. Ghetti, W. E. Klunk, E. McDade, R. N. Martins, C. L. Masters, R. Mayeux, J. M. Ringman, M. N. Rossor, P. R. Schofield, R. A. Sperling, S. Salloway, and J. C. Morris, "Clinical and biomarker changes in dominantly inherited Alzheimer's disease.," *The New England journal of medicine*, vol. 367, pp. 795–804, Aug. 2012.
- [49] M. E. Murray, V. J. Lowe, N. R. Graff-Radford, A. M. Liesinger, A. Cannon, S. A. Przybelski, B. Rawal, J. E. Parisi, R. C. Petersen, K. Kantarci, O. A. Ross, R. Duara, D. S. Knopman, C. R. Jack, and D. W. Dickson, "Clinicopathologic and 11C-Pittsburgh compound B implications of Thal amyloid phase across the Alzheimer's disease spectrum.," *Brain : a journal of neurology*, vol. 138, pp. 1370–81, Mar. 2015.
- [50] A. de Calignon, M. Polydoro, M. Suarez-Calvet, C. William, D. H. Adamowicz, K. J. Kopeikina, R. Pitstick, N. Sahara, K. H. Ashe, G. A. Carlson, T. L.

BIBLIOGRAPHY

- Spires-Jones, and B. T. Hyman, "Propagation of Tau Pathology in a Model of Early Alzheimer's Disease," *Neuron*, vol. 73, pp. 685–697, Feb. 2012.
- [51] S. H. Choi, Y. H. Kim, M. Hebisch, C. Sliwinski, S. Lee, C. D'Avanzo, H. Chen, B. Hooli, C. Asselin, J. Muffat, J. B. Klee, C. Zhang, B. J. Wainger, M. Peitz, D. M. Kovacs, C. J. Woolf, S. L. Wagner, R. E. Tanzi, and D. Y. Kim, "A three-dimensional human neural cell culture model of Alzheimer's disease," *Nature*, vol. 515, pp. 274–8, Oct. 2014.
- [52] M. B. Graeber and W. J. Streit, "Microglia: biology and pathology.," *Acta neuropathologica*, vol. 119, pp. 89–105, Jan. 2010.
- [53] B. J. Cummings, T. Satou, E. Head, N. W. Milgram, G. M. Cole, M. J. Savage, M. B. Podlisny, D. J. Selkoe, R. Siman, B. D. Greenberg, and C. W. Cotman, "Diffuse plaques contain C-terminal A beta 42 and not A beta 40: evidence from cats and dogs.," *Neurobiology of aging*, vol. 17, pp. 653–9, Jan.
- [54] E. Heuer, R. F. Rosen, A. Cintron, and L. C. Walker, "Nonhuman primate models of Alzheimer-like cerebral proteopathy.," *Current pharmaceutical design*, vol. 18, pp. 1159–69, Jan. 2012.
- [55] A. Kraska, O. Dorieux, J.-L. Picq, F. Petit, E. Bourrin, E. Chenu, A. Volk, M. Perret, P. Hantraye, N. Mestre-Frances, F. Aujard, and M. Dhenain, "Age-associated cerebral atrophy in mouse lemur primates.," *Neurobiology of aging*, vol. 32, pp. 894–906, May 2011.
- [56] C. Duyckaerts, M.-C. Potier, and B. Delatour, *Alzheimer disease models and human neuropathology: similarities and differences.*, vol. 115. 2008.
- [57] A. Dubois, A.-S. Hérad, B. Delatour, P. Hantraye, G. Bonvento, M. Dhenain, and T. Delzescaux, "Detection by voxel-wise statistical analysis of significant changes in regional cerebral glucose uptake in an APP/PS1 transgenic mouse model of Alzheimer's disease.," *NeuroImage*, vol. 51, pp. 586–98, June 2010.
- [58] G. Poisnel, A.-S. Hérad, N. El Tannir El Tayara, E. Bourrin, A. Volk, F. Kober, B. Delatour, T. Delzescaux, T. Debeir, T. Rooney, J. Benavides, P. Hantraye, and M. Dhenain, "Increased regional cerebral glucose uptake in an APP/PS1 model of Alzheimer's disease.," *Neurobiology of aging*, vol. 33, pp. 1995–2005, Sept. 2012.
- [59] S. Oddo, A. Caccamo, J. D. Shepherd, M. P. Murphy, T. E. Golde, R. Kaye, R. Metherate, M. P. Mattson, Y. Akbari, and F. M. LaFerla, "Triple-transgenic model of Alzheimer's disease with plaques and tangles: intracellular Abeta and synaptic dysfunction.," *Neuron*, vol. 39, pp. 409–21, July 2003.
- [60] D. Games, D. Adams, R. Alessandrini, R. Barbour, P. Berthelette, C. Blackwell, T. Carr, J. Clemens, T. Donaldson, and F. Gillespie, "Alzheimer-type neuropathology in transgenic mice overexpressing V717F beta-amyloid precursor protein.," *Nature*, vol. 373, pp. 523–7, Feb. 1995.

BIBLIOGRAPHY

- [61] K. R. Zahs and K. H. Ashe, “‘Too much good news’ - are Alzheimer mouse models trying to tell us how to prevent, not cure, Alzheimer’s disease?,” *Trends in neurosciences*, vol. 33, pp. 381–9, Aug. 2010.
- [62] E. A. Susaki, K. Tainaka, D. Perrin, F. Kishino, T. Tawara, T. M. Watanabe, C. Yokoyama, H. Onoe, M. Eguchi, S. Yamaguchi, T. Abe, H. Kiyonari, Y. Shimizu, A. Miyawaki, H. Yokota, and H. R. Ueda, “Whole-brain imaging with single-cell resolution using chemical cocktails and computational analysis,” *Cell*, vol. 157, pp. 726–39, Apr. 2014.
- [63] R. Tomer, L. Ye, B. Hsueh, and K. Deisseroth, “Advanced CLARITY for rapid and high-resolution imaging of intact tissues.,” *Nature protocols*, vol. 9, pp. 1682–97, July 2014.
- [64] S. Ourselin, A. Roche, G. Subsol, X. Pennec, and N. Ayache, “Reconstructing a 3D structure from serial histological sections,” *Image and Vision Computing*, vol. 19, pp. 25–31, Jan. 2001.
- [65] J. Dauguet, T. Delzescaux, F. Condé, J.-F. Mangin, N. Ayache, P. Hantraye, and V. Frouin, “Three-dimensional reconstruction of stained histological slices and 3D non-linear registration with in-vivo MRI for whole baboon brain,” *Journal of Neuroscience Methods*, vol. 164, pp. 191–204, Aug. 2007.
- [66] K. Amunts, C. Lepage, L. Borgeat, H. Mohlberg, T. Dickscheid, M.-E. Rousseau, S. Bludau, P.-L. Bazin, L. B. Lewis, A.-M. Oros-Peusquens, N. J. Shah, T. Lippert, K. Zilles, and A. C. Evans, “BigBrain: an ultrahigh-resolution 3D human brain model.,” *Science (New York, N.Y.)*, vol. 340, no. 6139, pp. 1472–5, 2013.
- [67] J. Lebenberg, A.-S. Hérard, A. Dubois, J. Dauguet, V. Frouin, M. Dhenain, P. Hantraye, and T. Delzescaux, “Validation of MRI-based 3D digital atlas registration with histological and autoradiographic volumes: an anatomofunctional transgenic mouse brain imaging study.,” *NeuroImage*, vol. 51, pp. 1037–46, July 2010.
- [68] J. F. Smiley and C. Bleiwas, “Embedding matrix for simultaneous processing of multiple histological samples.,” *Journal of neuroscience methods*, vol. 209, pp. 195–8, July 2012.
- [69] A. Dubois, J. Dauguet, A.-S. Herard, L. Besret, E. Duchesnay, V. Frouin, P. Hantraye, G. Bonvento, and T. Delzescaux, “Automated three-dimensional analysis of histological and autoradiographic rat brain sections: application to an activation study.,” *Journal of cerebral blood flow and metabolism : official journal of the International Society of Cerebral Blood Flow and Metabolism*, vol. 27, pp. 1742–55, Oct. 2007.
- [70] J. G. Daugman, “Uncertainty relation for resolution in space, spatial frequency, and orientation optimized by two-dimensional visual cortical filters.,”

BIBLIOGRAPHY

- Journal of the Optical Society of America. A, Optics and image science*, vol. 2, pp. 1160–9, July 1985.
- [71] M. R. Turner, “Texture discrimination by Gabor functions,” *Biological Cybernetics*, vol. 55, no. 2-3, pp. 71–82.
- [72] L. Breiman, “Random Forests,” *Machine Learning*, vol. 45, no. 1, pp. 5–32, 2001.
- [73] F. Pedregosa, G. Varoquaux, A. Gramfort, V. Michel, B. Thirion, O. Grisel, M. Blondel, P. Prettenhofer, R. Weiss, V. Dubourg, J. Vanderplas, A. Passos, D. Cournapeau, M. Brucher, M. Perrot, and E. Duchesnay, “Scikit-learn: Machine Learning in Python,” *JOURNAL OF MACHINE LEARNING RESEARCH*, vol. 12, pp. 2825–2830, Oct. 2011.
- [74] C. Chen, A. Liaw, A. L. Com, and L. Breiman, “Using Random Forest to Learn Imbalanced Data,” tech. rep., 2004.
- [75] Y. Balbastre, N. Souedet, D. Rivière, Y. Cointepas, M. Vandenberghe, A.-S. Hérard, and T. Delzescaux, “Parallel computing in image analysis using BrainVISA software: Application to histopathological staining segmentation in whole slide images,” in *European Congress on Digital Pathology*, 2014.
- [76] F. Bianconi and A. Fernández, “Evaluation of the effects of Gabor filter parameters on texture classification,” *Pattern Recognition*, vol. 40, pp. 3325–3335, Dec. 2007.
- [77] S. E. Grigorescu, N. Petkov, and P. Kruizinga, “Comparison of texture features based on Gabor filters.,” *IEEE transactions on image processing : a publication of the IEEE Signal Processing Society*, vol. 11, pp. 1160–7, Jan. 2002.
- [78] C. Palm, “Color texture classification by integrative Co-occurrence matrices,” *Pattern Recognition*, vol. 37, pp. 965–976, May 2004.
- [79] a. E. Dorr, J. P. Lerch, S. Spring, N. Kabani, and R. M. Henkelman, “High resolution three-dimensional brain atlas using an average magnetic resonance image of 40 adult C57Bl/6J mice,” *NeuroImage*, vol. 42, no. 1, pp. 60–69, 2008.
- [80] P. Viola and W. Wells, “Alignment by maximization of mutual information,” in *Proceedings of IEEE International Conference on Computer Vision*, pp. 16–23, IEEE Comput. Soc. Press, 1995.
- [81] D. Rueckert, L. I. Sonoda, C. Hayes, D. L. Hill, M. O. Leach, and D. J. Hawkes, “Nonrigid registration using free-form deformations: application to breast MR images.,” *IEEE transactions on medical imaging*, vol. 18, pp. 712–21, Aug. 1999.

BIBLIOGRAPHY

- [82] D. Mattes, D. R. Haynor, H. Vesselle, T. K. Lewellen, and W. Eubank, "PET-CT image registration in the chest using free-form deformations.," *IEEE transactions on medical imaging*, vol. 22, pp. 120–8, Jan. 2003.
- [83] D. M. Bowden, E. Song, J. Kosheleva, and M. F. Dubach, "NeuroNames: an ontology for the BrainInfo portal to neuroscience on the web.," *Neuroinformatics*, vol. 10, pp. 97–114, Jan. 2012.
- [84] A. Dubois, A.-S. Hérard, B. Delatour, P. Hantraye, G. Bonvento, M. Dhenain, and T. Delzescaux, "Detection by voxel-wise statistical analysis of significant changes in regional cerebral glucose uptake in an APP/PS1 transgenic mouse model of Alzheimer's disease.," *NeuroImage*, vol. 51, no. 2, pp. 586–598, 2010.
- [85] L. Boussicault, A.-S. Hérard, N. Calingasan, F. Petit, C. Malgorn, N. Merienne, C. Jan, M.-C. Gaillard, R. Lerchundi, L. F. Barros, C. Escartin, T. Delzescaux, J. Mariani, P. Hantraye, M. F. Beal, E. Brouillet, C. Véga, and G. Bonvento, "Impaired brain energy metabolism in the BACHD mouse model of Huntington's disease: critical role of astrocyte-neuron interactions.," *Journal of cerebral blood flow and metabolism : official journal of the International Society of Cerebral Blood Flow and Metabolism*, vol. 34, pp. 1500–10, Sept. 2014.
- [86] K. J. Friston, C. D. Frith, P. F. Liddle, R. J. Dolan, A. A. Lammertsma, and R. S. Frackowiak, "The relationship between global and local changes in PET scans.," *Journal of cerebral blood flow and metabolism : official journal of the International Society of Cerebral Blood Flow and Metabolism*, vol. 10, pp. 458–66, July 1990.
- [87] S. Sawiak, N. Wood, G. Williams, a. Morton, and T. Carpenter, "SPM Mouse: A new toolbox for SPM in the animal brain," *Proceedings 17th Scientific Meeting, International Society for Magnetic Resonance in Medicine*, vol. 17, p. 1086, 2009.
- [88] K. J. Friston, A. P. Holmes, K. J. Worsley, J.-P. Poline, C. D. Frith, and R. S. J. Frackowiak, "Statistical parametric maps in functional imaging: A general linear approach," *Human Brain Mapping*, vol. 2, pp. 189–210, Oct. 1994.
- [89] C. R. Genovese, N. A. Lazar, and T. Nichols, "Thresholding of statistical maps in functional neuroimaging using the false discovery rate.," *NeuroImage*, vol. 15, pp. 870–8, Apr. 2002.
- [90] E. T. Bullmore, J. Suckling, S. Overmeyer, S. Rabe-Hesketh, E. Taylor, and M. J. Brammer, "Global, voxel, and cluster tests, by theory and permutation, for a difference between two groups of structural MR images of the brain.," *IEEE transactions on medical imaging*, vol. 18, pp. 32–42, Jan. 1999.

BIBLIOGRAPHY

- [91] T. E. Nichols, “Multiple testing corrections, nonparametric methods, and random field theory,” *NeuroImage*, vol. 62, no. 2, pp. 811–815, 2012.
- [92] C. D. Barr and F. P. Schoenberg, “On the Voronoi estimator for the intensity of an inhomogeneous planar Poisson process,” *Biometrika*, vol. 97, pp. 977–984, Sept. 2010.
- [93] T. Hastie, R. Tibshirani, and J. Friedman, *The Elements of Statistical Learning*. Springer Series in Statistics, 2009.
- [94] I. S. Abramson, “On Bandwidth Variation in Kernel Estimates-A Square Root Law,” *The Annals of Statistics*, vol. 10, pp. 1217–1223, Dec. 1982.
- [95] D. Schenk, R. Barbour, W. Dunn, G. Gordon, H. Grajeda, T. Guido, K. Hu, J. Huang, K. Johnson-Wood, K. Khan, D. Kholodenko, M. Lee, Z. Liao, I. Lieberburg, R. Motter, L. Mutter, F. Soriano, G. Shopp, N. Vasquez, C. Vandeventer, S. Walker, M. Wogulis, T. Yednock, D. Games, and P. Seubert, “Immunization with amyloid-beta attenuates Alzheimer-disease-like pathology in the PDAPP mouse.,” *Nature*, vol. 400, pp. 173–7, July 1999.
- [96] L. Pradier, C. Cohen, V. Blanchard, T. Debeir, P. Barneoud, T. Canton, J. Menager, A. Bohme, T. Rooney, M.-C. Guillet, B. Cameron, Y. Shi, S. Naimi, J. Ravetch, S. Claudel, and J. Alam, “SAR228810: an anti-protofibrillar A β antibody designed to reduce risk of amyloid-related imaging abnormalities (ARIA),” in *Alzheimer’s Association International Conference*, 2013.
- [97] M. Garcia-Alloza, E. M. Robbins, S. X. Zhang-Nunes, S. M. Purcell, R. A. Betensky, S. Raju, C. Prada, S. M. Greenberg, B. J. Bacskai, and M. P. Frosch, “Characterization of amyloid deposition in the APP^{swe}/PS1^{dE9} mouse model of Alzheimer disease.,” *Neurobiology of disease*, vol. 24, pp. 516–24, Dec. 2006.
- [98] L. Mucke, E. Masliah, G. Q. Yu, M. Mallory, E. M. Rockenstein, G. Tatsuno, K. Hu, D. Kholodenko, K. Johnson-Wood, and L. McConlogue, “High-level neuronal expression of abeta 1-42 in wild-type human amyloid protein precursor transgenic mice: synaptotoxicity without plaque formation.,” *The Journal of neuroscience : the official journal of the Society for Neuroscience*, vol. 20, pp. 4050–8, June 2000.
- [99] G. Paxinos and K. Franklin, *The Mouse Brain in Stereotaxic Coordinates*. 2001.
- [100] R. N. Spreng, R. A. Mar, and A. S. N. Kim, “The common neural basis of autobiographical memory, prospection, navigation, theory of mind, and the default mode: a quantitative meta-analysis.,” *Journal of cognitive neuroscience*, vol. 21, pp. 489–510, Mar. 2009.
- [101] S. D. Vann, J. P. Aggleton, and E. A. Maguire, “What does the retrosplenial cortex do?,” *Nature reviews. Neuroscience*, vol. 10, pp. 792–802, Nov. 2009.

BIBLIOGRAPHY

- [102] A. Lenartowicz and A. R. McIntosh, “The role of anterior cingulate cortex in working memory is shaped by functional connectivity.,” *Journal of cognitive neuroscience*, vol. 17, pp. 1026–42, July 2005.
- [103] G. Pengas, J. R. Hodges, P. Watson, and P. J. Nestor, “Focal posterior cingulate atrophy in incipient Alzheimer’s disease.,” *Neurobiology of aging*, vol. 31, pp. 25–33, Jan. 2010.
- [104] B. A. Vogt and M. W. Miller, “Cortical connections between rat cingulate cortex and visual, motor, and postsubicular cortices.,” *The Journal of comparative neurology*, vol. 216, pp. 192–210, May 1983.
- [105] H. Oh, C. Habeck, C. Madison, and W. Jagust, “Covarying alterations in $A\beta$ deposition, glucose metabolism, and gray matter volume in cognitively normal elderly,” *Human Brain Mapping*, vol. 35, no. 1, pp. 297–308, 2014.
- [106] M. Jucker and L. C. Walker, “Pathogenic protein seeding in Alzheimer disease and other neurodegenerative disorders,” *Annals of Neurology*, vol. 70, no. 4, pp. 532–540, 2011.
- [107] A. Petiet, M. Santin, A. Bertrand, C. J. Wiggins, F. Petit, D. Houitte, P. Hantraye, J. Benavides, T. Debeir, T. Rooney, and M. Dhenain, “Gadolinium-staining reveals amyloid plaques in the brain of Alzheimer’s transgenic mice,” *Neurobiology of Aging*, vol. 33, no. 8, pp. 1533–1544, 2012.
- [108] J. L. De Reuck, V. Deramecourt, F. Auger, N. Durieux, C. Cordonnier, D. Devos, L. Defebvre, C. Moreau, D. Caparros-Lefebvre, D. Leys, C. A. Maurage, F. Pasquier, and R. Bordet, “Iron deposits in post-mortem brains of patients with neurodegenerative and cerebrovascular diseases: a semi-quantitative 7.0 T magnetic resonance imaging study.,” *European journal of neurology : the official journal of the European Federation of Neurological Societies*, vol. 21, pp. 1026–31, July 2014.
- [109] J. Serra, *Image Analysis and Mathematical Morphology*. Orlando, FL, USA: Academic Press, Inc., 1983.
- [110] L. Vincent and P. Soille, “Watersheds in digital spaces: an efficient algorithm based on immersion simulations,” *IEEE Transactions on Pattern Analysis and Machine Intelligence*, vol. 13, pp. 583–598, June 1991.
- [111] Y. He, H. Gong, B. Xiong, X. Xu, A. Li, T. Jiang, Q. Sun, S. Wang, Q. Luo, and S. Chen, “iCut: an Integrative Cut Algorithm Enables Accurate Segmentation of Touching Cells.,” *Scientific reports*, vol. 5, p. 12089, Jan. 2015.
- [112] D. Greig, B. Porteous, and A. Seheult, “Exact maximum a posteriori estimation for binary images,” *Journal of the Royal Statistical Society, Series B*, vol. 51, pp. 271–279, Jan. 1989.

BIBLIOGRAPHY

- [113] C. Schmitz, B. S. Eastwood, S. J. Tappan, J. R. Glaser, D. a. Peterson, and P. R. Hof, “Current automated 3D cell detection methods are not a suitable replacement for manual stereologic cell counting.,” *Frontiers in neuroanatomy*, vol. 8, no. May, p. 27, 2014.
- [114] A. Lehmussola, P. Ruusuvuori, J. Selinummi, H. Huttunen, and O. Yli-Harja, “Computational framework for simulating fluorescence microscope images with cell populations.,” *IEEE transactions on medical imaging*, vol. 26, pp. 1010–6, July 2007.
- [115] C. F. J. Wu, “On the Convergence Properties of the EM Algorithm,” *The Annals of Statistics*, vol. 11, no. 1, pp. pp. 95–103, 1983.
- [116] M. Tsukahara, S. Mitrovic, V. Gajdosik, G. Margaritondo, L. Pournin, M. Ramaioli, D. Sage, Y. Hwu, M. Unser, and T. M. Lieblich, “Coupled tomography and distinct-element-method approach to exploring the granular media microstructure in a jamming hourglass,” *Phys. Rev. E*, vol. 77, no. 6, p. 61306, 2008.
- [117] K. S. Button, J. P. A. Ioannidis, C. Mokrysz, B. A. Nosek, J. Flint, E. S. J. Robinson, and M. R. Munafò, “Power failure: why small sample size undermines the reliability of neuroscience.,” *Nature reviews. Neuroscience*, vol. 14, pp. 365–76, May 2013.